



HAL
open science

Contribution to the study of heat relaxation in nanostructures of biological interest

Jordane Soussi

► **To cite this version:**

Jordane Soussi. Contribution to the study of heat relaxation in nanostructures of biological interest. Other. Université Paris Saclay (COMUE), 2015. English. NNT : 2015SACLCO13 . tel-01266055

HAL Id: tel-01266055

<https://theses.hal.science/tel-01266055>

Submitted on 2 Feb 2016

HAL is a multi-disciplinary open access archive for the deposit and dissemination of scientific research documents, whether they are published or not. The documents may come from teaching and research institutions in France or abroad, or from public or private research centers.

L'archive ouverte pluridisciplinaire **HAL**, est destinée au dépôt et à la diffusion de documents scientifiques de niveau recherche, publiés ou non, émanant des établissements d'enseignement et de recherche français ou étrangers, des laboratoires publics ou privés.

NNT : 2015SACL013

THESE DE DOCTORAT
DE
L'UNIVERSITE PARIS-SACLAY
PREPAREE A
CENTRALESUPELEC

ECOLE DOCTORALE N° 579
Sciences Mécaniques et Énergétiques, Matériaux et Géosciences

Spécialité Énergétique

Par

M. Jordane Soussi

Contribution to the study of heat relaxation in nanostructures of biological interest

Thèse présentée et soutenue à Châtenay-Malabry, le 10 décembre 2015 :

Composition du Jury :

Dr Le Pioufle Bruno	Professeur à l'ENS Cachan	Président
Dr Donadio Davide	Assistant Professor à UC Davis	Rapporteur
Dr Gazeau Florence	Directeur de recherche au CNRS	Rapporteur
Dr Pansu Robert	Directeur de recherche au CNRS	Examineur
Dr Volz Sebastian	Directeur de recherche au CNRS	Directeur de thèse
Dr Chalopin Yann	Chargé de recherche au CNRS	Co-directeur de thèse
M. Audibert Jean-Frédéric	Assistant ingénieur à l'ENS Cachan	Invité

Remerciements

Le doctorat est une expérience très enrichissante mais c'est aussi une étape difficile. En ce qui me concerne, ce fût ma première expérience professionnelle et ma première recherche scientifique mais avant tout ce fût une aventure humaine. Ainsi les travaux condensés dans ce manuscrit de thèse sont le résultat d'un travail d'équipe et des multiples interactions que j'ai pu avoir avec des gens qui n'ont parfois rien à voir avec mon sujet de thèse mais qui ont tout de même contribué à cette dernière. Ces remerciements sont écrits pour toutes ces personnes qui méritent d'être citées mais aussi pour les futurs doctorants qui liront ce manuscrit à qui j'adresse mon plus sincère message de soutien.

La première personne que je me dois de remercier est bien sûr mon encadrant Yann Chalopin dont le foisonnement d'idées est à l'origine de l'originalité des problématiques abordées dans ma thèse. Il m'a toujours poussé à aller plus loin dans la résolution des problématiques que nous avons abordées.

En second lieu, Sebastian Volz, mon directeur de thèse, qui a encadré mon travail et a favorisé mon ouverture en m'encourageant à participer à de nombreuses conférences et workshops ce qui m'a permis de m'ouvrir et comprendre le monde de la recherche.

Je tiens également à remercier Bruno Le Pioufle, Olivier Français et Robert Pansu qui ont encadré la partie expérimentale des travaux présentés et dont les conseils et expertises scientifiques ont été fort utiles. Merci aussi à Bruno et Robert d'avoir accepté de faire partie de mon jury de thèse.

De plus je remercie chaudement Jean-Frédéric Audiber sans qui je n'aurais pas pu réaliser les expériences dont les résultats sont présentés dans ce manuscrit.

Je remercie le travail fourni par mes rapporteurs Florence Gazeau et Davide Donadio, qui ont revu ma thèse dans les temps malgré les délais très courts.

Mon travail a nécessité des ressources de calculs importantes qui ont été fournies par le mésocentre du campus de Châtenay-Malabry de CentraleSupélec. Je remercie donc l'équipe du mésocentre Igloo ainsi que Matthieu Boileau qui s'est occupé de Madness et de Genesis que j'ai aussi largement utilisé. J'exprime aussi ma gratitude à Sebastien Turgis pour sa gentillesse et sa promptitude à m'aider.

Je suis très reconnaissant envers Gloria Foulet, Pierre-Eymeric Janolin et Hichem Dammak pour m'avoir permis d'enseigner dans leurs cours respectifs. Cette expérience a été extrêmement enrichissante pour moi.

Je remercie également le personnel administratif du laboratoire EM2C, Nathalie Rodrigues, Noï Lavaud, Brigitte Llobel et Anne-Cécile Aïach et de l'Ecole doctorale, Catherine Lhopital et Emmanuelle Coplo.

Le doctorat ne se résume pas aux calculs, expériences et enseignements et je ne l'aurais pas vécu de la même manière sans les moments passés avec mes collègues de laboratoires. Ainsi je tiens à remercier tout particulièrement mes co-bureaux Benoit Latour, Chaï Koren et Wafa Bendahoui pour leur soutien moral mais aussi scientifique mais surtout pour tous les bons moments passés ensembles. J'espère que je revivrai pareils moments que ceux que nous avons passé ensembles !

Merci aussi à tous les membres de la nano-team, les conférences, les group meetings et les échanges que nous avons eu ont été d'excellents moments. Ainsi je remercie Thomas Antoni, Jérôme Saint-Martin, Yuriy Kosevich, Kostas Termentzidis, José Ordonez, Shenghong Ju, Yuxiang Ni, Shiyun Xiong, Aymeric Ramière, Laurent Tranchant, Kimmo Säskilathi, Kyle Horne, Juliana Jaramillo, Wassim Kassem, Haoxue Han, Sergei Gluchko, Lantao Yu , Yunhui Wu, Brice Davier, Romain Bude et Mikyung Lim.

Il me reste à remercier tous les membres du laboratoire EM2C, vous êtes trop nombreux pour être tous cités mais je vous remercie pour les moments partagés à la cafétéria, au RU et ailleurs qui font les petits plaisirs de tout les jours.

Merci aussi aux membres de Institut d'Alembert à L'ENS Cachan avec qui j'ai échangé et partagé lors de mes visites répétées.

Pour finir, il me tient à cœur de remercier ma fiancée Amélie Tuton qui m'a soutenu dans tous les moments difficiles au point de venir passer ses weekends au laboratoire avec moi quand je devais travailler. Tu m'as soutenu sans faillir dans les pires moments de doutes et je t'en remercie.

Abstract

In medicine, nanotechnologies give the opportunity to create new care practices such as local hyperthermia and targeted drug delivery. These applications imply new scientific challenges concerning the design of nanodevices and the properties of their biological environment. In this thesis, we have analysed several aspects of heat relaxation of such systems. We have used both Molecular Dynamics numerical simulations and Fluorescence-lifetime imaging microscopy experiments. We present a study of heat transfer from a solvated nanoparticle and show that attaching a polymer on its surface reduces the thermal resistance between the particle and its aqueous environment. We have modelled lipid bilayers to compute their dielectric properties and their viscosity have been investigated by fluorescence imaging. The experiments conducted on both suspended lipid membrane and giant unilamellar vesicles show that the viscosity decreases when the temperature increases and when a transmembrane voltage is applied to inducing a structural change.

Résumé

En médecine, les nanotechnologies permettent le développement de nouvelles techniques de soin comme l'hyperthermie local ou la délivrance ciblée de médicaments. Ces applications impliquent de nouveaux défis scientifiques concernant la conception de nanosystems et les propriétés de leur environnement biologique. Dans cette thèse, nous avons analysé plusieurs aspects de la relaxation thermique de tels systèmes. Nous avons mise en œuvre la fois des simulations de Dynamique Moléculaire et des mesures expérimentales de microscopie d'imagerie en temps de vie de fluorescence. Nous présentons une étude numérique du transfert thermique depuis une nanoparticule en solution aqueuse et montrons qu'attacher un polymère à sa surface permet de réduire la résistance thermique entre la particule et son environnement. Nous avons modélisé des bicouches lipidiques pour calculer leurs propriétés diélectriques et leur viscosité a été étudiée par microscopie de fluorescence. Ces expériences sont réalisées sur des membranes suspendues et des vésicules unilamellaires géantes et démontrent que la viscosité des bicouches lipidiques diminue avec la température et l'application d'une tension transmembranaire induisant un changement de structure.

Contents

Abstract	v
Résumé	vii
Introduction	1
I Theory and methods	5
1 Theoretical framework and Molecular Dynamics simulation methods	7
1.1 Introduction	8
1.2 Statistical ensembles and probability density	8
1.3 Molecular Dynamics simulation	13
1.4 Computing physical properties using Molecular Dynamics simulations	27
1.5 Conclusion	45
II Solid/liquid interface	47
2 Heat transfer at a solid/liquid interface	49
2.1 Introduction	50
2.2 Modelling	51
2.3 Effect of the curvature on the gold/water interface	54
2.4 Interface Resistance calculation	55
2.5 Physical analysis of the interfaces	58
2.6 Qualitative analysis by a transient non-equilibrium method	61
2.7 Generalization of the results	62
2.8 Conclusion	65
III Lipid bilayers	67
3 Lipid bilayer systems	69

3.1	Introduction	70
3.2	Self-organisation of lipids in water: bilayers, micelles and vesicles	70
3.3	Thermal properties of lipid bilayers	72
3.4	Response to electric field	75
3.5	Conclusion	79
4	Dielectric properties of lipid bilayers	81
4.1	Introduction	82
4.2	Model description and calculation method	82
4.3	Results	84
4.4	The bilayer morphology and its effect on the dielectric properties	90
4.5	Conclusion	95
5	Viscosity of a suspended DPPC lipid bilayer: effect of the solvent	97
5.1	Introduction	98
5.2	Experimental investigations	98
5.3	Variation of the decane concentration in the bilayer from Molecular Dynamics simulations	109
5.4	Prediction of the fluorescence lifetime variation	116
5.5	Conclusion	117
6	Voltage and temperature induced phase change in Giant Unilamellar Vesicles	119
6.1	Introduction	120
6.2	Fabrication of the Giant Unilamellar Vesicles: the electroformation	120
6.3	Imaging method	122
6.4	Mapping the orientation of the BODIPY in the bilayer: an experimental approach	122
6.5	Temperature and voltage dependent viscosity of the bilayer from FLIM experiments on GUV	124
6.6	Conclusion	135
	Conclusion	137
A	An example of non-ergodic system: the 1D harmonic chain	139
B	Classical approximation and equipartition theorem	141
C	Radial distribution function in diffraction experiments	143
D	Link between susceptibility and fluctuations	145
E	Thermal conductivity	147
E.1	The Green-Kubo relations	147

CONTENTS	xi
E.2 Applying the Green-Kubo formula in Molecular Dynamics . . .	149
References	166

List of Tables

1.1	Parameters for bonds and angles in DREIDING.	18
1.2	Lennard-Jones parameters for DREIDING	20
1.3	Parameters for the TIP3P water model.	22
2.1	Partial charges in DHLA-Jeffamine	53
2.2	Thermal resistances of the interface	56
3.1	Melting temperature of different lipids.	74
5.1	Laser specifications.	100
5.2	Partial charges in decane.	114
6.1	Fitting parameters of the fluorescence decay on the GUV.	131

List of Figures

1.1	Phase space	9
1.2	Phonon dispersion relation of the gold.	23
1.3	Radial distribution function of oxygen in water	31
1.4	Definition of the viscosity with the speed gradient in a fluid.	40
1.5	Density of water as a function of the temperature.	42
2.1	Skeletal formula of DHLA-Jeffamine polymer.	52
2.2	Gold/water interfaces with different radius curvature of the gold surface.	54
2.3	Density profiles of water at the interface with gold.	55
2.4	Close view of the interface between the nanoparticle of 6.5 nm and water.	56
2.5	Gold/polymer/water interface description.	57
2.6	Autocorrelation function of the temperature difference fluctuations	59
2.7	Transmission function and densities of states in the gold/polymer/water system	60
2.8	Temperature profiles in water at the vicinity of the gold.	62
2.9	Space-time isotherm diagram.	63
2.10	Effective contact resistance extrapolated for higher polymer surface density on gold	65
3.1	Bilayer structure of lipids.	71
3.2	Micelles and vesicles.	71
3.3	The different phases of lipid bilayers	72
3.4	Lipid volume and heat capacity dependence on the temperature	73
3.5	Effect of unsaturated lipids (bottom) on lipid bilayer.	74
3.6	Electroporation mechanism	76
3.7	Transmembrane voltage during the action potential propagation	77
3.8	Electrical model of an axon	77
3.9	Heat release during the action potential propagation	78
4.1	Skeletal formulas of POPC and DPPC lipids	82
4.2	Representation of the lipid bilayers.	84
4.3	Size effect on the static polarisability of the lipid bilayer.	85

4.4	Size effect on the static permittivity in the plane of the lipid bilayer.	86
4.5	Static polarisability and electric capacity of lipid bilayers as function of temperature	87
4.6	In plane static permittivity of lipid bilayers as function of temperature.	88
4.7	Absorption spectrum, Raman spectroscopy and densities of states of DPPC and POPC bilayers.	89
4.8	Density and charge density in lipid bilayers.	91
4.9	Radial distribution function of lipid bilayers	92
4.10	Position dependant absorption in the lipid bilayer	94
5.1	Principle of phase contrast microscopy	99
5.2	Set-up of the FLIM experiments	101
5.3	Skeletal formula of the BODIPY.	101
5.4	Fluorescence lifetime as function of the viscosity.	102
5.5	Skeletal formula of a DPPC lipid.	102
5.6	Skeletal formula of decane.	103
5.7	Description of the chip for suspended lipid bilayers.	103
5.8	Procedure of the painting method.	104
5.9	Phase contrast and fluorescence images of the suspended lipid bilayer	105
5.10	FLIM image of the suspended bilayer	106
5.11	Fluorescence decays	107
5.12	Fluorescence lifetimes of the BODIPY in the lipid bilayer	108
5.13	Fluorescence lifetime with the corresponding viscosity	108
5.14	Fluorescence lifetime of the BODIPY in three different systems	110
5.15	Force between two DPPC lipid monolayers	111
5.16	Equilibrium distance between the two layers of the DPPC bilayer as function of the temperature.	112
5.17	Probability to split the bilayer	113
5.18	Thickness and surface of a decane molecule	115
5.19	Work needed to insert a decane molecule inside the bilayer	115
5.20	Probability to insert a decane molecule inside a lipid bilayer	116
5.21	Predicted viscosity of a mixing of decane and DPPC lipid bilayer	117
6.1	The different parts of the electroformation system	121
6.2	Phase contrast image of a GUV.	122
6.3	Images for the fluorescence anisotropy.	125
6.4	Fluorescence anisotropy in a GUV.	126
6.5	BODIPY used as fluorescent molecule.	126
6.6	Sketch of a GUV in a uniform electric field	128
6.7	Chip to apply voltage on the GUV	129
6.8	Phase contrast and fluorescence image of a GUV	129

6.9	FLIM images of a GUV at different at different temperatures and voltages.	130
6.10	Fluorescence lifetime as function of the peak to peak voltage on the electrodes	131
6.11	Viscosity as function of the transmembrane voltage on the GUV	133
6.12	Viscosity as function of the electrical energy	134
A.1	Example of non-ergodic system.	139
E.1	Autocorrelation function of the heat flux in water.	150
E.2	Thermal conductivity of water.	151

Introduction

Thermal transport in biological systems has recently gotten more attention thanks to new applications in medicine but bioheat transfer is an older field that first intended to model the heat transfer in biological systems for the design of devices and protocols in medicine. The difficulty of studying the heat transfer in biological and living systems is the mixing of several heat transfer mechanisms such as heat conduction, convection, phase change and the metabolism producing energy via chemical reactions.

Thus the thermal conductivity of many tissues have been measured and tabulated as the first data needed to model systems [84]. The models of heat transfer in biological systems explained the heat transfer in living bodies considering those experimental data and the blood vessels. These models allowed understanding several heat transfer problems in biology such as a better understanding of thermoregulation. These studies also allowed designing devices for therapeutic healing as increasing the temperature locally to 40°C or 42°C has analgesia and healing effects. It also has an effect on the kinetic of chemical processes in the body and can kill cells and tissues.

Cooling the tissues to subzero is also an important area of bioheat transfer. The studies of the effects of subzero temperatures played a key role in important applications such as transplantations. The effect of both high and low temperatures on living matter is deeply bonded to its effect on the cell properties. It is connected to the impact on the chemistry, to how cryoprotective additives enter in cells, to what happens to the different part of the cells when the temperature changes. If the cells are impacted, then the tissue is impacted. Thus, the study of the temperature effects at micrometric scales is central to understand thermal effects on tissues.

In today's most advanced researches in medicine and biology, local treatments are developed and microbiology tries to understand the micro-scale mechanism in cell biology. The cells are composed of many micro and nano-scale systems made of molecules and macromolecules, which the properties are the subject of intense studies. In this context, bioheat transfer is still an important field, but it used to consider large parts of bodies to be heated, and now, new hyperthermia techniques are local and target only the tissues one wants to act upon. In this context, the thermal conductivity of the tissues is not central any more. Instead the thermal properties of the cell components become relevant. This change of

dimension means a continuum model cannot model the heat transfer any more but one has to take into account the local organisation of the different elements. At this scale, it is known that interfaces between different materials become an important heat transfer properties in the models and sometimes the main one. The heat transfer in biological systems already involved many different aspects such as the phase transition, heat conduction and convection and when studying this transfer at the nanoscale, interfaces and surface effects also have to be considered and the importance of other phenomena such as the phase transition of small systems changes. On top of these differences, nanoscale systems are introduced into the cells to act upon them and these systems themselves require nanoscale modelling as part of their design.

Nano-engineered systems can be made for multiple applications. They can be used for imaging both *in vivo* and *in vitro*. Gold nanoparticles for instance are used for their high X-ray absorption and could increase the imaging contrast [58]. Or Quantum Dot can be used instead of fluorescent molecules [47, 57]. Or again iron-oxide nanoparticles to increase the contrast of magnetic resonance imaging [160, 20]. Other systems can be designed for local drug delivery; a nanodevice is introduced in the body and it will release a drug only where it is needed. This technique would reduce the side effects of treatments, which are major issues in chemotherapy for example. Lipid based systems in the form of liposomes or micelles [116, 102] are promising candidates for those applications. Another promising application of nanodevices in medicine is local hyperthermia treatment, using gold nanoparticles [131] or magnetic nanoparticles [69, 55, 101, 32]. Hyperthermia was already used as said before but it was done on a whole body or on large parts of a body. The possibility to increase the temperature locally leads to new methods to destroy targeted cells or release drugs or even both at the same time. In this context more than any other, studying the heat transfer at the microscale in living tissues becomes important for engineering nanodevices and modelling their behaviour in the biological environment. However, there are still few studies of the thermal properties of nanoscale biological systems and of those nanodevices.

In the work presented in this thesis, some parts of this problem are being addressed. One of these nanodevices for hyperthermia is modelled and a problem that is still unclear is addressed: the effect of polymer covering a nanoparticle on its heat transfer properties. However, understanding such system alone is not enough to model its behaviour in a living tissue. Considering the different subsystems and barriers in cells, one extensively studied system but which its thermal properties are mostly unknown is the plasma membrane. This membrane separates the interior of a cell from their outside environment. It is a central system for applications aiming to interact with a cell either from the outside, for instance when trying to fix a cell on a surface, or from the inside, this membrane is then one of the barriers to cross. As a result, when a device is designed to act on a cell, its interaction with the plasma membrane has to be taken into account. In particular, when the device's role is to release heat,

the plasma membrane's conductance plays a role. This plasma membrane is a very complex system. It is made of different types of lipids and proteins. The amphiphilic lipids self-organise in a bilayer and create a matrix made of several types of lipids hosting different proteins acting as pumps, channels, receptors, enzymes or structural components. This complexity makes this system difficult to study as a whole and it was decided to focus the study on only pure lipid bilayers made of one type of lipid. These systems are already very complex in terms of heat transfer and their heat transport properties are still mostly un-addressed. In this work, several aspects of these thermal properties were investigated from numerical simulations such as its absorption. Furthermore, these bilayers have the specificity to go through phase transitions, from a gel to a liquid phase, and this is important for both heat transfer and interactions with the bilayer. In particular, lipid bilayer would absorb heat to go to gel phase and thus if the phase transition is forced, the system would absorb heat as well. This effect is suspected to be at the origin of the heat flux from the axon membrane during the action potential propagation. This would be interesting for heat transfer in cells but also, if the membrane changes to the liquid phase when a voltage is applied on it, it is a way to control its phase and thus its associated properties such as its permeability.

This thesis is thus divided into three parts. The first part will only focus on first the theoretical methods and then the numerical method used along this thesis. Basics of statistical physics concepts and the fluctuation dissipation theorem are introduced in the first chapter and the second one details how they are applied in numerical simulations.

The second part of this thesis will present a study on a solid/liquid interface and the effect of a grafted polymer on the interface resistance. This is purely numerical work.

The third and last part of this thesis presents the work on lipid bilayers. It starts by a short introduction on lipid bilayers and their properties. The computation of the absorption and dielectric properties of lipid bilayers is then detailed. Finally, the last two chapters of this part concern experimental work. The effect of an electric field on the membrane's viscosity has been measured showing that structure of the bilayer can be changed by a voltage. The set-up and method used are explained in these chapters and the results are explained using also numerical simulations. The two chapters present measurements on different lipid bilayer systems. The first chapter considers experiments conducted on a suspended lipid bilayer while the measurements of the second chapter have been made on giant unilamellar vesicles.

Part I

Theory and methods

Chapter 1

Theoretical framework and Molecular Dynamics simulation methods

1.1	Introduction	8
1.2	Statistical ensembles and probability density	8
1.2.1	Probability density	9
1.2.2	Microcanonical ensemble (NVE)	10
1.2.3	Entropy	10
1.2.4	Canonical ensemble (NVT)	10
1.2.5	NPT ensemble	12
1.3	Molecular Dynamics simulation	13
1.3.1	Integration method: the Verlet algorithm	13
1.3.2	Boundaries	15
1.3.3	Interaction potentials	16
1.3.4	Gasteiger algorithm	23
1.3.5	PPPM algorithm	25
1.3.6	Thermostats	27
1.4	Computing physical properties using Molecular Dynamics simulations	27
1.4.1	Reaching equilibrium	28
1.4.2	The radial distribution function	28
1.4.3	The dielectric properties	32
1.4.4	Interface thermal resistance	35
1.4.5	Viscosity	39
1.4.6	Phase transition	40
1.4.7	Density of vibrational states	42
1.5	Conclusion	45

1.1 Introduction

This chapter focuses on the theoretical context and numerical methods of the work presented in this thesis. The main interest here is to present method to compute the quantities investigated in the following chapters which were mostly condensed matter properties defined in the 19th century. Most of these quantities were used to quantify the properties of matter seen as continuous media. That is the case for the thermal conductivity for instance. It was introduced by Joseph Fourier as a parameter in his famous law of heat diffusion [45]. This law is perfectly defined in continuous media and the thermal conductivity becomes an intrinsic property that characterises the material. However, when using a microscopic description of matter, the gradient of the temperature becomes difficult to define. Another theoretical frame is required in which those properties are now expressed from a microscopic point of view. This is the frame of statistical physics. However, this description requires following the evolution of a large number of particles which cannot be done analytically. As a result, numerical simulations are used to apply this theory without or with fewer approximations than in analytical developments. Several simulation techniques to model statistical ensembles exist but in this thesis, the models are based on Molecular Dynamics (MD).

The first section of this chapter presents the basics of statistical physics as the general theoretical frame of our work. Then, the second section describes how Molecular Dynamics is implemented to simulate statistical ensembles. In the last part, the statistical physics definitions of the quantities phenomenologically introduced in materials science is developed as well as the numerical method used to compute them from Molecular Dynamics. In several cases, expressions cited here are demonstrated for the sake of a key understanding or a simple interest.

1.2 Statistical ensembles and probability density

In this thesis, the numerical methods and concepts implemented are based on statistical physics. This is why a few reminders about statistical physics are presented here. A short summary is provided but several references can also support the calculations [130]. The general idea of statistical physics is to describe macroscopic properties from the behaviour of individual molecules composing the system. It is impossible of course to describe the movement of each molecule or each atom of a macroscopic system, which justifies the statistical approach. In this frame, the thermodynamic quantities must be defined, such as the pressure and the temperature, and the laws of thermodynamics are

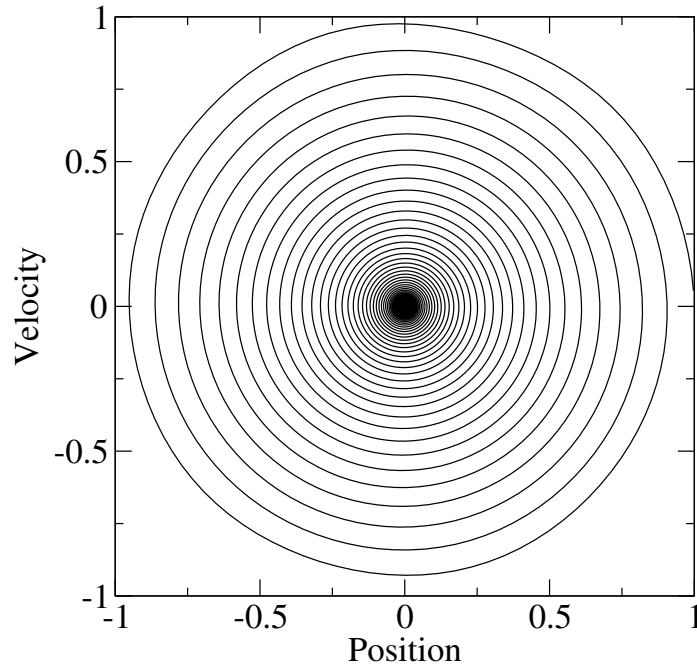


Figure 1.1: *Example of phase space. This curve represents the motion of a one-dimensional damped oscillator.*

derived from microscopic and statistical descriptions.

1.2.1 Probability density

From a classical point of view, a system of N particles is entirely described by the position and impulsion of each particle consisting in $6N$ components, i.e. a point in the phase space. The position of this point may depend on time and thus creates a curve on the phase diagram, as shown in Figure 1.1 for a one-dimensional damped oscillator. The macroscopic state of this system results from this microscopic state. However, there are several microscopic states that are macroscopically identical. Those states are explored during the fluctuations of the system. If one could measure the position and impulsion of each particle of a large collection of identical systems, an histogram of all states could be created and the probability law of the system could be deduced. The average defined by this probability law is called the ensemble average and the collection of systems is called statistical ensemble.

To build the probability density, one can imagine measuring the positions and impulsions of all particles of the same system but at different times. The average using this density probability is a temporal average and it is not always equal to the ensemble average. When they are equal the system is said to be ergodic but all systems are not ergodic. An example of non-ergodic system is given in Annexe A.

1.2.2 Microcanonical ensemble (NVE)

All the quantities defined in the frame of thermodynamics can be defined in statistical physics as an ensemble average, but this description requires the knowledge of the probability density of the states of the system. To address this problem, let us consider an isolated system at equilibrium. Its total energy is a constant and it determines the accessible states of the systems. The collection of the accessible states of an isolated system is called microcanonical ensemble sometimes noted NVE, for fixed number of particles N , fixed volume V and fixed energy E .

For an isolated system, it is postulated that all its accessible states have the same associated probability. This postulate is justify by the results of the theory based on this postulate and its agreement with experiments. Using this postulate, the usual thermodynamic quantities can be derived.

1.2.3 Entropy

Entropy has been first introduced as a thermodynamics quantity in the second law of thermodynamics and later Ludwig Boltzmann introduced an expression of the entropy, S , based on the probability density. It was then reformulated by Shannon in the information theory as follows, with k_B the Boltzmann constant:

$$S = -k_B \sum_i P_i \ln P_i. \quad (1.1)$$

However, this expression and whether the second law of physics only emerges from statistical physics or not is still debated specially concerning non-equilibrium statistical mechanics and irreversible processes [149, 31, 103]. This question will not be debated here and the Boltzmann expression will be used.

When the probability of each state is the same, as in the microcanonical ensemble, $P_i = \frac{1}{\Omega}$, Ω being the number of states yielding the entropy becomes:

$$\begin{aligned} S &= -k_B \sum_i P_i \ln P_i \\ &= k_B \sum_i \frac{1}{\Omega} \ln \Omega \\ &= k_B \ln \Omega \end{aligned} \quad (1.2)$$

The second principle of statistical physics states that the equilibrium probability density is the one that maximizes the entropy of the system.

1.2.4 Canonical ensemble (NVT)

Let us study a system that is not isolated but in contact with a thermal bath. It can exchange heat with this latter reservoir, as a result, its energy fluctuates but at equilibrium, its average value is fixed. This system creates a canonical

ensemble, noted NVT, for fixed number of particles N , fixed volume V and fixed temperature T . Consequently

$$\sum_i P_i = 1, \quad (1.3)$$

$$\sum_i P_i E_i = \langle E \rangle, \quad (1.4)$$

with E_i is the energy of state i and $\langle E \rangle$ is the average energy of the system. To find the probability law, the Lagrange multiplier methods can be used by introducing the multipliers λ_1 and λ_2 to find the maximum of the entropy:

$$-k_B \sum_i P_i \ln P_i + \lambda_1 \left(\sum_i P_i - 1 \right) + \lambda_2 \left(\sum_i P_i E_i - \langle E \rangle \right). \quad (1.5)$$

The derivation of P_k leads to

$$-k_B(1 + \ln P_k) + \lambda_1 + \lambda_2 E_k = 0, \quad (1.6)$$

thus,

$$P_i = e^{-1 + \frac{\lambda_1 + \lambda_2 E_i}{k_B}}, \quad (1.7)$$

which can be restated as

$$P_i = \frac{e^{-\beta E_i}}{Z}, \quad (1.8)$$

with Z the partition function

$$Z = \sum_i e^{-\beta E_i}, \quad (1.9)$$

and β is called the statistical temperature.

Using this probability law P_i ,

$$\langle E \rangle = \sum_i E_i P_i = \sum_i E_i \frac{e^{-\beta E_i}}{Z}. \quad (1.10)$$

In such a way that

$$\frac{\partial Z}{\partial \beta} = - \sum_i E_i e^{-\beta E_i}, \quad (1.11)$$

$$\frac{1}{Z} \frac{\partial Z}{\partial \beta} = - \sum_i E_i \frac{e^{-\beta E_i}}{Z}, \quad (1.12)$$

$$-\frac{\partial \ln Z}{\partial \beta} = \langle E \rangle. \quad (1.13)$$

β can now be identified by estimating the entropy S :

$$S = -k_B \sum_i P_i \ln P_i = -k_B \ln Z + k_B \beta \langle E \rangle. \quad (1.14)$$

Consequently,

$$\frac{\partial S}{\partial \langle E \rangle} = k_B \beta. \quad (1.15)$$

Finally, by identification with the thermodynamic expression,

$$\beta = \frac{1}{k_B T}. \quad (1.16)$$

1.2.5 NPT ensemble

In most cases studied in this manuscript, the systems do not have a fixed volume as they are in contact with a constant pressure bath, this systems are noted NPT. The probability law in this ensemble can be obtained with the same procedure as in NVT ensemble and adding the condition of fixed pressure P_r .

$$\sum_i P_i = 1, \quad (1.17)$$

$$\sum_i P_i E_i = \langle E \rangle, \quad (1.18)$$

$$\sum_i P_i V_i = \langle V \rangle. \quad (1.19)$$

Let us find the probability law by deriving the following expression with respect to P_k :

$$-k_B \sum_i P_i \ln P_i + \lambda_1 \left(\sum_i P_i - 1 \right) + \lambda_2 \left(\sum_i P_i E_i - \langle E \rangle \right) + \lambda_3 \left(\sum_i P_i V_i - \langle V \rangle \right).$$

Leading to the probability law:

$$P_i = \frac{e^{-\beta E_i + \lambda_2 V_i}}{Z}, \quad (1.20)$$

with

$$Z = \sum_i e^{-\beta E_i + \lambda_2 V_i}. \quad (1.21)$$

The entropy is written:

$$S = k_B \beta \langle E \rangle + k_B \ln Z - \lambda_2 k_B \langle V \rangle. \quad (1.22)$$

λ_2 is identified using

$$\begin{aligned} T \frac{\partial S}{\partial \langle V \rangle} &= P_r, \\ &= -\lambda_2 k_B T. \end{aligned}$$

This relation defines the pressure P_r . Finally, using the enthalpy, $H = E + VPr$, the probability law is obtained

$$P_i = \frac{e^{-\beta H}}{Z}. \quad (1.23)$$

This expression is thus very similar to the one of the canonical ensemble. These relations can be generalized to different quantities, in particular when the number of particles N can vary, this ensemble is called grand canonical ensemble.

1.3 Molecular Dynamics simulation

Molecular dynamics is a numerical tool that simulates the temporal behaviour of an ensemble of particles. This method is ideal to access time scales from one femtosecond of a few nanoseconds and sizes of a few nanometers. It is based on Newton's second law of motion and it is thus deterministic and classical. The equations of motion of the ensemble of particles are solved in an iterative way using an interaction model. Thus the simulation explores the phase space of the modelled system and the set of trajectories and velocities is computed and used to compute the temperature, the pressure and several other properties using statistical physics equations or non-equilibrium regimes. The simulations presented in this work have been performed using Large-scale Atomic/Molecular Massively Parallel Simulator (LAMMPS) [126].

1.3.1 Integration method: the Verlet algorithm

Let be an ensemble of N particles in an isolated system of volume V . The Hamiltonian H of this system writes

$$H = \sum_{i=1}^N \frac{1}{2} m_i \dot{\vec{r}}_i^2 + U(r_1, \dots, r_i, \dots, r_N), \quad (1.24)$$

where \vec{r}_i is the position and m_i is the mass of atom i .

With $\vec{f}_i = \frac{\partial U}{\partial \vec{r}_i}$ the force applied on atom i , the equation of motion for each atom i is

$$m_i \ddot{\vec{r}}_i = \vec{f}_i. \quad (1.25)$$

These are $3N$ coupled equations that can be solved numerically using the Verlet algorithm [173]. \vec{r}_i is expanded in a Taylor series at the time $t + \delta t$ and combining the result with Eq. 1.25:

$$\begin{aligned} \vec{r}_i(t + \delta t) &= \vec{r}_i(t) + \delta t \dot{\vec{r}}_i(t) + \frac{\delta t^2}{2} \ddot{\vec{r}}_i(t) + \frac{\delta t^3}{6} \overset{\curvearrowright}{\ddot{\vec{r}}_i}(t) + \mathcal{O}(\delta t^4), \\ &= \vec{r}_i(t) + \delta t \dot{\vec{r}}_i(t) + \frac{\delta t^2}{2} \frac{\vec{f}_i(t)}{m_i} + \frac{\delta t^3}{6} \overset{\curvearrowright}{\ddot{\vec{r}}_i}(t) + \mathcal{O}(\delta t^4), \end{aligned}$$

and at $t - \delta t$

$$\vec{r}_i(t - \delta t) = \vec{r}_i(t) - \delta t \vec{\dot{r}}_i(t) + \frac{\delta t^2}{2} \frac{\vec{f}_i(t)}{m_i} - \frac{\delta t^3}{6} \vec{\ddot{r}}_i(t) + \mathcal{O}(\delta t^4). \quad (1.26)$$

By summing those two relations

$$\vec{r}_i(t + \delta t) = 2\vec{r}_i(t) - \vec{r}_i(t - \delta t) + \delta t^2 \frac{\vec{f}_i(t)}{m_i} + \mathcal{O}(\delta t^4). \quad (1.27)$$

The velocity can be expressed as

$$\vec{v}_i(t) = \frac{\vec{r}_i(t + \delta t) - \vec{r}_i(t - \delta t)}{2\delta t} + \mathcal{O}(\delta t^2). \quad (1.28)$$

This means that the positions of the atoms can be computed at step $t + \delta t$ with the position at steps t and $t - \delta t$ and the forces computed at step t and with a precision in $\mathcal{O}(\delta t^4)$. Furthermore, this expression does not involve the velocity of the atoms.

In this algorithm, two consecutive initial conditions have to be stated as well as the time step δt .

1.3.1.1 Choosing δt

The time parameter has to be small enough to fully capture the dynamics of the system. For instance, all vibrations of the system must be included. Considering the highest frequency of the system ω_{max} , 100 time steps per vibrational period is required to ensure an accurate resolution. The consequent constraint on the time step writes:

$$\omega_{max} \delta t < 0.01. \quad (1.29)$$

The time step is usually chosen as

$$\delta t = \frac{0.01}{\omega_{max}}. \quad (1.30)$$

In the systems considered in this manuscript, the highest frequency is typically the one associated to the C-H bonds which vibrate at a frequency of about 90 THz yielding a time step of $\delta t = 0.1$ fs.

1.3.1.2 Initial conditions

In the Verlet algorithm, two consecutive time steps are required to compute a third one. As a result, two initial conditions are needed. At $t = 0$, the positions of all atoms are set depending on the system to model: a crystal, a liquid, a gas, etc ... For instance, the initial positions of the atoms of a liquid are set as a crystal having the same density as the liquid and enough energy to ensure a liquid phase. The second time step is computed as

$$\vec{r}_i(t + \delta t) = \vec{r}_i(t) + \delta t \vec{\dot{r}}_i(t) + \frac{\delta t^2}{2} \frac{\vec{f}_i(t)}{m_i} + \mathcal{O}(\delta t^3). \quad (1.31)$$

In this equation, the velocities of the atoms at $t=0$ must be known. Setting the initial velocities is the way to set the initial energy of the system. The model being classical, the equipartition theorem can be used to set the velocities corresponding to a given temperature. Here, this theorem states that (see Annexe B):

$$\frac{1}{N} \sum_{i=1}^N \frac{1}{2} m_i \vec{v}_i^2 = \frac{3}{2} k_B T. \quad (1.32)$$

Using this constraint, the velocities are drawn according to a Gaussian distribution. If no other constraint is imposed the system might rotate on itself or be in translation and the system can leave its initial volume. These motions can be avoided by making sure that the total momentum cancels

$$\sum_{i=1}^N m_i \vec{v}_i = \vec{0}. \quad (1.33)$$

Following the same process, the total angular momentum is set to zero

$$\sum_{i=1}^N (\vec{r}_i - \vec{r}_0) \times m_i \vec{v}_i = \vec{0}. \quad (1.34)$$

This relation does not depend on the choice of \vec{r}_0 as long as $\sum_{i=1}^N m_i \vec{v}_i = \vec{0}$. For instance, the momentum from \vec{r}_0' writes

$$\begin{aligned} \sum_{i=1}^N (\vec{r}_i - \vec{r}_0') \times m_i \vec{v}_i &= \sum_{i=1}^N (\vec{r}_i - \vec{r}_0 + \vec{r}_0 - \vec{r}_0') \times m_i \vec{v}_i \\ &= \underbrace{\sum_{i=1}^N (\vec{r}_i - \vec{r}_0) \times m_i \vec{v}_i}_{=0} + \sum_{i=1}^N (\vec{r}_0 - \vec{r}_0') \times m_i \vec{v}_i \\ &= (\vec{r}_0 - \vec{r}_0') \times \underbrace{\sum_{i=1}^N m_i \vec{v}_i}_{=0} \\ &= \vec{0} \end{aligned} \quad (1.35)$$

1.3.2 Boundaries

The Verlet algorithm has been described but if the system is a fluid, the particles occupy the total space and hit the boundaries of the volume and thus boundary conditions are needed. There are two main ways to consider the boundaries in Molecular Dynamics. The most common one is to use periodical boundary conditions: every particle that is leaving the box is simultaneously entering in the system from the opposite side. This simple way to solve the problem

of boundaries is also used to simulate an infinite "bulk" system. The other method is to prevent the particles from leaving the volume by setting walls. There are several types of walls:

- static atoms with a velocity kept at zero at the limit of the volume. Those atoms will interact with the rest of the simulated atoms.
- a force between the boundary itself and the atoms.
- reflecting atoms that are leaving the volume. If an atom is crossing a boundary, it is instead repositioned on its original side as its symmetric with respect to the boundary plane.

All those methods are relevant in certain conditions depending on the system and the objective of the simulation but in most of the work reported in this thesis, the periodic boundary conditions or reflective walls are preferred mostly because they do not modify the energy of the system as no force is added.

1.3.3 Interaction potentials

The forces applied to each atom are needed to compute the new steps in the Verlet algorithm. The choice of these forces is a central part of the modelling in Molecular Dynamics simulations. In this thesis, a limited number of interaction potentials has been used and they are described in this section.

1.3.3.1 DREIDING interaction model

The DREIDING model [110] is a generic model for polymer modelling. It is meant to be convenient to model organic materials and to add atoms to the model. A description of this model and how to use it in Molecular Dynamics simulations is proposed here.

1.3.3.1.1 Atom description

The atoms in this model are explicitly represented. They are defined by their element, for example H for hydrogen atoms, and by their hybridization or geometry if it is relevant (1 for linear, 2 for trigonal or 3 for tetrahedral). For example, C_3 is the carbon present in ethane. The model includes the possibility to use implicit hydrogen atoms, for instance C_32 is a tetrahedral carbon with two implicit hydrogen atoms but this is not used in the following studies. An ensemble of parameters is associated to each atom, which will be used to compute the parameters of the interaction potentials.

1.3.3.1.2 Potential energy form

In DREIDING, the potential energy is defined as follows:

$$E = E_b + E_a + E_t + E_i + E_{vdw} + E_c, \quad (1.36)$$

where E_b , E_a , E_t , E_i , E_{vdw} and E_c are respectively the bonded two-body, the bonded three-body, the bonded four-body, the inversion bonded four-body, the

non-bonded two-body and the electrostatic interaction energies. Each of those potential energies is computed separately.

1.3.3.1.3 Bonded two-body interactions

A simple potential for a two-body interaction energy is the one of a simple oscillator:

$$E_b = \frac{1}{2}K(r - r_e)^2, \quad (1.37)$$

where K is the bond stiffness and r_e is the equilibrium distance between the atoms.

A more accurate way to consider this interaction energy is the Morse potential:

$$E_b = D_e[e^{-\alpha(r-r_e)} - 1]^2, \quad (1.38)$$

where D_e is dissociation energy of the bond and r_e the equilibrium distance of the bond.

The two previous models are linked by:

$$\alpha = \left[\frac{K}{2D_e} \right]^{\frac{1}{2}}. \quad (1.39)$$

The interaction energy of the Morse potential converges to zero when the distance between the two atoms becomes large. To ensure a non-negligible interaction, harmonic potential are used at the beginning of the simulation where the atoms can be far from their equilibrium positions.

The length parameter of this bond is computed as:

$$r_e = r_i + r_j - \delta, \quad (1.40)$$

where i, j are the atom types of the bonded atoms and $\delta = 0.01 \text{ \AA}$. The parameter r_i and r_j are given in the original article presenting the DREIDING model reported on Table 1.1.

The other bond constants are set to:

$$K_e = 700.n \text{ kcal.mol}^{-1}.\text{\AA}^2, \quad (1.41)$$

$$D_e = 70.n \text{ kcal.mol}^{-1}.\text{\AA}^2, \quad (1.42)$$

where n is the bond order.

1.3.3.1.4 Bonded three-body interactions

The three-body potential imposes the angle bending between two atoms connected to a third one. It is modelled by:

$$E_a = \frac{1}{2}K_\theta[\theta - \theta_0]^2, \quad (1.43)$$

with

$$K_\theta = 100 \text{ kcal.mol}^{-1}.\text{rad}^{-2}, \quad (1.44)$$

θ_0 being considered independent of the types of the two atoms bonded to the central one. The angle parameters are given in Table 1.1 for each atom type.

Atom	bond radius (Å)	bond angle (°)	atom	bond radius (Å)	bond angle (°)
H_	0.330	180.0	Si3	0.937	109.471
B_3	0.880	109.471	P_3	0.890	93.3
S_3	1.040	92.1	Cl	0.997	180.0
B_2	0.790	120.0	Ga3	1.210	109.471
C_3	0.770	109.471	Ge3	1.210	109.471
C_R	0.700	120.0	As3	1.210	92.1
C_2	0.670	120.0	Se3	1.210	90.6
C_1	0.602	180.0	Br	1.167	180.0
N_3	0.702	106.7	In3	1.390	109.471
N_R	0.650	120.0	Sn3	1.373	109.471
N_2	0.615	120.0	Sb3	1.432	91.6
N_1	0.556	180.0	Te3	1.280	90.3
O_3	0.660	104.51	I_	1.360	180.0
O_R	0.660	120.0	Na	1.860	90.0
O_2	0.560	120.0	Ca	1.940	90.0
O_1	0.528	180.0	Fe	1.285	90.0
F_	0.611	180.0	Zn	1.330	109.471
Al3	1.047	109.471			

Table 1.1: Parameters for bonds and angles in DREIDING. Each atom is identified by its element and oxidation number. Parameters for bonds and angles are used to compute bonded potential parameters and angle parameters [110].

1.3.3.1.5 Bonded four-body interactions

The first four-body interaction to consider is the interaction involved by two angles having a common bond. The atoms i , j , k and l with i bonded to j , j to k and k to l , form two angles in ijk and jkl . A potential is added to represent the torsion of this chain, which takes the form:

$$E_d = \frac{1}{2}V[1 - \cos(n(\psi - \psi_0))], \quad (1.45)$$

where V is the rotation barrier, ψ the angle between the planes formed by each angle, ψ_0 the equilibrium angle and n is the periodicity. The parameters V , n and ψ_0 are considered independent to the two extreme atoms of the angles. For instance, the angles involved in the atoms i , j , k and l above only depend on j and k . V here is the total barrier relevant for any possible angle. As an example, ethane ($\text{H}_3\text{C}-\text{CH}_3$) involves nine options where the carbon atom is at the center. Thus, each H-C-C-H has a barrier of $\frac{V}{9}$. The parameters V , n and ψ_0 are defined in the following cases:

- the two central atoms are sp3 atoms (X_3):

$$V = 2 \text{ kcal.mol}^{-1} \quad n = 3 \quad \psi_0 = 180^\circ. \quad (1.46)$$

- one of the central atoms in a sp3 atom and the other is a sp2 atom (for instance the C-C bond in $\text{H}_3\text{C}-\text{COOH}$):

$$V = 1 \text{ kcal.mol}^{-1} \quad n = 6 \quad \psi_0 = 0^\circ. \quad (1.47)$$

- the two atoms are sp2 atoms (X_2):

$$V = 45 \text{ kcal.mol}^{-1} \quad n = 2 \quad \psi_0 = 180^\circ. \quad (1.48)$$

- the two central atoms are resonant atoms (bond order is 1.5) (X_R):

$$V = 25 \text{ kcal.mol}^{-1} \quad n = 2 \quad \psi_0 = 180^\circ. \quad (1.49)$$

- the two central atoms are resonant or sp2 atoms (as in betadine):

$$V = 5 \text{ kcal.mol}^{-1} \quad n = 2 \quad \psi_0 = 180^\circ. \quad (1.50)$$

Or if the atoms are exocyclic aromatic atoms, $V = 10$.

- one of the central atoms is a sp1 atom (X_1):

$$V = 0 \text{ kcal.mol}^{-1}$$

- the two central atoms are sp3 atoms of the oxygen column:

$$V = 2 \text{ kcal.mol}^{-1} \quad n = 2 \quad \psi = 90^\circ \quad (1.51)$$

- one of the two central atoms is a sp3 atom of the oxygen column and the other is a sp2 or resonant atom:

$$V = 2 \text{ kcal.mol}^{-1} \quad n = 2 \quad \psi = 180^\circ$$

- one of the two central atoms is a sp3 atom and the other is a sp2 or resonant atom while they are not bonded to a sp2 or resonant atom:

$$V = 2 \text{ kcal.mol}^{-1} \quad n = 3 \quad \psi = 180^\circ$$

Atom	r_0	D_0 (kcal.mol ⁻¹)	Atom	r_0	D_0 (kcal.mol ⁻¹)
H	3.20	0.01	N	3.6950	0.1450
O	3.5100	0.2150	C	3.8800	0.0950
F	3.2850	0.3050	Na	3.1440	0.5000
Al	4.6150	0.0650	Si	4.4350	0.0950
P	4.2950	0.2150	S	4.1400	0.2150
Cl	3.9150	0.3050	Br	4.2150	0.3050
Ca	3.4720	0.00500	Ti	4.5400	0.0550
Fe	3.4720	0.00500	Zn	4.5400	0.0550
Ru	3.4720	0.00500			

Table 1.2: Lennard-Jones parameters for DREIDING allowing to compute the parameters for the van der Waals interaction modelled by a Lennard-Jones potential. These values are considered independent from the oxidation number [110]

1.3.3.1.6 Inversion bonded four-body interaction

When an atom i is bonded to exactly three atoms j,k and l , the four atoms can be in a plane. A potential is needed to make the right position favourable. Here DREIDING proposes:

$$E_i = K(1 - \cos\phi).$$

ϕ refers to the angle between the bond il and the plane ijk . In DREIDING, all three possible potentials are defined for the group of four atoms and the total barrier is thus divided by three. The parameter K depends on the central atom only (X_2 , X_R) and is equal to $K = 40$ kcal.mol⁻¹.

1.3.3.1.7 Van der Waals interaction

Bonded interactions exist inside a molecule that builds up its structure. Those are the interactions inside a molecule that make its structure. There are also non-bonded interactions between molecules and between the non-bonded atoms inside a molecule. There are two interactions to take into account, the first one is the van der Waals interactions for which DREIDING considers a 12-6 Lennard-Jones:

$$E_{vdw} = D_0(\rho^{12} - 2\rho^6), \quad (1.52)$$

with $\rho = \frac{r}{r_0}$, D_0 represents the well depth and r_0 the van der Waals bond length. They are defined as follows:

$$r_0 = \frac{r_0(\text{atom 1}) + r_0(\text{atom 2})}{2}, \quad (1.53)$$

$$D_0 = \sqrt{D_0(\text{atom 1}) \cdot D_0(\text{atom 2})}. \quad (1.54)$$

All parameters are gathered in Table 1.2.

It is important to note that the non-bonded interaction energies are not calculated between atoms bonded to each other. This interaction is also independent of the hybridization.

1.3.3.1.8 Electrostatic interactions

The potential itself takes the usual form:

$$E_c = \frac{q_i q_j}{4\pi\epsilon_0 r}, \quad (1.55)$$

in kcal.mol⁻¹ with q_i and q_j the charges of atoms i and j . This interaction energy is not computed between bonded atoms or atoms in the same angle. The difficulty here is the choice of the charges for which the Gasteiger algorithm [49] can be used. The computation of the electrostatic interaction itself is implemented using the PPPM algorithm [63] with a 12 Å cut-off. Those algorithms are detailed later in this chapter.

1.3.3.1.9 Conclusion

The DREIDING model is a generic force field for organic molecules, this potential is flexible and easy to implement in LAMMPS. It is important to mention AMBER [19], GROMAC [171] and CHARMM [17] that are other force fields and codes of the same kind but with parameters fitted for specific applications.

Other models have been developed that do not simulate all the atoms. Those are called coarse-grain models and allow for time steps of more than several fs, among which the common example of the MARTINI model.

1.3.3.2 TIP3P water model

In several places of the thesis work, water is part of the simulated systems. The Molecular Dynamics simulations implemented in the following are based on the TIP3P water model [74]. This model is chosen for its satisfying match with DREIDING. Indeed, this model includes:

- 3 atoms per water molecule, two hydrogen atoms and one oxygen atom.
- harmonic bonds between the oxygen and the hydrogen atoms.
- harmonic angle for the H-O-H angle (same potential as in DREIDING angles).
- Lennard-Jones potentials for long range interactions.
- partial charges to compute the electrostatic interactions using the PPPM algorithm.

The parameters used in this model are gathered in Table 1.3.

These parameters can be set in the rigid water molecule model by using the shake algorithm [143]. This allows increasing the time step up to 0.5 fs.

Other notable water models can be cited such as the SPC model [167] and the TIP4P one [1] that are both commonly used.

1.3.3.3 MEAM potential

MEAM is a modified version of the Embedded-Atom Method (EAM) designed for metals [154] to study impurities. MEAM, the Modified Embedded-Atom

Table 1.3: *Parameters for the TIP3P water model.*

Parameter	value	units
O mass	15.9994	g.mol ⁻¹
H mass	1.008	g.mol ⁻¹
O charge	-0.830	multiple of absolute electron charge
H charge	0.415	multiple of absolute electron charge
OO Lennard-Jones well depth	0.102	kcal.mol ⁻¹
OO Lennard-Jones bond length	3.188	Å
OH Lennard-Jones well depth	0.0	kcal.mol ⁻¹
OH Lennard-Jones bond length	0.0	Å
HH Lennard-Jones well depth	0.0	kcal.mol ⁻¹
HH Lennard-Jones bond length	0.0	Å
Stiffness of O-H bond	450	kcal.mol ⁻¹ .Å ⁻²
Equilibrium distance of O-H bond	0.9572	Å
Stiffness of H-O-H angle	55	kcal.mol ⁻¹ .rad ⁻²
Equilibrium angle of H-O-H angle	104.52	rad

Method, extends the EAM method to a large number of cubic materials [12], metals and semiconductors. This method is based on the effective medium theory and considers an electronic environment interacting with the atoms. The energy of atom i is the energy to place this atom at position R_i considering the electronic environment generated by the other atoms of the crystal. Thus the energy of the crystal is given by:

$$E = \sum_i \left(F(\rho_i) + \sum_{j \neq i} \Phi_{ij}(R_{ij}) \right), \quad (1.56)$$

where ρ_i is the electron density of the crystal missing atom i and F is called the embedding energy. Φ is a pair potential considering only the nearest neighbours with repulsive and attractive components. Their analytic forms depend on the element considered and can be modified for alloys [12, 89]. While this is achieved in EAM, MEAM adds a screening in both the embedding energy and the pair potential of this model. Because when the atom i is added between two atoms, they do not interact with each other as strongly as when atom i is excluded. In this thesis, this potential is used to model gold crystals, which parameters can be found in [97]. Using MEAM for gold crystals, its phonon dispersion relation can be computed and are represented in Figure 1.2. The comparison of these results with experimental data [105] shows that high frequencies are underestimated and that the branches are significantly flatter than the experimental ones.

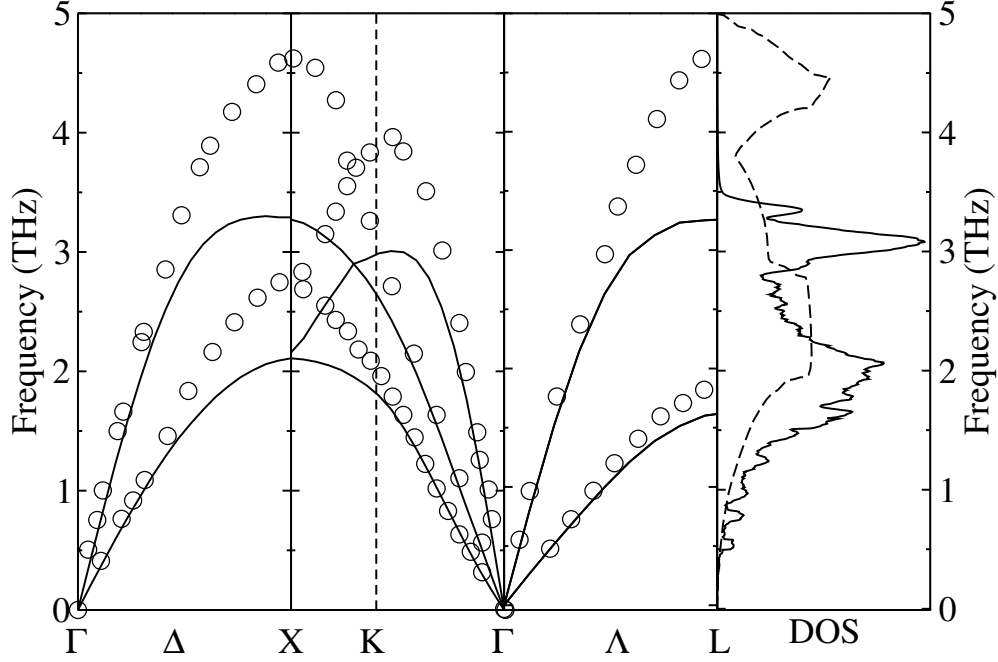


Figure 1.2: Phonon relation dispersion of MEAM gold (solid lines) and experimental data (circles and dashed line) [105]

1.3.4 Gasteiger algorithm

Polymers and biomolecules modelled possess many dipoles and local charges that are modelled by given a partial charge to each atom of the molecule. The Gasteiger algorithm [49] is a simple algorithm to compute those partial charges on the atoms of a molecule. This method is fast and easy to implement. The algorithm only requires the definition of the atoms of the molecule of interest and how they are bonded. The model is also based on the electronegativity χ of the atoms as defined by Mulliken, which is expressed from the ionization potential I and the electron affinity E as

$$\chi = \frac{I + E}{2}. \quad (1.57)$$

For the dependence to charge q , a second order polynomial has been chosen:

$$\chi(q) = a + bq + cq^2. \quad (1.58)$$

The parameters a , b and c are set to fit experimental data:

$$\chi(q=0) = a = \frac{I(q=0) + E(q=0)}{2}, \quad (1.59)$$

$$\chi(q=1) = a + b + c = \frac{I(q=1) + E(q=1)}{2}, \quad (1.60)$$

$$\chi(q=-1) = a - b + c = \frac{I(q=-1) + E(q=-1)}{2} = \frac{E(q=0)}{2}, \quad (1.61)$$

$$(1.62)$$

because the ionization potential of the negative ion is equal to the electron affinity of the uncharged state and its electron affinity is assumed to be zero. As a result:

$$\begin{aligned} a &= \frac{I(q=0) + E(q=0)}{2}, \\ b &= \frac{I(q=1) + E(q=1) - E(q=0)}{4} \\ c &= \frac{I(q=1) - 2I(q=0) + E(q=1) - E(q=0)}{4} \end{aligned} \quad (1.63)$$

The values for $E(q=-1,0)$ and $I(q=0,1)$ can be found in the literature and it is easy to add an atom to a pre-existing algorithm.

When two atoms are bonded in a molecule, say A and B ($\chi^A > \chi^B$), charges are transferred from B to A, but then the electrostatic energy makes it harder for A to get more charges. This is taken into consideration in the equation calculating the charge transfer between atoms A and B:

$$q_t = \frac{\chi^A(q) - \chi^B(q)}{\chi^A(q=1)} \left(\frac{1}{2}\right)^\alpha, \quad (1.64)$$

which is iteratively computed, α being the iteration order. The first charge transferred is calculated using χ at $q=0$. Then the charges of the atoms are used in χ . The total charge consists in the total of all charges transferred at each iteration step. For polyatomic molecules, all neighbours of the atom A_i are considered in the same iterative step:

$$q_t = \left[\sum_{\chi^{A_k} > \chi^{A_i}} \frac{\chi^{A_k}(q) - \chi^{A_i}(q)}{\chi^{A_k}(q=1)} + \sum_{\chi^{A_j} < \chi^{A_i}} \frac{\chi^{A_j}(q) - \chi^{A_i}(q)}{\chi^{A_i}(q=1)} \right] \left(\frac{1}{2}\right)^\alpha. \quad (1.65)$$

This method usually converges after about ten iterations.

This algorithm were coded in C++ and its results successfully compared with the reference [49].

To conclude, the Gasteiger algorithm provides a simple and fast way to compute partial charges on any molecule. However, this method is not exact and the

optimal method to get the partial charges on molecule atoms is to compute the electrostatic potential around the molecule using *ab initio* techniques and fit the potential profile with the partial charges as fitting parameters. Having described a method to compute the partial charges the next step is to describe the method to compute the electrostatic potential in Molecular Dynamics.

1.3.5 PPPM algorithm

The Particle-Particle Particle-Mesh algorithm (PPPM or P3M) [63] is an algorithm developed to accurately and rapidly compute the electrostatic interactions in Molecular Dynamics simulations. In an ensemble of N charged particles in a volume V (L^3) with periodic boundary conditions, the electrostatic interaction of particle j on particle i is expressed by:

$$\begin{aligned} E_i &= \frac{q_i q_j}{4\pi\epsilon_0 |\vec{r}_i - \vec{r}_j + \vec{n}L|} \\ &= q_i \Phi_j(\vec{r}_i) \end{aligned} \quad (1.66)$$

Thus the total electrostatic energy of atom i is

$$E_i = \sum_{j \neq i} q_i \Phi_j(\vec{r}_i) + \sum_{\vec{n} \neq \vec{0}} \sum_{j=1}^N q_i \Phi_j(r_i). \quad (1.67)$$

So the total electrostatic energy is written as:

$$E = \sum_i E_i. \quad (1.68)$$

In Molecular Dynamics simulations, the distances under consideration are short (≈ 1 nm), while the electrostatic potential decreases as $\frac{1}{r}$. Consequently, this interaction is of longer range than the Lennard-Jones interaction and thus it cannot be neglected even in the periodic images of the system.

PPPM is an algorithm developed to compute this energy by applying an idea proposed by Ewald in reference [40]. The method consists in dividing the electrostatic interactions into a short range and a long range part. To achieve this, two charge distributions are created. The true charge distribution ρ_{true} is:

$$\rho_{true}(\vec{r}) = \sum_{i=1}^N q_i \delta(\vec{r} - \vec{r}_i). \quad (1.69)$$

A fictive distribution ρ_{short} that quickly converges in the direct space is introduced:

$$\rho_{short}(\vec{r}) = \rho_v(\vec{r}) - \sum_{i=1}^N q_i \left(\frac{\alpha}{\pi}\right)^{\frac{3}{2}} e^{-\alpha(\vec{r}-\vec{r}_i)^2}, \quad (1.70)$$

where α is a parameter setting the spatial extension of the function. Note that if $r \gg \sqrt{\frac{1}{\alpha}}$, which implies that the gaussian function is equivalent to a dot

and that ρ_{short} is almost equal to zero. The gaussian density, ρ_{long} , is defined as:

$$\rho_{long}(\vec{r}) = \sum_{i=1}^N q_i \left(\frac{\alpha}{\pi}\right)^{\frac{3}{2}} e^{-\alpha(\vec{r}-\vec{r}_i)^2}, \quad (1.71)$$

and converges quickly in the reciprocal space. The resulting density expression reads:

$$\rho_{true} = \rho_{short} + \rho_{long}. \quad (1.72)$$

The potential created by those two distributions can now be computed and the superposition theorem can be used to get the real potential:

$$\Delta\Phi_{long} = 4\pi\rho_{long}, \quad (1.73)$$

$$\Delta\Phi_{short} = 4\pi\rho_{short}. \quad (1.74)$$

Eq. 1.73 can be solved using the Fourier transform, which leads to the potential

$$E_{long} = \sum_{l=1}^N \sum_{j=1}^N N \sum_{\vec{k}} \frac{4\pi q_l q_j}{L^3 k^2} e^{i\vec{k} \cdot (\vec{r}_l - \vec{r}_j) - \frac{k^2}{4\alpha}}, \quad (1.75)$$

and corrected by removing the interaction of atom u with itself to obtain:

$$E_{long} = \sum_{l=1}^N \sum_{j=1}^N N \sum_{\vec{k}} \frac{4\pi q_l q_j}{L^3 k^2} e^{i\vec{k} \cdot (\vec{r}_l - \vec{r}_j) - \frac{k^2}{4\alpha}} - \left(\frac{\alpha}{\pi}\right)^{\frac{1}{2}} q_l^2. \quad (1.76)$$

The solution of equation 1.74 can be expressed as:

$$E_{short} = \sum_{i=1}^N \sum_{j>i} \frac{q_i q_j}{|\vec{r}_i - \vec{r}_j|} \operatorname{erfc}(\sqrt{\alpha}|\vec{r}_i - \vec{r}_j|), \quad (1.77)$$

where erfc denotes the complementary error function. The distance up to which this interaction is computed is usually set at 12 Å. The remaining task consists in choosing the parameter α .

This procedure is called the Ewald method, which is fast but another method, using the same idea can be faster. It is the Particle-Particle Particle-Mesh method, or PPPM (or even P3M). The difference with the Ewald method relies on how the long range potential is evaluated. First, ρ_{long} is computed, second, the charge density is interpolated on a regular mesh with a imposed resolution. Finally the Fast Fourier transform algorithm is used to compute the potentials. Those are then interpolated at the ions positions to compute the forces. This method is faster than the Ewald algorithm, mainly thanks to the use of the Fast Fourier Transform. In this thesis, the PPPM algorithm is used to compute the electrostatic interactions as it is commonly used to simulate organic materials.

1.3.6 Thermostats

Up to this point, the system was simulated in the microcanonical ensemble (NVE). No element is able to change the energy, the volume or the number of particles in the system during the simulation. The Verlet algorithm ensures the energy conservation, as it is invariant by the reverse time transformation.

However in most cases, the simulations are run in the canonical ensemble or even in NPT (constant number of particles, constant pressure and constant temperature). To achieve this goal, several methods have been elaborated and one of the most common is a thermostating method called Nosé-Hoover [65, 122].

The principle consists in coupling the atoms of the system to a heat bath of temperature T . The positions are scaled to let the volume V change and reach a target pressure P_{ext} . The following motion equations were employed with x , the position, p , the impulsion and F , the force:

$$\begin{aligned}\dot{x} &= \frac{p}{mV^{\frac{1}{3}}}, \\ \dot{p} &= F - (\epsilon + \zeta)p,\end{aligned}$$

with

$$\begin{aligned}\dot{\zeta}Q &= \sum \frac{p^2}{m} - 3Nk_B T, \\ \dot{\epsilon} &= \frac{\dot{V}}{3V}, \\ \ddot{\epsilon} &= \frac{(P - P_{ext})V}{\tau^2 k_B T},\end{aligned}$$

where Q is the parameter of the thermostat and τ the one of the barostat. Hoover has shown [65] that these equations allow recovering the NPT ensemble.

1.4 Computing physical properties using Molecular Dynamics simulations

The method used to simulate an ensemble of interacting particles was exposed in the previous section. Those ensembles can be considered as those treated in statistical physics. This section exposes the definitions of some condensed matter properties used in this thesis and how they can be expressed in the frame of statistical physics, mostly using the linear response theory. The method using these expressions to compute the physical quantities from a Molecular Dynamics model is then exposed. As a recall, Molecular Dynamics being a classical method, quantum effects cannot be represented with these simulations. As a result, only the classical version of statistical physics is useful and the equipartition of energy is valid as explained in Annexe B.

1.4.1 Reaching equilibrium

The first step when conducting a Molecular Dynamics simulation is to equilibrate the system. The first structure imposed via atomic positions has to be as physical as possible but it remains difficult to *a priori* find the equilibrium positions, especially in fluids. During the first steps, the system evolves significantly and rapidly towards a final stage. This latter can be reached after a few nanoseconds but this duration depends on the system and is usually about a few picoseconds. A relevant technique to verify that the equilibrium is reached is to check the potential and kinetic energies but other parameters can be of interest, especially when the volume or the temperature is also relaxing.

Investigations on the physical properties of the system can start only after equilibrium is reached. This section details how to perform these calculations for several examples of physical properties.

1.4.2 The radial distribution function

The radial distribution function is a pair correlation of the positions of the particles present in the system. It carries an information about the structure of an ensemble of particles and thus, it is widely used in soft matter to characterise the phase of a fluid. We present here its definition from the microscopic description and the method to compute this function using Molecular Dynamics.

1.4.2.1 n-particle density

Let a group of N particles be in canonical ensemble NVT. The partition function of the microscopic configurations $\{r_1, \dots, r_N\}$ is given by:

$$Z = \int \dots \int e^{-\frac{E(r_1, \dots, r_N)}{k_B T}} d^3 r_1 \dots d^3 r_N, \quad (1.78)$$

with $E(r_1, \dots, r_N)$, the energy of the the configuration $\{r_1, \dots, r_N\}$.

Let's define the probability associated to a partial configuration where only the first n particles are taken into account:

$$P^{(n)}(r_1, \dots, r_n) = \frac{1}{Z} \int \dots \int e^{-\frac{E(r_1, \dots, r_N)}{k_B T}} d^3 r_{n+1} \dots d^3 r_N. \quad (1.79)$$

As all particles are identical, all their permutations have the same probability. There are $\binom{N}{n}$ ways of selected n particles in the system and $n!$ combinations of them to occupy the positions r_1, \dots, r_n . This allow us to compute the probability that positions r_1, \dots, r_n are occupied by any particle:

$$\rho^{(n)}(r_1, \dots, r_n) = \frac{N!}{(N-n)!} P^{(n)}(r_1, \dots, r_n). \quad (1.80)$$

This is called the n-particle density.

Using eq. 1.80 the average 1-particle density $\frac{1}{V} \int \rho^{(1)}(r) d^3r$ can be computed:

$$\begin{aligned}
\frac{1}{V} \int \rho^{(1)}(r) d^3r &= \int \frac{N!}{(N-1)!V} P^{(1)}(r) d^3r \\
&= \frac{N}{VZ} \int \left(\int \dots \int e^{-\frac{E(r_1, \dots, r_N)}{k_B T}} d^3r_2 \dots d^3r_N \right) d^3r \\
&= \frac{N}{VZ} \int \int \dots \int e^{-\frac{E(r_1, \dots, r_N)}{k_B T}} d^3r_1 d^3r_2 \dots d^3r_N \\
&= \frac{N}{V} \\
&\hat{=} \rho.
\end{aligned} \tag{1.81}$$

So the average 1-particle density is equal to the average density $\frac{N}{V}$, that is the origin of the name of this function, but it can also be interpreted as the number of particle in the position r , which is why its integral is N . Actually $\int \int \rho^{(2)}(r_1, r_2) d^3r_1 d^3r_2 = N(N-1)$, as $\rho^{(2)}$ is the pair density:

$$\rho^{(1)}(r_1) = \left\langle \sum_{i=1}^N \delta(r_i - r_1) \right\rangle_{\{r_1 \dots r_N\}}, \tag{1.82}$$

and

$$\rho^{(2)}(r_1, r_2) = \left\langle \sum_{j=1}^N \sum_{i=1, i \neq j}^N \delta(r_j - r_1) \delta(r_i - r_2) \right\rangle_{\{r_1 \dots r_N\}}. \tag{1.83}$$

Noticing that in the case of an homogeneous fluid, $\rho^{(1)}$ does not depend on the position as it is the probability to find a particle at the position r , thus:

$$\frac{1}{V} \int \rho^{(1)}(r) d^3r = \rho^{(1)} = \rho. \tag{1.84}$$

1.4.2.2 The correlation function $g^{(n)}$

By focusing on the correlation between atoms to extract $\rho^{(n)}$, one defines:

$$g^{(2)}(r_1, \dots, r_N) = \frac{\rho^{(2)}(r_1, r_2)}{\rho^{(1)}(r_1) \rho^{(1)}(r_2)}. \tag{1.85}$$

$g^{(2)}(r_1, r_2)$ is called the pair correlation function or radial distribution function. In an homogeneous and isotropic fluid, $g^{(2)}$ depends only on the distance $|r_2 - r_1|$, which allows us to write: $g^{(2)}(r_1, r_2) = \frac{\rho^{(2)}(|r_2 - r_1|)}{\rho^2} \hat{=} g(r)$.

The probability to find a particle in the position r_2 knowing there is an atom at r_1 is expressed by the conditional probability:

$$\frac{\rho^{(2)}(r_1, r_2)}{\rho^{(1)}(r_1)} = \rho^{(1)}(r_2) g^{(2)}(r_1, r_2) = \rho g(r). \tag{1.86}$$

g can also be written the same way as $\rho^{(n)}$, keeping in mind that the particles are all identical:

$$\begin{aligned} g(r) &= \frac{1}{\rho} \left\langle \sum_{j=2}^N \delta(r - |r_i - r_1|) \right\rangle_{\{r_1 \dots r_N\}} \\ &= \frac{V(N-1)}{N} \langle \delta(r - |r_1 - r_2|) \rangle_{\{r_1 \dots r_N\}} \end{aligned} \quad (1.87)$$

The pair correlation function that is here defined from the microscopic states can be measured in diffraction experiments (see Annexe C).

1.4.2.3 Computing the radial distribution function from Molecular Dynamics

Molecular Dynamics simulations allow the computation of the radial distribution function, g , by temporal average, which is equivalent to the ensemble average in ergodic conditions. g is computed as:

$$\begin{aligned} g(r) &= \frac{1}{4N\rho\pi r^2} \left\langle \sum_{i=1}^N \sum_{j=1, j \neq i}^N \delta(r - |r_i - r_j|) \right\rangle \\ &= \frac{1}{4N\rho\pi r^2} \frac{1}{T} \sum_{t=1}^T \sum_{i=1}^N \sum_{j=1, j \neq i}^N \delta(r(t) - |r_i(t) - r_j(t)|) \end{aligned} \quad (1.88)$$

$$(1.89)$$

This average formula lies in the computation of an histogram of the distances $r = |r_i(t) - r_j(t)|$ using all atoms i, j from 1 to N and all time steps from 1 to T . This histogram is then normalized by the surface of the sphere at the distance r . g is then called the pair correlation function (and sometimes radial distribution function). This calculation can be done on any system and reflects its structure. There are two possibilities to take into account the boundaries of the system here :

- without periodic boundary conditions in the calculation of the histogram, there are size effects as all atoms miss neighbours, especially the atoms close to the border of the system. For this reason, a large system is required so that the number of atoms missing neighbours is small compared to the core atoms.
- with periodic conditions, the histogram is computed by taking into account the images of the system due to the periodic boundary conditions. This method induces errors such as an atom correlated to itself.

An example of the pair correlation function of the oxygen atoms of water using TIP3P is provided in Figure 1.3 and is in good agreement with previous calculations in the literature [41].

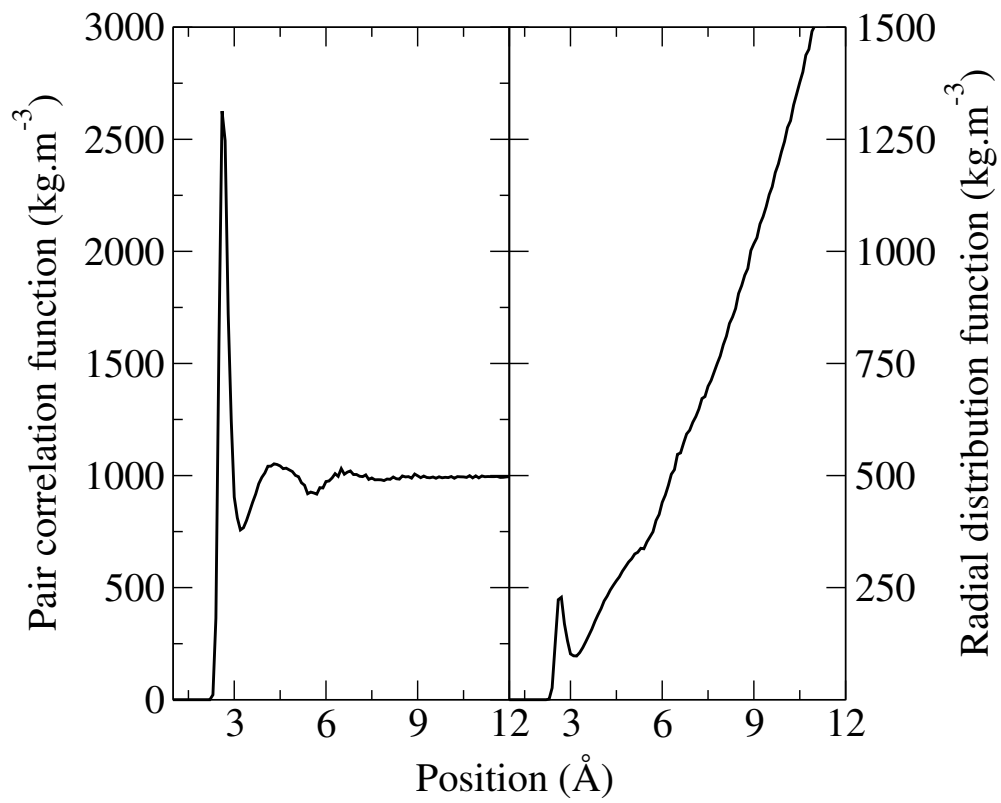


Figure 1.3: Radial distribution function and pair correlation function of oxygen atoms in water at 310 K. Both functions carries the same information but the pair correlation is normalised by the number of neighbours.

1.4.3 The dielectric properties

Most of the materials of interest in this report are dielectrics; they therefore do not contain free charges able to conduct an electrical current. However, they are made of dipoles that are still sensitive to electric fields. The susceptibility, χ , is the quantity that links the electric field, \vec{E} , to the polarisation density, \vec{p} , with ϵ_0 , the vacuum permittivity, ϵ_0 :

$$\vec{p} = \epsilon_0 \chi \vec{E}. \quad (1.90)$$

Alternatively, the polarisability, α , is the quantity linking the dipole moment $\vec{P} = \vec{p}V$, to the electric field:

$$\vec{P} = \alpha \vec{E}. \quad (1.91)$$

The polarisability is usually used to describe system at the atomic scale, and the susceptibility at the macroscopic scale, but their definitions are equivalent and one can set that $\epsilon_0 \chi = \alpha$ in any system.

The induction field \vec{D} is the electric field inside a material and it is the sum of the external field \vec{E} and the field induced by the polarisation of the local dipoles. It can be derived as follows:

$$\begin{aligned} \vec{D} &= \epsilon_0 \vec{E} + \vec{p} \\ &= \epsilon_0 \vec{E} + \epsilon_0 \chi \vec{E} \\ &= \epsilon_0 (1 + \chi) \vec{E} \\ &= \left(\epsilon_0 + \frac{\alpha}{V} \right) \vec{E} \\ &\hat{=} \epsilon_0 \epsilon \vec{E} \end{aligned} \quad (1.92)$$

$$(1.93)$$

This relation finally defines the dielectric constant of the material, ϵ .

The polarisability can be extracted from the fluctuations of the polarisation by:

$$\alpha = \beta (\langle p^2 \rangle_{x=0} - \langle p \rangle_{x=0}^2). \quad (1.94)$$

The demonstration of this relation is in Annexe D and is in fact not limited to the dielectric constant.

In general cases, the dielectric constant is frequency dependant and a complex value. This can be expressed in the frame of the linear response theory using the fluctuation-dissipation theorem.

The following paragraphs introduce this theoretical frame which the dielectric properties represent one of the possible applications. A numerical application for the polarisability is presented in Chapter 4 of this manuscript.

1.4.3.1 The linear response theory

The linear response concerns most of the phenomena and properties described in this thesis and the application of this theory provides a numerical mean to compute various quantities such as the dielectric constant.

The general expression for a linear response $X(t)$ to an external excitation $F(t)$ is [86]

$$X(t) = \int_{-\infty}^{+\infty} \chi(t, t') F(t') dt'. \quad (1.95)$$

But this can already be modified considering that χ does not depend on the absolute time and that what happens in the future ($t' > t$) does not affect the present. Thus

$$X(t) = \int_{-\infty}^t \chi(t - t') F(t') dt'. \quad (1.96)$$

This latter expression includes a convolution product, it is thus easier to use the Fourier transform of this expression:

$$X(\omega) = \chi(\omega) F(\omega). \quad (1.97)$$

Let ψ be the relaxation function. In a case of a constant excitation $F(t) = F_0$ applied from $t = -\infty$ to $t = 0$,

$$\begin{aligned} X(t) &= F_0 \int_{-\infty}^0 \chi(t - t') dt' = F_0 \int_t^{+\infty} \chi(t') dt', \\ &\hat{=} F_0 \psi(t) \end{aligned} \quad (1.98)$$

Thus

$$\chi(t) = -h(t) \frac{d\psi(t)}{dt}, \quad (1.99)$$

h is the Heaviside step function.

1.4.3.2 The Fluctuation-Dissipation theorem

The general idea of this theory is that the first order response of any system to an external excitation is linked to the fluctuation of the system at equilibrium. When the system is perturbed, knowing the equilibrium states quantities, X_i^0 , the equilibrium probability law P^0 and its evolution due to the perturbation x , it writes

$$\langle X \rangle(t) = \sum_i P_i^0 X_i^0(t) \quad (1.100)$$

Leading to

$$\langle X \rangle(t) = \langle X^0 \rangle + \beta x [\langle X^0(0) X^0(t) \rangle - \langle X^0 \rangle(t) X_0]. \quad (1.101)$$

Thus, considering that X is zero at equilibrium, and using the equation 1.98

$$\psi(t) = \beta \langle X(0) X(t) \rangle. \quad (1.102)$$

And then

$$\chi(t) = -h(t) \frac{d\langle X(0) X(t) \rangle}{dt}. \quad (1.103)$$

Thus the Fourier transform of χ is

$$\begin{aligned}\chi(\omega) &= -\beta \int_0^{+\infty} e^{i\omega t} \frac{d\langle X(0)X(t) \rangle}{dt}, \\ &= \beta \langle X(0)^2 \rangle i\omega \beta \int_0^{+\infty} e^{i\omega t} \langle X(0)X(t) \rangle dt\end{aligned}\quad (1.104)$$

Thus,

$$\begin{aligned}\chi'' &= \text{Re} \left\{ \omega \beta \int_0^{+\infty} e^{i\omega t} \langle X(0)X(t) \rangle dt, \right\} \\ &= \omega \beta \frac{1}{2} \int_{-\infty}^{+\infty} e^{i\omega t} \langle X(0)X(t) \rangle dt,\end{aligned}\quad (1.105)$$

$$(1.106)$$

This relation between the dissipation (χ'') and the fluctuations ($\langle X(0)X(t) \rangle$) is known as the fluctuation-dissipation theorem.

A weaker version of this relation can be extracted from the statistical description of the system and this is presented in Annexe D.

1.4.3.3 Applying the fluctuation-dissipation theorem in Molecular Dynamics simulations

The relation between the dissipation response and the fluctuations of a system are given by:

$$\chi'' = \frac{\beta\omega}{2} PSD(X)(\omega),$$

where

$$X(t) = \int_{-\infty}^t \chi(t-t')F(t')dt',$$

or

$$X(\omega) = \chi(\omega)F(\omega).$$

The above-mentioned relation is not a tedious task, the main difficulty being to compute the quantity X and to estimate its power spectral density (PSD). Computing X really depends on what is X and what is the system but note that the Wiener-Khintchine theorem links the power spectral density to the Fourier transform of the autocorrelation function. Defining the power spectral density:

$$PSD(X) \hat{=} \lim_{T \rightarrow \infty} \frac{|\int_0^T X(t)e^{i\omega t} dt|^2}{T},\quad (1.107)$$

the Wiener-Khintchine theorem states that:

$$PSD(X) = \int_{-\infty}^{+\infty} \langle X(0)X(t) \rangle e^{i\omega t} dt.\quad (1.108)$$

Thus the relation between the dissipation response and the fluctuations becomes:

$$\chi'' = \frac{\beta\omega}{2} PSD(X)(\omega). \quad (1.109)$$

This outcome is convenient as it avoids the computation of the autocorrelation function but there is a limitation to this theorem since it cannot be applied if the function χ is not continuous. This happens with the dielectric permittivity for instance and thus this theorem has to be used with care as it will be shown in Chapter 4.

The only problems are that this formula requires integration up to infinity and the ensemble average has to be performed. Those drawbacks are balanced by running simulations over a long enough time to reach convergence. The ensemble averaging is carried out by running several simulations of the same system to explore an increasingly larger phase space until the value converges. This method is simple and is able to provide a large amount of information but requires a large number of simulations.

1.4.4 Interface thermal resistance

The thermal conductivity (defined in Annexe E) is not relevant to describe interfacial heat transport. It is necessary to define a thermal resistance only due to the interfaces between different materials. Let R be the interface resistance, or g , the interface conductance, as the quantity linking the flux J through an interface to the temperature difference between the two sides of the interface, ΔT :

$$J = \frac{\Delta T}{R} = g\Delta T. \quad (1.110)$$

R is called the interface resistance or the Kapitza resistance. This resistance may appear as an obvious quantity but it was discovered quite recently (1941) between a copper solid and liquid helium [78], and it was found later at solid/solid interfaces [128]. This configuration actually includes any kind of interfaces, solid/liquid, solid/solid or even liquid/liquid. While being negligible for macroscopic materials, this resistance becomes increasingly important when the size of the system decreases because interfaces then become predominant. In specific structures, it can even become the main resistance.

This quantity can be investigated using Molecular Dynamics and some methods are presented here for this purpose.

1.4.4.1 ΔT method

This method allows computing the thermal resistance between two interacting systems. It was introduced and proven by Ali Rajabpour and Sebastian Volz [133]. This method is summed up here.

Let us take two systems, 1 and 2 at temperature T_1 and T_2 , interacting with each other, the heat flux exchange at their interface is:

$$J = g\Delta T, \quad (1.111)$$

with g the thermal conductance between systems 1 and 2 and $\Delta T = T_2 - T_1$. The variation of the temperature of each system of heat capacity C_1 and C_2 can be write as follows:

$$\frac{\partial T_1}{\partial t} = \frac{1}{C_1}g\Delta T(t), \quad (1.112)$$

$$\frac{\partial T_2}{\partial t} = -\frac{1}{C_2}g\Delta T(t). \quad (1.113)$$

Subtracting equation 1.113 and equation 1.112 leads to

$$\frac{\partial \Delta T}{\partial t} = -\left(\frac{1}{C_2} + \frac{1}{C_1}\right)g\Delta T(t). \quad (1.114)$$

Thus

$$\frac{\partial}{\partial t}(\Delta T(0)\Delta T(t)) = -\left(\frac{1}{C_2} + \frac{1}{C_1}\right)g\Delta T(0)\Delta T(t), \quad (1.115)$$

and by taking the ensemble average,

$$\frac{\partial}{\partial t}\langle\Delta T(0)\Delta T(t)\rangle = -\left(\frac{1}{C_2} + \frac{1}{C_1}\right)g\langle\Delta T(0)\Delta T(t)\rangle. \quad (1.116)$$

Let us defined

$$A(t) = \langle\Delta T(0)\Delta T(t)\rangle, \quad (1.117)$$

and

$$C_V = \left(\frac{1}{C_2} + \frac{1}{C_1}\right)^{-1}. \quad (1.118)$$

Therefore,

$$C_V \frac{\partial A}{\partial t} = gA. \quad (1.119)$$

The Laplace transform of this expression yields

$$C_V(s\mathcal{L}\{A\}(s) - A(t=0)) = -g\mathcal{L}\{A\}(s). \quad (1.120)$$

So at $s = 0$,

$$C_V A(t=0) = g\mathcal{L}\{A\}(s=0). \quad (1.121)$$

As a result, $R = \frac{1}{G}$ can be expressed using the definition of the Laplace transform

$$\begin{aligned} R &= \frac{1}{C_V} \frac{\mathcal{L}\{A\}(s=0)}{A(t=0)}, \\ &= \frac{1}{C_V} \frac{\int_0^\infty \langle\Delta T(0)\Delta T(t)\rangle dt}{\langle\Delta T(0)^2\rangle} \end{aligned} \quad (1.122)$$

In a classical system, $C_1 = k_B N_1$ and $C_2 = k_B N_2$, (N_1 being the number of degrees of freedom in system 1) leading to

$$R = \left(\frac{1}{k_B N_1} + \frac{1}{k_B N_2} \right) \frac{\int_0^\infty \langle \Delta T(0) \Delta T(t) \rangle dt}{\langle \Delta T(0)^2 \rangle}. \quad (1.123)$$

This is a method to compute the resistance at the interface between two systems. This interface is defined energetically as the limit between two ensembles of particles. This can be different from a geometrically defined interface as the particles could be mixed or the surface contact between the systems could unclear. An example of application of this method is given in Chapter 2.

1.4.4.2 Extension of the ΔT method to three systems

The ΔT method is a convenient method to compute interface resistance but it is limited to two systems interacting with each other only. An extension of this method to 3 systems interacting with each other is proposed here.

Let be 3 systems with the temperatures T_1, T_2, T_3 and their heat capacity C_1, C_2 and C_3 . Each system is in thermal contact with the two others. Naming g_{XY} the thermal conductance between the systems X and Y and $\Delta T_{XY} = T_Y - T_X$, leads to

$$C_1 \frac{\partial T_1}{\partial t} = g_{12} \Delta T_{12} + G_{13} \Delta T_{13}, \quad (1.124)$$

$$C_2 \frac{\partial T_2}{\partial t} = -g_{12} \Delta T_{12} + G_{23} \Delta T_{23}, \quad (1.125)$$

$$C_3 \frac{\partial T_3}{\partial t} = -g_{13} \Delta T_{13} - G_{23} \Delta T_{23}. \quad (1.126)$$

$$(1.127)$$

Those equations can be rewritten as:

$$\frac{\partial T(t)}{\partial t} = g \Delta T(t), \quad (1.128)$$

meaning that:

$$\frac{\partial}{\partial t} \begin{bmatrix} T_1 \\ T_2 \\ T_3 \end{bmatrix} = \begin{bmatrix} \frac{g_{12}}{C_1} & 0 & \frac{g_{13}}{C_1} \\ -\frac{g_{12}}{C_2} & \frac{g_{23}}{C_2} & 0 \\ 0 & -\frac{g_{23}}{C_3} & -\frac{g_{13}}{C_3} \end{bmatrix} \begin{bmatrix} \Delta T_{12} \\ \Delta T_{23} \\ \Delta T_{13} \end{bmatrix} \quad (1.129)$$

This latter equation can be multiplied by $M(0) = \begin{bmatrix} \Delta T_{12}(t=0) & 0 & 0 \\ 0 & \Delta T_{23}(t=0) & 0 \\ 0 & 0 & \Delta T_{13}(t=0) \end{bmatrix}$

and take the phase average of the resulting equation:

$$\frac{\partial}{\partial t} \langle T(t) M(0) \rangle = g \langle \Delta T(t) M(0) \rangle. \quad (1.130)$$

If $C_{XY}(t)$ refers to the vector $\langle X(t)Y(0) \rangle$ (X is a vector and Y a matrix):

$$\frac{\partial}{\partial t} C_{TM}(t) = g C_{\Delta TM}(t). \quad (1.131)$$

The Laplace transform leads to:

$$s\mathcal{L}\{C_{TM}\}(s) - C_{TM}(t=0) = g\mathcal{L}\{C_{\Delta TM}\}(s), \quad (1.132)$$

setting s to zero:

$$g C_{\Delta TM}(t=0) = -\mathcal{L}\{C_{TM}\}(s=0). \quad (1.133)$$

This latter relation can be solved for g as only three different components appear (heat capacities are known in classical systems).

Our derivation cannot be generalized to N systems interacting with $N-1$ other bodies. That means there are $\frac{N(N-1)}{2}$ different components in g and N independent equations which can be solved for $N \leq 3$ only.

However, if each system only interact with 2 others, G contains N different components, and equation 1.133 can be solved for any value of N .

1.4.4.3 Application of the ΔT method in Molecular Dynamics

The ΔT method allows one to compute an interface resistance with the relation:

$$R = \left(\frac{1}{k_B N_1} + \frac{1}{k_B N_2} \right) \frac{\int_0^\infty \langle \Delta T(0) \Delta T(t) \rangle dt}{\langle \Delta T(0)^2 \rangle}. \quad (1.134)$$

In Molecular Dynamics simulations, none of the quantities appearing in this equation are difficult to compute but the difficulty is the same as the one seen in the Green-Kubo method. The autocorrelation function must converge and one has to average a large number of simulations to achieve a reasonable accuracy. The original publication of the method provides an example of application [133]. In the end, this method is alike the Green-Kubo method except that the quantities involved are easier to compute and one especially does not have to compute the heat flux.

1.4.4.4 Non-Equilibrium Molecular Dynamics

The method described above is an equilibrium method, which means that the system has identified equilibrium temperature, pressure, energy, etc... However, non-equilibrium numerical experiments can also be performed. To compute the response of the system to an external excitation, instead of using statistical physics, the excitation is applied and the system response is monitored.

For example, a heat flux can be applied on the system to compute the thermal conductivity. This operation can be achieved by adding energy to the atoms in one region of the system and removing the same energy in another one of the

system. When the stationary state is reached, the Fourier's Law is simply used to compute the conductivity as the heat flux F and the temperature gradient can be estimated during the simulation. Their ratio indeed yields the thermal conductivity:

$$\lambda = \frac{-F}{\|\text{grad } T\|}. \quad (1.135)$$

In the case of a system including an interface, the temperature drops ΔT can be identified at the interfaces and compute the corresponding conductance G as:

$$G = \frac{F}{\Delta T}. \quad (1.136)$$

The application of the method is straightforward, especially on liquids and systems with short mean free paths.

This method can be used to compute any response function such as viscosity, permeability, susceptibility and so on. As the system is out of equilibrium, only the parameter resulting from the constraint can be computed. The constraint might also make it difficult to understand or interpret the result. For instance, when a heat flux is applied in MD, the temperature difference can be large making difficult the estimation of the temperature at which thermal conductivity is measured.

Because they are direct, easy to implement and require less theoretical background, those non-equilibrium methods are often used and serve as validations for more advance theories.

1.4.5 Viscosity

The present work mostly targets soft materials, which crucial property is the viscosity quantifying the resistance of the fluid to deformation. This quantity will be at the centre of the work presented in the last chapters of this manuscript. One way to define the viscosity is to consider two slices separated by the distance dz as illustrated in Figure 1.4. One slice is moving at the velocity $v + dv$ in a direction parallel to the plane of the slices. Its movement induces a force F on the other slice moving at the velocity v due to the viscosity μ and the contact surface S .

$$F = S\mu \frac{dv}{dz}. \quad (1.137)$$

The Green-Kubo formula, presented in Annexe E.1, is not limited to the thermal conductivity and can be used to compute the viscosity:

$$\mu = \frac{V}{k_B T} \int_0^\infty \langle P_{xz}(0)P_{xz}(t) \rangle dt, \quad (1.138)$$

corresponding to a case where the velocity of the fluid is along the x axis and the gradient along the z axis, with P referring to the pressure tensor. This relation is known as the Green-Kubo relation for viscosity.

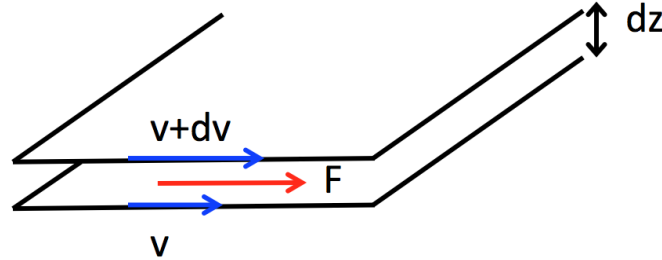


Figure 1.4: Definition of the viscosity with the speed gradient in a fluid. The viscosity is defined as a proportionality coefficient between the force F applied by one part of fluid on another and the velocity gradient in the fluid $\frac{dv}{dz}$.

1.4.6 Phase transition

Most materials exist under different phases. This is the case of water of course, that can exist as solid (ice) liquid or gas (vapour). This is also the case of lipid bilayers, gold, polymer materials, etc ... However, the phase change might be different than liquid-gas or solid-liquid transitions. The phase transition is a way for the system to relax and release energy. In general, phase transitions are classified into two categories [70]:

- first order phase transitions which involve a latent heat. During the phase change, the system either absorbs or releases a certain amount of energy. The melting of water is an example of first order phase transition.
- second order phase transition which is a continuous phase transition; It is characterized by a divergent susceptibility as in ferromagnetic materials.

The Gibbs free energy G is used to quantify these transitions:

$$G \hat{=} E + PV - TS = H - TS, \quad (1.139)$$

where E is the internal energy, P , the pressure, V , the volume, H , the enthalpy, T , the temperature and S is the entropy. When the first derivative of the Gibbs free energy is discontinuous, it is a first order phase transition. During second order phase transitions, the second derivative of G is continuous. This work mostly tackles first order transitions. Let us recall here that during a first order phase transition, the heat capacity C_P diverges and it will usually be the signal to measure the phase transition. The heat capacity is indeed defined by:

$$\frac{\partial H}{\partial T} = C_P. \quad (1.140)$$

At the phase transition (first order):

$$\Delta H = L, \quad (1.141)$$

where L is the latent heat. This discontinuity of the enthalpy leads to the divergence of the heat capacity. A way to highlight the physical origin of

this latent heat is to consider for instance a solid. When a system is heated toward its melting point, the heat added will stop being used for increasing the temperature but will instead break the bonds inside the solid. The system stays at the same temperature as long as it has not completely melted.

An order parameter is used to characterize the phase transition. It is typically zero in one phase and non-zero in the other phase. The density can be the order parameter for the liquid-gas phase transition or the magnetization for the ferromagnetic-paramagnetic transition.

Let us notice that there is some cases where the system is under conditions of pressure and temperature in which it should be in another phase and still does not undergo a phase transition. An example is the well-known surfusion of water. Water can stay liquid under 0°C in a metastable state. A perturbation is needed to initiate the phase transition.

In the following chapters, the phase transition of lipid bilayers will be investigated and discussed. However, this will be done only using experiments and not simulations but investigations of a phase transition using Molecular Dynamics are possible. This is why numerical methods for simulating phase change are presented here.

1.4.6.1 Phase transition in Molecular Dynamics

Molecular Dynamics can also be used to simulate the phase transition of materials. In principle, this can be achieved either by increasing a parameter that will make the system go through a phase transition during the simulation or by implementing several simulations with this parameter set at different values. In both cases, the order parameter is defined to characterise the transition and measure, for example, the transition temperature.

In practice, studying the phase transition is difficult because it requires having an interaction model that can simulate the system in different phases. Then, the time scale of the Molecular Dynamics simulations is short and the phase space observe is rather small in such a way that the system can often reach a metastable state.

As an example, the phase transition of water can be studied by using the TIP3P model. The transition of water from a liquid to a gas are analysed when the temperature increases. In this aim, 4000 water molecules using the TIP3P model described above, at 310K and with a 0.1 fs timestep. First 500 steps are run in NVE, then 20000 steps in NVT, and 50000 steps in NPT. Finally 300000 time steps in NPT are simulated with a pressure P set to 1 atm but with T increasing from 310 K to 700 K. The order parameter chosen here is the density, which is about $1\text{ g}\cdot\text{cm}^{-3}$ and almost zero in the gas phase.

Figure 1.5 shows the evolution of the density as a function of the temperature. This graph shows that water (black line) vaporises at about 670K, which is a high temperature but here, only one simulation is used and the temperature is increased from 310 K to 700 K in 30 ps. This ramp is too steep and a

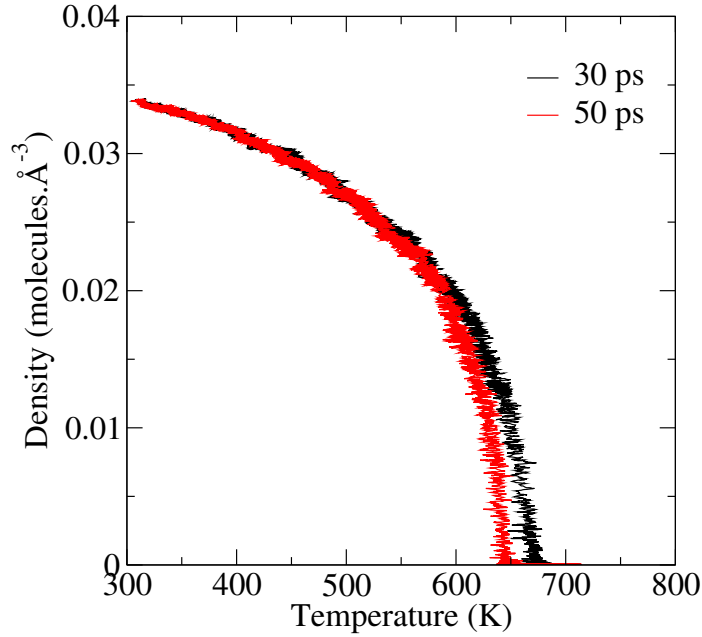


Figure 1.5: Density of water as function of the temperature computed during heating simulations of 30 ps and 50 ps from 310 K to 700 K. This fast heating does not allow the phase transition to occur at its expected temperature and when the heating is slower the transition temperature becomes smaller.

metastable state was generated. The system is still liquid at high temperatures and is vaporised later. If the same simulation is made but with 50 ps to reach the same final temperature of 700 K, the results reported in the red curves on Figure 1.5 are obtained. In this situation, the transition temperature is 650 K. This shows that it can be difficult to achieve a phase transition in a controlled manner. Thus, when the aim is to compute a precise transition temperature, it is preferable to run different simulations equilibrated at different temperatures but in this case the transition itself is not simulated.

1.4.7 Density of vibrational states

The density of vibrational states is defined as the number of modes per frequency interval, $N(\omega)$ [33] and thus maps the frequencies present in a system. It can be expressed from the autocorrelation function of the atomic velocities:

$$\begin{aligned}
 N(\omega) &\hat{=} \sum_{j=1}^{3N} \delta(\omega - \omega_j) \\
 &= \frac{1}{3k_B T} \int_0^\infty \sum_{n=1..N} m_n \langle \vec{v}_n(0) \cdot \vec{v}_n(t) \rangle e^{i\omega t} \quad (1.142)
 \end{aligned}$$

where N is the number of atoms, $\vec{v}_n(t)$ is the velocity of atom n at instant t , m_n , its mass, k_B is the Boltzmann constant and T the temperature.

We propose to demonstrate relation 1.142. Let us consider a system that is an ensemble of point masses coupled via spring forces. The motion equation of a given atom n projected in a given direction $d = x, y$ or z :

$$m_n \ddot{u}_{nd} = - \sum_{k=1}^N \sum_{l=x,y,z} c^{nd,kl} u_{kl}, \quad (1.143)$$

or

$$\sqrt{m_n} \ddot{u}_{nd} = - \sum_{k=1}^N \sum_{l=x,y,z} \frac{c^{nd,kl}}{\sqrt{m_n \cdot m_k}} \sqrt{m_k} u_{kl}, \quad (1.144)$$

When looking for the solutions such as $\vec{u}_n(t) = \vec{u}_n^0 e^{i\omega t}$, the motion equation takes the new form:

$$\omega^2 \sqrt{m_n} u_{nd}^0 = - \sum_{k=1}^N \sum_{l=x,y,z} \frac{c^{nd,kl}}{\sqrt{m_n \cdot m_k}} \sqrt{m_k} u_{kl}^0, \quad (1.145)$$

We rewrite the equations as a matrix equation:

$$\omega^2 U = CU, \quad (1.146)$$

where $U_{3(n-1)+d} = \sqrt{m_n} u_{nd}^0$ (a $3N$ long vector) and $C_{nd,kl} = \frac{c^{nd,kl}}{\sqrt{m_n \cdot m_k}}$ which is a symmetrical matrix.

Let us now consider the $3N$ normalized eigenvectors, U^j , and ω_j , the square root of its corresponding eigenvalues. Accordingly the vectors U^j are orthonormal:

$$U^j \cdot U^k = \sum_{n=1}^N \sum_{d=x,y,z} m_n u_{nd}^{0j} u_{nd}^{0k} = \delta(j-k). \quad (1.147)$$

So the position vector X can be written as:

$$X = \sum_{j=1}^{3N} A_j U^j, \quad (1.148)$$

and for atom n :

$$\sqrt{m_n} \vec{r}_n(t) = \sum_{j=1}^{3N} A_j \sqrt{m_n} \vec{u}_n^{0j} e^{-i\omega_j t}. \quad (1.149)$$

Thus

$$\sqrt{m_n} \dot{\vec{r}}_n(t) = \sqrt{m_n} \vec{v}_n(t) = \sum_{j=1}^{3N} -i\omega_j A_j \sqrt{m_n} \vec{u}_n^{0j} e^{-i\omega_j t}. \quad (1.150)$$

The sum over the atoms and the direction of the velocity autocorrelation functions:

$$\sum_{n=1}^N m_n \langle \vec{v}_n(0) \cdot \vec{v}_n(t) \rangle = \left\langle \sum_{n=1}^N \omega_j^2 \sum_{k=1}^N \sum_{j=1}^N A_j A_k m_n \vec{u}_n^{0k} \cdot \vec{u}_n^{0j} e^{-i\omega_j t} \right\rangle, \quad (1.151)$$

However,

$$U^k \cdot U^j = \delta(k - j). \quad (1.152)$$

Therefore,

$$\sum_{n=1}^N m_n \vec{u}_n^{0k} \cdot \vec{u}_n^{0j} = \delta(k - j). \quad (1.153)$$

Combining Eq.1.153 and Eq.1.151,

$$\begin{aligned} \sum_{n=1}^N m_n \langle \vec{v}_n(0) \cdot \vec{v}_n(t) \rangle &= \left\langle \sum_{n=1}^N \sum_{k=1}^{3N} \sum_{j=1}^{3N} \omega_j^2 A_j A_k m_n \vec{u}_n^{0k} \cdot \vec{u}_n^{0j} e^{-i\omega_j t} \right\rangle, \\ &= \sum_{k=1}^{3N} \sum_{j=1}^{3N} \omega_j^2 \langle A_j A_k e^{-i\omega_j t} \sum_{n=1}^N m_n \vec{u}_n^{0k} \cdot \vec{u}_n^{0j} \rangle, \\ &= \sum_{k=1}^{3N} \sum_{j=1}^{3N} \omega_j^2 \langle A_j A_k e^{-i\omega_j t} \delta(k - j) \rangle, \\ &= \sum_{j=1}^{3N} \omega_j^2 \langle A_j^2 \rangle e^{-i\omega_j t}, \end{aligned} \quad (1.154)$$

The average kinetic energy of each mode j , K_j , can be computed as the kinetic energy of the system when all other modes are frozen (the modes are uncoupled):

$$\langle K_j \rangle = \sum_{n=1}^N \frac{1}{2} m_n \langle v_n^j{}^2 \rangle, \quad (1.155)$$

and thanks to equation 1.150

$$\langle K_j \rangle = \frac{1}{2} \omega_j^2 \langle A_j^2 \sum_{n=1}^N m_n \vec{u}_n^{0j} \cdot \vec{u}_n^{0j} \rangle. \quad (1.156)$$

Using the equipartition theorem, each mode, with its 3 components, carries a total energy of $3k_B T$, giving for the kinetic energy of mode j :

$$\langle K_j \rangle = \frac{1}{2} \omega_j^2 \langle A_j^2 \rangle = \frac{3}{2} k_B T. \quad (1.157)$$

Then in equation 1.154,

$$\sum_{n=1}^N m_n \langle \vec{v}_n(0) \cdot \vec{v}_n(t) \rangle = 3k_B T \sum_{j=1}^N e^{-i\omega_j t}. \quad (1.158)$$

Finally, by taking the Fourier transform of this relation,

$$\begin{aligned} \int_0^\infty \sum_{n=1}^N m_n \langle \vec{v}_n(0) \cdot \vec{v}_n(t) \rangle e^{i\omega t} dt &= 3k_B T \int_0^\infty \sum_{j=1}^{3N} e^{-i(\omega_j - \omega)t} dt \\ &= 3k_B T \sum_{j=1}^{3N} \delta(\omega - \omega_j). \end{aligned} \quad (1.159)$$

Which directly leads to equation 1.142. This relation is demonstrated in a system with harmonic bonds, which is not the case in most systems but it will still be applied on any system, solids or liquids.

In Molecular Dynamics, the density of vibrational states can be computed from the velocities of the atoms. Several examples of applications will be presented in chapters 2 and 4.

1.5 Conclusion

In this chapter, the phenomenological definitions of the thermal resistance, the polarizability and the viscosity have been recalled and the theoretical background of phase transition phenomena has been introduced. Statistical physics has been used to define these quantities and behaviour from a microscopic description. However, the concept of phonon has not been introduced here while it is central in heat transfer. This is because the work presented in this thesis focuses on soft matter materials where phonons cannot be properly defined due to the absence of translational invariance. Only the concept of vibrational relaxation stands in what follows. The statistical descriptions of the phenomena presented here can be applied in analytical models but in the cases of interest in this thesis, it is required to use a numerical tool to simulate the ensembles of particles on which the equations of statistical physics will be applied.

Thus, Molecular Dynamics is introduced as a practical tool to simulate an ensemble of particles and apply statistical physics methods to investigate condensed matter transport and structural properties. The characteristics of this method lead to both advantages and limitations:

- it is classical: the equipartition theorem is valid and the statistical physics equations are thus simplified but quantum effects cannot be modelled.
- the interaction model relies on empirical interaction potentials: it is simple to implement but the interaction model depends on the property used to fit the potential.
- it simulates the time evolution of the system: the spectral information is accessible but the integration time required to simulate a few nanoseconds can reach tens of hours.

These characteristics make Molecular Dynamics simulations a perfect tool to simulate nanoscale systems such as the one studied in the following chapters.

Part II

Solid/liquid interface

Chapter 2

Heat transfer at a solid/liquid interface

2.1	Introduction	50
2.2	Modelling	51
2.2.1	Potentials	51
2.2.2	Details of the systems studied and the simulations .	52
2.3	Effect of the curvature on the gold/water interface	54
2.4	Interface Resistance calculation	55
2.4.1	Thermal resistance of the bare gold/water interface .	55
2.4.2	Effect of polymer grafting on the thermal resistance	56
2.5	Physical analysis of the interfaces	58
2.6	Qualitative analysis by a transient non-equilibrium method	61
2.7	Generalization of the results	62
2.8	Conclusion	65

2.1 Introduction

Metallic nanoparticles are used in several studies ranging from physics to biology due to their optical and morphological properties [148, 38, 39, 6, 139]. Applications can be mentioned in molecular imaging [24] and Raman spectroscopy [112, 71]. More recently, metallic nanoparticles have attracted an even greater interest due to their ability to absorb radiations and to turn them into heat through plasmon resonance [123, 54, 125, 96, 72, 16, 83, 95, 153]. This feature makes nanoparticles promising candidates for the development of drug delivery systems [96, 29] and photo-induced hyperthermia to destroy tumor cells [177, 158]. In this context a precise control of the local heat release into the environment is sought. Measurements of the heat at the vicinity of nanoparticle is a difficult problem that has been addressed by experiments where thermosensitive polymers are attached to the surface of the nanoparticles allowing the measure of the temperature field [139, 99, 140, 129, 46]. Some physical models have been proposed [54, 8, 56, 113, 140, 175, 68] to describe this temperature field at the interface between a gold nanoparticle and water and only a few microscopic models [113] but, while bare nanoparticles are rare in applications, the effect of the polymer covering has not been addressed. We seek to tackle this problem as it has great potential for the engineering of nanosystems for biological applications. The thermal resistance of a gold/water interface is studied and how it is affected when a polymer is grafted on it. To answer this question, a Molecular Dynamics model of the interface between a gold nanoparticle and water has been developed.

The first step of this study is the development of the Molecular Dynamics model. As mentioned here, our solid/liquid interface is a gold/water interface. It has been chosen to model a DHLA-Jeffamine for the grafted polymer. This is a thermosensitive polymer, just like PNIPAAm [29], and its lower critical solution temperature (LCST) can be tuned by its length. Furthermore, this polymer can make thiol bonds with the gold atoms of the solid. The process of experimentally grafting this polymer using this bond is also well handled [37]. These properties make DHLA-Jeffamine a good candidate to design self-assembled nanoparticles for photo-induced hyperthermia [37].

This first part of this chapter describes how the Molecular Dynamics model is implemented with these different subsystems and specifically how the potentials to make the different elements of the system interact together have been chosen. In a second part, it is shown that modelling only a plane of water to address the problem of the heat transfer at the gold/water interface and that it will still be a relevant model for nanoparticles of sizes above at least 14 nm of diameter. This is done by comparing the structure of water at the interface with gold of different radii of curvature.

Then, we detail our numerical calculations and results using the ΔT method to compute the thermal conductance of the gold/water interface and how the grafted polymer increases this conductance. We present our interpretation of

this result by computing the transmission function at the gold/polymer interface and the density of states of each element of our model.

2.2 Modelling

We present here the modelling procedure of our gold/water/polymer system. These three subsystems will be modelled with three different potentials and we will first describe these potentials and how they interact with the each other. Then we describe the five different geometries we have investigated. Three of them are nanoparticles of different radii of curvature to study its influence on the water structure and two of them are planar gold surfaces with water, one of those surfaces has a polymer grafted on it.

2.2.1 Potentials

We model systems made of gold, water and a DHLA-Jeffamine polymer. The skeletal formula of this polymer is given on Figure 2.1. We chose to use the TIP3P model for the water (the flexible version) [75, 27, 41], the DREIDING model for the polymer [110] and the MEAM potential for the gold [11]. These potentials are presented in Chapter 1. However, here we have to combine those potentials. Between the atoms modelled by DREIDING and TIP3P, we use the DREIDING model. This is not difficult as those two models involve the same potentials only with a different set of parameters. It is more complicated between the water and the gold but gold/water systems have already been modelled in Molecular Dynamics and so potentials have already been developed and tested [113, 147]. It is a Lennard-Jones potential:

$$E = 4\epsilon \left[\left(\frac{\sigma}{r} \right)^{12} - \left(\frac{\sigma}{r} \right)^6 \right],$$

with

- $\epsilon = 0.25584406$ kcal.mol⁻¹ et $\sigma = 3.6$ Å for the interaction between oxygen and gold atoms.
- $\epsilon = 0.0$ et $\sigma = 0.0$ Å for the interaction between hydrogen and gold atoms.

About the interactions between the gold and the polymer atoms, there is a thiol bond between the gold and the sulfur atoms for which the parameters can be found in the literature [76] for a harmonic bond:

$$E = K(r - r_0)^2,$$

with $r_0 = 2.531$ Å and $K = 8.586$ kcal.mol⁻¹.Å² but we can use the equivalent Morse potential instead:

$$E = D_0 \left[e^{-2\alpha(r-r_0)} - 2e^{-\alpha(r-r_0)} \right],$$

with $D_0 = 0.856$ kcal.mol⁻¹, $\alpha = 3.16227766$ Å⁻¹ et $r_0 = 2.531$ Å.

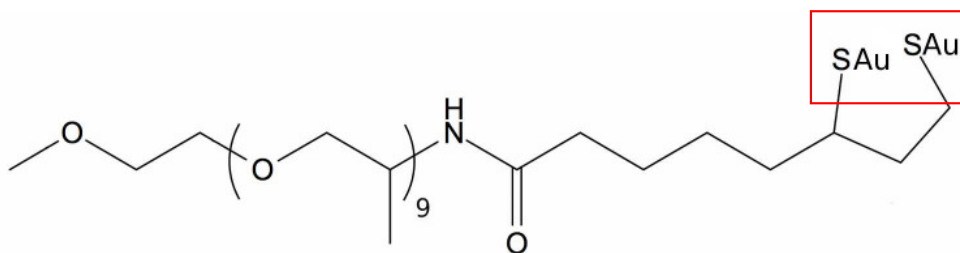


Figure 2.1: Skeletal formula of DHLA-Jeffamine polymer. This polymer ends with sulfur atoms that are bonded to Au atoms of the gold surface by a thiol bond.

To model the long range interaction (van der Waals) between the polymer and the gold, we used the Lennard-Jones potential and the method proposed in the DREIDING model to compute the parameters ϵ and σ (Chapter 1). For the gold, we used the parameters from the Universal Force Field [135] giving $R_0(\text{Au}) = 2.934 \text{ \AA}$ and $D_0(\text{Au}) = 0.039 \text{ kcal.mol}^{-1}$.

The last part is the computation of the local charges of the atoms of the DHLA-Jeffamine polymer which is done using the Gasteiger algorithm [49] as seen in Chapter 1. We indicates those charges in Table 2.1.

2.2.2 Details of the systems studied and the simulations

In this chapter, we will study 5 different systems:

- 3 nanoparticles of respectively 6.5 nm, 17 nm and 28 nm of diameter to study the effect on the curvature of these particles on the structure of the water at the interface.

To reduce the computational costs, we exploit the symmetries of nanoparticles and we model only an 8th of the particles. To build them, we create a cubic gold crystal which the edge is half the diameter of the nanoparticle, then we delete all atoms outside of the largest inscribing $\frac{1}{8}$ th of sphere within the gold cube. We then add 50 \AA of water molecules around the nanoparticle to complete the system. We don't use periodical conditions in these systems, we thus used reflective walls as described in Chapter 1.

- a planar gold surface in contact with water.

To build this system, we use the same method as for the nanoparticles but we keep the cubic gold crystal (about 125 nm^3) and add 5 nm of water above. Here we used periodical conditions in the directions parallel to the gold/water interface plane. The area of the contact between the gold and the water is 28 nm^2 .

- a gold surface with a DHLA-Polymer grafted on it, in contact with water. To build this system, we use the previous system and added the polymer on the gold surface using, at first, an harmonic potential for the Au-S bond. The charges computed with the Gasteiger algorithm are given in

Table 2.1: Atoms of the DHLA-Jeffamine polymer with their partial charges computed with the Gasteiger algorithm [49] and the atoms they are bonded to.

ID	Type	Partial charge	Bonded to				ID	Type	Partial charge	Bonded to			
			1	2	3	4				1	2	3	4
1	H	0.085516632	2				59	H	0.085866632	57			
2	C	-0.218687368	1	3	4	5	60	H	0.085866632	57			
3	H	0.085516632	2				61	H	0.085866632	57			
4	H	0.085516632	2				62	O	-0.028597368	56	63		
5	O	-0.052519368	2	6			63	C	-0.170242368	62	64	65	66
6	C	-0.182448368	5	7	8	9	64	H	0.103807632	63			
7	H	0.102002632	6				65	H	0.103807632	63			
8	H	0.102002632	6				66	C	-0.155060368	63	67	68	72
9	C	-0.180900368	6	10	11	12	67	C	-0.224421368	66	69	70	71
10	H	0.102092632	9				68	H	0.121653632	66			
11	H	0.102092632	9				69	H	0.085866632	67			
12	O	-0.039567368	9	13			70	H	0.085866632	67			
13	C	-0.171776368	12	14	15	16	71	H	0.085866632	67			
14	H	0.103715632	13				72	O	-0.028597368	66	73		
15	H	0.103715632	13				73	C	-0.170242368	72	74	75	76
16	C	-0.155119368	13	17	18	22	74	H	0.103807632	73			
17	C	-0.224422368	16	19	20	21	75	H	0.103807632	73			
18	H	0.121652632	16				76	C	-0.155063368	73	77	78	82
19	H	0.085866632	17				77	C	-0.224421368	76	79	80	81
20	H	0.085866632	17				78	H	0.121653632	76			
21	H	0.085866632	17				79	H	0.085866632	77			
22	O	-0.028598368	16	23			80	H	0.085866632	77			
23	C	-0.170242368	22	24	25	26	81	H	0.085866632	77			
24	H	0.103807632	23				82	O	-0.028666368	76	83		
25	H	0.103807632	23				83	C	-0.171608368	82	84	85	86
26	C	-0.155060368	23	27	28	32	84	H	0.103699632	83			
27	C	-0.224421368	26	29	30	31	85	H	0.103699632	83			
28	H	0.121653632	26				86	C	-0.168484368	83	87	88	92
29	H	0.085866632	27				87	C	-0.225854368	86	89	90	91
30	H	0.085866632	27				88	H	0.119221632	86			
31	H	0.085866632	27				89	H	0.085792632	87			
32	O	-0.028597368	26	33			90	H	0.085792632	87			
33	C	-0.170242368	32	34	35	36	91	H	0.085792632	87			
34	H	0.103807632	33				92	N	-0.074401368	86	93	94	
35	H	0.103807632	33				93	H	0.102721632	92			
36	C	-0.155060368	33	37	38	42	94	C	-0.057589368	92	95	96	
37	C	-0.224421368	36	39	40	41	95	O	0.025455632	94			
38	H	0.121653632	36				96	C	-0.182861368	94	97	98	99
39	H	0.085866632	37				97	H	0.101644632	96			
40	H	0.085866632	37				98	H	0.101644632	96			
41	H	0.085866632	37				99	C	-0.198523368	96	100	101	102
42	O	-0.028597368	36	43			100	H	0.100813632	99			
43	C	-0.170242368	42	44	45	46	101	H	0.100813632	99			
44	H	0.103807632	43				102	C	-0.199291368	99	103	104	105
45	H	0.103807632	43				103	H	0.100871632	102			
46	C	-0.155060368	43	47	48	52	104	H	0.100871632	102			
47	C	-0.224421368	46	49	50	51	105	C	-0.198619368	102	106	107	108
48	H	0.121653632	46				106	H	0.100776632	105			
49	H	0.085866632	47				107	H	0.100776632	105			
50	H	0.085866632	47				108	C	-0.180728368	105	109	110	112
51	H	0.085866632	47				109	H	0.101361632	108			
52	O	-0.028597368	46	53			110	S	-0.018744368	108			
53	C	-0.170242368	52	54	55	56	111	C	-0.198036368	108	112	113	114
54	H	0.103807632	53				112	H	0.100670632	111			
55	H	0.103807632	53				113	H	0.100670632	111			
56	C	-0.155060368	53	57	58	62	114	C	-0.180885368	111	115	116	117
57	C	-0.224421368	56	59	60	61	115	H	0.101346632	114			
58	H	0.121653632	56				116	H	0.101346632	114			
							117	S	-0.018754368	114			

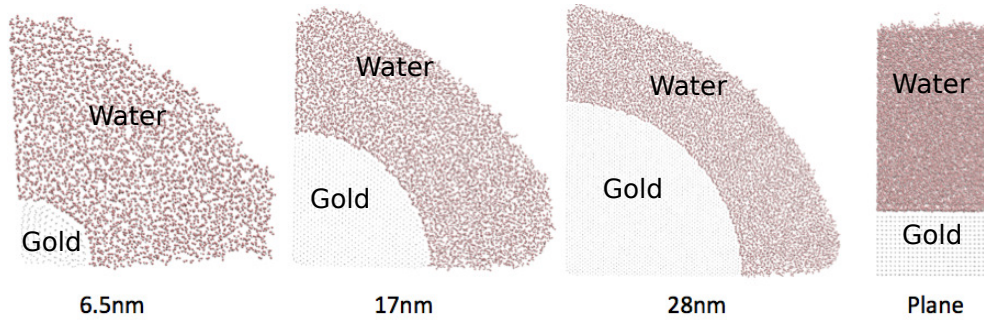


Figure 2.2: Gold/water interfaces with different radius curvature of the gold surface. The first three systems are 8th of a nanoparticle of the indicated diameter. We only represent slices of the whole system here. The fourth system is a planar surface (with periodic boundary conditions in the directions parallel to the gold plane). All those system are simulated at 310 K.

Table 2.1.

After a first simulation to equilibrate this structure, we change this bond into a Morse potential and then add water on the structure avoiding the polymer by 3 Å.

Due to the full atomistic model, where hydrogen atoms are represented, we need a time step always under 1 fs in the simulations. We used a 0.5 fs time step during the equilibration run under canonical ensemble. We used a 0.1 fs time step in microcanonical runs. To ensure reaching the equilibrium of temperature of 310 K and pressure of 1 atm in the canonical ensemble, we ran the system for 800 ps. Only after this equilibrium is reached, we switch to the microcanonical ensemble simulation and all the results we present are produced we data collected during this stage.

2.3 Effect of the curvature on the gold/water interface

We use our four first systems to study the effect of the radius of curvature of the gold surface on the structure of the water. Those different systems are presented on the Figure 2.2 (we represent only slices for the nanoparticles). The larger the radius of curvature, the closer the gold/water interface will be to the plane model. The simulations allow us to characterise this convergence in terms of water density profile.

We have calculated the density profiles of the water surrounding the gold to characterise those interfaces and the results are presented on Figure 2.3. We see that the water density is maximum a few ångströms away from the gold surface and is structured up to 1 nm from it. This is true near the plane of gold and the nanoparticles of at least 17 nm of diameter. Around our smallest nanoparticle, 6.5 nm of diameter, there is no structure in the water and no density pick. A

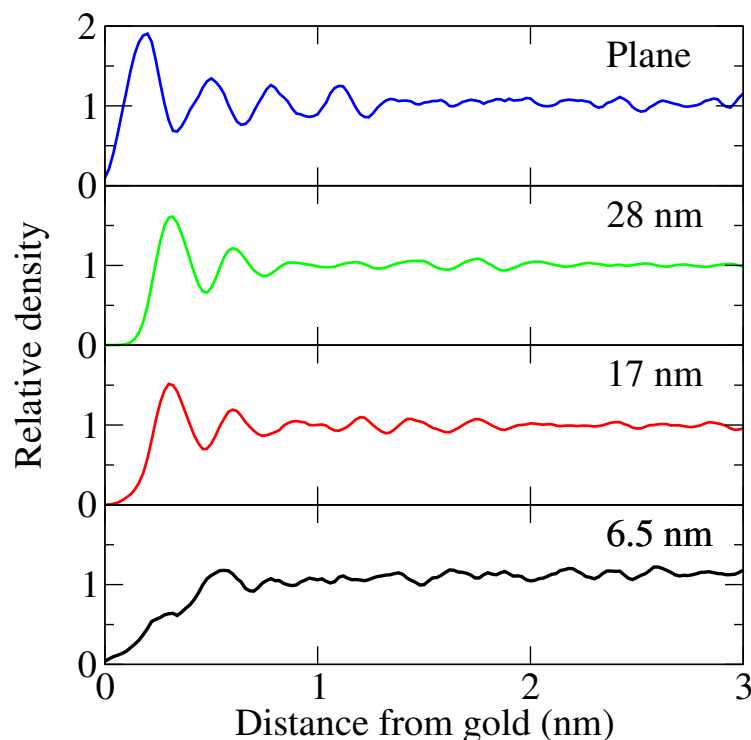


Figure 2.3: *Density profiles of water at the interface with gold at 310 K for our different gold geometries. This shows that the density profile of water is very perturbed by the 6.5 diameter nanoparticle but with nanoparticle of 17 nm of diameter and more, the density profile of the water on a planar surface is recovered.*

closer view of this interface showing the details of this nanoparticle, presented on Figure 2.4, show that the gold itself in this nanoparticle is unstructured. This let us think that the interaction force with the gold structures the water and that this one imitates the crystal structure of the gold.

With the nanoparticle of 17 nm of diameter, Figure 2.3 shows that the gold/water interface can be correctly approached by a planar surface. Thus the rest of our studies and therefore the rest of this chapter will be on a planar surface.

2.4 Interface Resistance calculation

2.4.1 Thermal resistance of the bare gold/water interface

On the plane system from Figure 2.2, we calculate the thermal resistance of the gold/water interface R_{GW} . To achieve this we used an equilibrium method based on the fluctuations of the temperature difference between the gold and the water, detailed in Chapter 1 as the ΔT method [133]. We compute the autocorrelation of $T_{or}-T_{eau}$ and average the results over ten simulations for ensemble average. Its integral gives the resistance of our 28 nm^2 gold/water

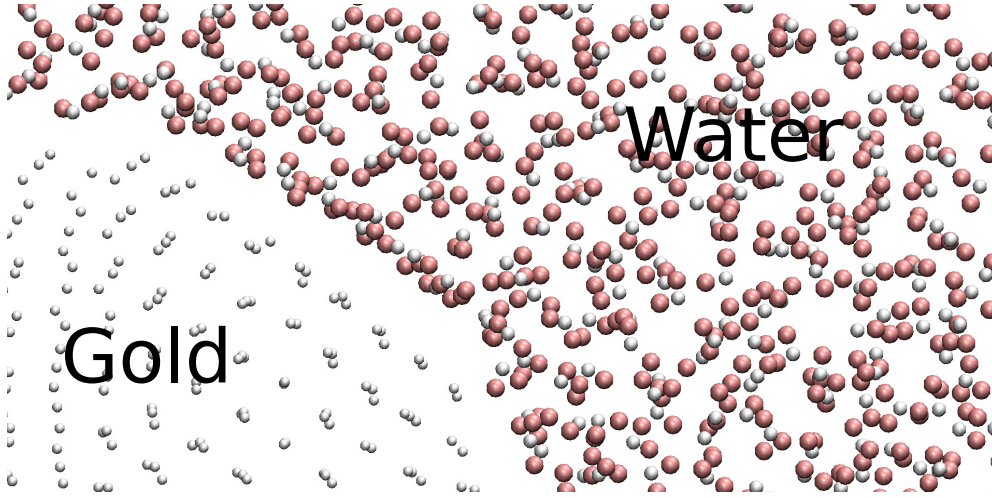


Figure 2.4: Close view of the interface between the nanoparticle of 6.5 nm and water at 310 K. The water shows no structure around the particle and the gold crystal itself starts to be unstructured.

Table 2.2: Thermal resistances of the interface (in $MK.W^{-1}$). R_{XY} states for the resistance between systems X and $Y = G$ (gold), W (water), P (polymer) and $R_{XY/Z}$ states for the resistance between systems $XY=X+Y$ and Z .

Resistance	from eq. 2.1	from MD
R_{GW}		4.59 ± 0.47
R_{GP}	4.07 ± 0.43	
R_{PW}	2.99 ± 0.23	
$R_{PG/W}$		3.05 ± 0.11
$R_{WP/G}$		4.18 ± 0.16
$R_{GW/P}$		1.73 ± 0.09
R_{eff}	2.78 ± 0.28	

interface. The results of this calculation is presented in the Table 2.2, this will be compared with the resistance between the gold and the water when a polymer is grafted on the gold surface. The equivalent conductance of this value is $G = 7.8 \text{ GW.m}^{-2}.\text{K}^{-1}$ which is higher than the value of $G = 150$ to $537 \text{ MW.m}^{-2}.\text{K}^{-1}$ found in previous calculations on water/gold nanoparticles using NEMD [113]. The fact that we used different interaction models, as well as a different geometry and a different computation method can explain that we find different results but this has not been investigated here.

2.4.2 Effect of polymer grafting on the thermal resistance

We now want to compare this resistance to the resistance of the same gold surface with a DHLA-Jeffamine polymer grafted on the gold surface via two

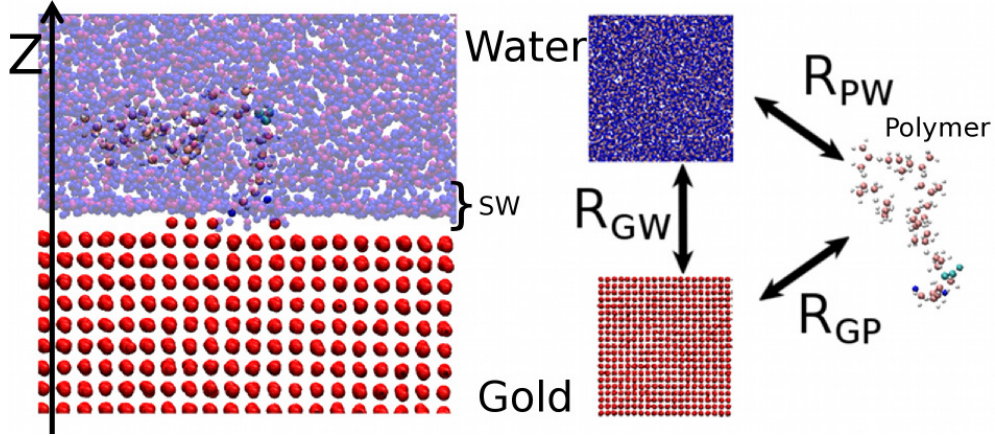


Figure 2.5: Gold/polymer/water interface description. The first layer of water (sw) is the structured layer seen as the peak of density as in Figure 2.3. The three systems that are the polymer, the gold and the water all have resistances between each other. These resistance are noted R_{GW} for the gold/water resistance, R_{PW} for the polymer/water resistance and R_{GP} for the gold/polymer resistance. Thus adding the polymer on the gold surface created two more interfaces.

thiol bonds. This is the fifth system we described before. Adding this polymer on the gold surface creates new interfaces that we present on Figure 2.5.

Our aim here is to compute the effective resistance between the water and the gold but the method we used previously to compute the resistance R_{GW} , the ΔT method, cannot be apply directly here as this method can only be apply to compute the resistance between two interacting systems which their ensemble must be isolated. However in our system there are three interacting systems: the gold, the water and the polymer. Similarly, the non-equilibrium method and the Green-Kubo method do not allow us to access to all the resistances present in the system. Only microscopic methods [21, 94] allow a complete access to the thermal resistances, but these methods can be difficult to use on liquids. To achieve our goal, we bypass the problem with the ΔT method noticing we can apply the method to compute the resistance between the system gold+polymer and water, $R_{PG/W}$, as well as the resistance between the system gold+water and the polymer, $R_{GW/P}$, and the resistance between the system water+polymer and the gold, $R_{WP/G}$. Furthermore, those resistances are linked to the one we are interested in by:

$$\begin{aligned}
 R_{GP/W}^{-1} &= R_{GW}^{-1} + R_{PW}^{-1} \\
 R_{WP/G}^{-1} &= R_{GP}^{-1} + R_{GW}^{-1} \\
 R_{GW/P}^{-1} &= R_{GP}^{-1} + R_{PW}^{-1}.
 \end{aligned} \tag{2.1}$$

So that the resistances of the different interfaces of our system presented on

Figure 2.5, can be extracted indirectly:

$$\begin{aligned}
 R_{\text{GW}}^{-1} &= \frac{1}{2} \left(R_{\text{GP/W}}^{-1} + R_{\text{WP/G}}^{-1} - R_{\text{GW/P}}^{-1} \right) \\
 R_{\text{GP}}^{-1} &= \frac{1}{2} \left(R_{\text{GW/P}}^{-1} + R_{\text{WP/G}}^{-1} - R_{\text{GP/W}}^{-1} \right) \\
 R_{\text{PW}}^{-1} &= \frac{1}{2} \left(R_{\text{GW/P}}^{-1} + R_{\text{GP/W}}^{-1} - R_{\text{WP/G}}^{-1} \right).
 \end{aligned} \tag{2.2}$$

Thus, we have a method to compute the resistances R_{GW} , R_{GP} and R_{PW} by Molecular Dynamics simulation using the ΔT method by computing first the resistances $R_{\text{GP/W}}$, $R_{\text{GW/P}}$ et $R_{\text{PW/G}}$. An example of the calculation of the autocorrelation function of the fluctuations of ΔT is presented on Figure 2.6. From the three resistances depicted on Figure 2.5, we can compute R_{eff} , the effective resistance between the gold and the water. This can be computed considering that there are two heat transfer channels between the gold and the water, one through the gold/water interface and another through the grafted polymer. We write:

$$R_{\text{eff}}^{-1} = R_{\text{GW}}^{-1} + (R_{\text{GP}} + R_{\text{PW}})^{-1}. \tag{2.3}$$

All the resistances computed are presented in the Table 2.2. The effective resistance R_{eff} is $2.78 \pm 0.23 \text{ MK.W}^{-1}$ while R_{GW} reaches $4.59 \pm 0.47 \text{ MK.W}^{-1}$, 1.65 times more. This is explained by the resistances of the interfaces water/polymer and polymer/gold, respectively 2.99 ± 0.23 and 4.07 ± 0.43 , which are both smaller than the gold/water resistance. This is quite surprising as these interfaces contain fewer atoms than the gold/water interface (28 nm^2 contact area). Thus, the polymer adds an extra thermal relaxation channel which the resistance is $(R_{\text{GP}}^{-1} + R_{\text{PW}}^{-1})^{-1} = 1.72 \pm 0.15 \text{ MK.W}^{-1}$.

2.5 Physical analysis of the interfaces

To understand the physical origin of the resistance differences observed in Table 2.2, we have computed the density of vibrational states of the various subsystems. The results are presented on Figure 2.7. This Figure shows that the cut-off frequency of gold is 8 THz while in the polymer and the water, it reaches 100 THz. In particular, there is almost no overlap between the gold and the water spectra, meaning the transfer between the systems is poor due to the selection rules and that explains the relatively high thermal resistance of the gold/water interface. At the opposite, the densities of states of the gold and the polymer largely overlap. This is specifically true with the sulfur atoms which are bonded to the gold by a thiol bond, a quasi-covalent bond. Moreover, it has been showed that covalent bonding between two systems induces a weaker thermal resistance [104, 150, 121]. The thiol bonds and the overlap of

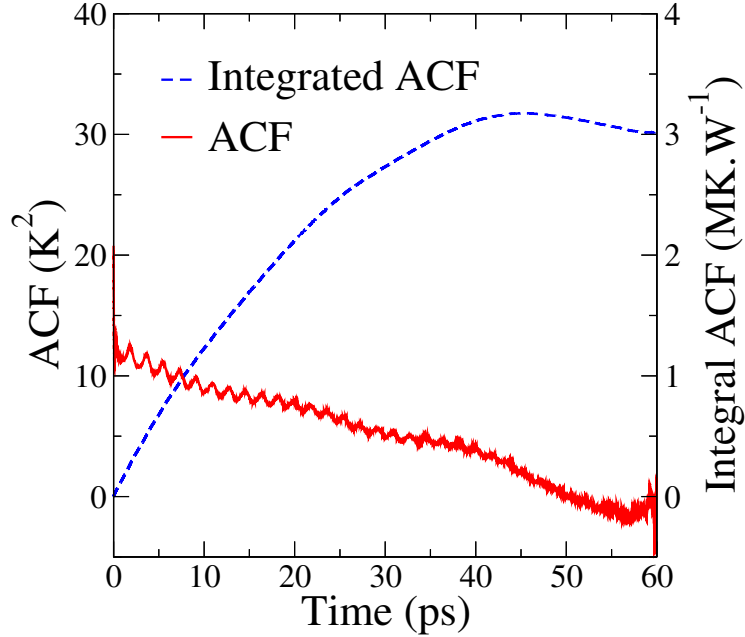


Figure 2.6: Autocorrelation function of the temperature difference fluctuations at the water/gold+polymer interface (red) at 310 K and its integral (blue) giving the resistance between the water and the gold+polymer.

the densities of states together explain the weakness of the gold/polymer resistance compared to the gold/water one, where the gold and the water interact through van der Waals forces only and their densities of states are separated. Similarly, the density of states of the polymer is very similar to the one of water and furthermore, the polymer is totally surrounded by water molecules. This explains the rather weak resistance between the polymer and the water. The polymer is thus a bridge between the gold and the water. This strategy has also been used to explain recent measurements partially validating our results between a gold surface and ethanol with polymers on the gold surface [166]. We have computed the frequency dependent vibrational transmission function [23, 22] between the gold and the polymer, and more specifically between the gold and the sulfur atoms which are attached to it. The method we have used was introduced by Chalopin [21] and allows computing the frequency dependent transmission between systems A and B interacting with each other in an equilibrium simulation. Chalopin showed that the transmission can be expressed with the atomic displacement u (u_i^α refers to the displacement of atom i in the direction $\alpha \in \{x, y, z\}$):

$$T(\omega) = \frac{1}{2k_B T} \sum_{i \in A} \sum_{j \in B} \sum_{\alpha \in \{x, y, z\}} \sum_{\gamma \in \{x, y, z\}} k_{i,j}^{\alpha,\gamma} [\dot{u}_i^\alpha(\omega) \bar{u}_j^\delta(\omega) - \bar{u}_i^\alpha(\omega) \dot{u}_j^\delta(\omega)], \quad (2.4)$$

with k_B the Boltzmann constant, T the temperature, $k_{i,j}^{\alpha,\gamma}$ is the inter-atomic

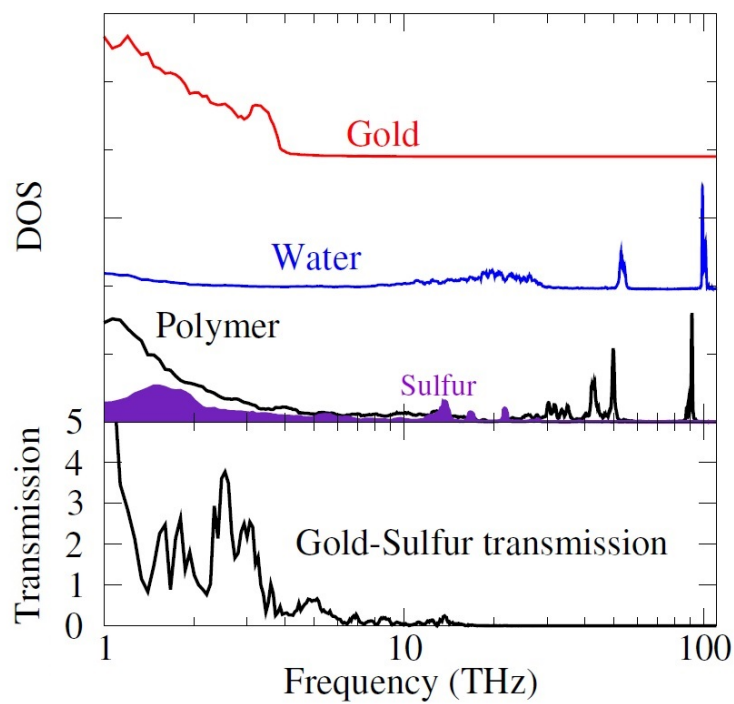


Figure 2.7: Transmission function and densities of states in the gold/polymer/water system at 310 K. The densities of states of the water and the polymer are close favouring the transmission of vibrations. The transmission function between the gold and the sulfur shows that there is a transmission channel at about 3 THz explaining the rather small resistance between those two systems.

force constant between atom i and j of systems A and B respectively. This expression can be rewritten as:

$$T(\omega) = \frac{1}{k_B T} \text{Re} \left[\frac{1}{i\omega} \sum_{i \in A} \sum_{j \in B} \sum_{\alpha \in \{x,y,z\}} \sum_{\gamma \in \{x,y,z\}} k_{i,j}^{\alpha,\gamma} \dot{u}_i^\alpha(\omega) \bar{\dot{u}}_j^\delta(\omega) \right]. \quad (2.5)$$

In our case, we apply this equation with A being the gold atoms interacting with the atoms of B, the sulfur atoms of the polymer.

This result of this calculation is also presented on Figure 2.7. This calculation reveals a major transmission channel at 3 THz. The transmission seems to diverge at low frequencies, but this is actually an effect of the Brownian motion of the polymer on the gold surface that drags gold atoms which induces strong a low frequency correlation. This is similar to what can be found in other liquid systems from previous studies [27].

2.6 Qualitative analysis by a transient non-equilibrium method

The analysis of the resistances in our interface model allows understanding some of the various specifications of the interface that matters in the design of systems to transfer energy for nanoparticles to their aqueous environment. For instance, we have seen that the density of states of the systems and the covalent bonding between the gold and the polymer involved explain the resistance hierarchy. However, when nanoparticles are used for hyperthermia, they are heated by the absorption of a laser pulse and then dissipate this energy in their environment in a transient regime. This is why we realized a transient non-equilibrium simulation to complete our equilibrium study by observing the spatial and temporal evolution of the temperature field at the vicinity of an initially hot gold surface.

We set the initial gold temperature at 1000 K and temperature of the water as well as the polymer is set at 310 K. We then register the temperature in the water as function of both the position and time, especially at 5 ps and 22.5 ps. We realise this study with and without the grafted polymer on the gold surface. The result is indicated on Figure 2.8. We find the result expected after our interface resistance analysis that the polymer decreases the interface resistance as it accelerates the thermal relaxation of the gold. This is showed by the fact that the temperature of water in the system with the polymer is always higher than in the system without the polymer. This simulation also shows the order of magnitude of the time constant of the heat transfer involved here. For instance we see that after 22 ps the water is still heating. This can be compared to the time necessary to transfer the energy absorbed by the electrons to the vibrational modes in the case of an irradiated nanoparticle, this transfer takes about ten picoseconds [100]. This simulation thus shows that we cannot neglect

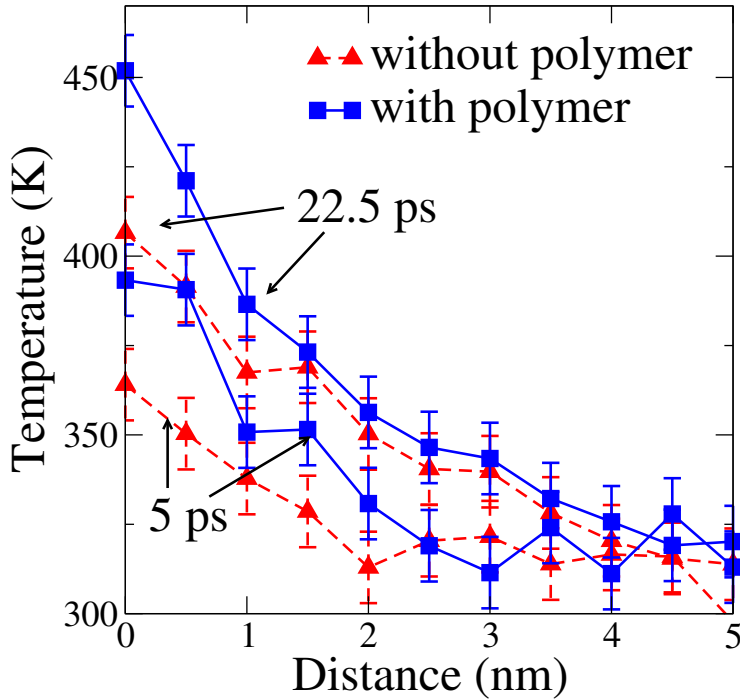


Figure 2.8: *Temperature profiles in water at the vicinity of the gold. These profiles have been compute at two times, 5 ps and 22.5 ps after the start of the exchange between the gold at 1000 K and the water at 310 K. This is done on the bare gold system (red) and the grafted gold system (blue). Each time, the temperature profile of the grafted interface is above the one of the bare interface.*

the transfer between the nanoparticle and the water during the thermalization of the electrons.

To complete Figure 2.8, we compute the isotherms in the water at different times and plot them in a space-time diagram in Figure 2.9, it illustrates that the temperature profile in the case with polymer is always above the one without polymer. In other words, a higher temperature is always firstly reached by the system with polymer and several picoseconds before it is reached by the system without polymer.

2.7 Generalization of the results

In our study, only one polymer is present on our 28 nm², for a density of about 0.04 polymers per nanometer square, and it induces a resistance reduction of a factor almost 2. We can generalize the equation 2.3 to compute the effective resistance when the surface polymer density is increased, but only under 2 approximations so that our resistance calculations remains valid:

1. the vibrational properties of the polymers are not affected by the inter-

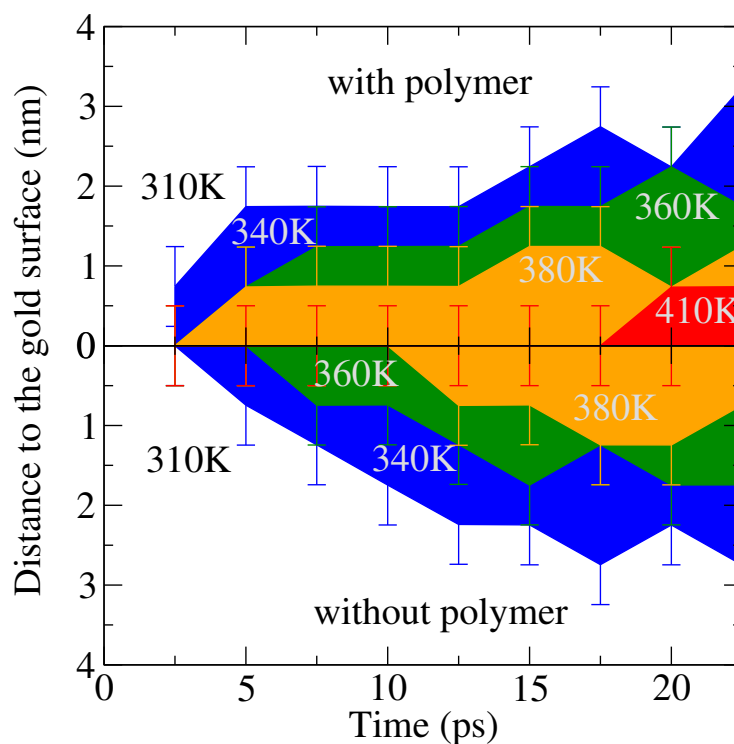


Figure 2.9: Space-time isotherm diagram. This figure completes Figure 2.8 by showing the temperature in the water at more time steps. The top part of this Figure is the system with polymer and the bottom part is without polymer. The frontiers between two colors represent space-time isotherms (with the errorbars of the corresponding color). This figure shows that the claim that the temperature is higher in the system with polymer is true at all time.

actions between the polymers.

2. the polymers do not screen the water molecules to the gold surface.

These hypotheses are valid until a surface polymer density of 0.7 polymers per nanometre square, i.e. 20 polymers on the surface of our previous system. There are two reasons for this:

1. at this density, the average distance between two polymers is 12 Å, which is the cut-off distance of the van der Waals interactions (modelled by Lennard-Jones potentials) and it is also from this distance that the Colombian interactions are approximated as they become very weak [63]. This weakness of these interactions between the polymers separated by 12 Å justifies the first approximation we made.
2. 0.7 polymers per nanometre square represents a covering of 10% of the gold surface if the polymer are unfolded (if all the polymers are folded on the gold surface, the covering reaches 80% of the surface, forming a monolayer that would screen the interaction between the gold and the water and thus would increase the gold/water resistance) but the gold/water resistance is inversely proportional to the contact surface area, thus the resistance would be increased by slightly less than 10%, which is acceptable considering the numerical errors on our resistance calculations (Table 2.2).

This conditions allow to consider that each polymer acts as a thermal relaxation channel and consider that the gold/water resistance, R_{GW} remains unchanged. We write an expansion of eq. 2.3:

$$R_{\text{eff}}^{-1}(N) = R_{\text{GW}}^{-1} + N(R_{\text{GP}} + R_{\text{PW}})^{-1}.$$

This will be a correct assumption up to $N = 20$ polymers on the surface. We can write again this to make the surface polymer density, n , appears as well as the effective surface resistance $r_{\text{eff}} = R_{\text{eff}}S$ and the gold/water surface resistance $r_{\text{GW}} = R_{\text{GW}}S$ where S is our surface area, $S = 28 \text{ nm}^2$. We have:

$$r_{\text{eff}}^{-1}(n) = r_{\text{GW}}^{-1} + n(R_{\text{GP}} + R_{\text{PW}})^{-1}. \quad (2.6)$$

We plot this function on Figure 2.10 showing the effective resistance as function of the surface polymer density. At $n = 0$ polymers per nm^2 , we find the previous resistance R_{GW} , then it decreases in $\frac{1}{n}$. At the 0.7 polymers per nm^2 , we find a resistance of 0.33 MK.W^{-1} which is about $\frac{1}{10}^{\text{eme}}$ of the gold/water resistance, and this is with about 10% of polymer covering ratio of the gold surface. The function represented on Figure 2.10 decreases as the inverse of the polymer surface density but when the polymer surface density increases, the average distance between the polymers decreases. When it becomes too small for water to fill the room between the polymers, the gold/water relaxation channel disappears and the gold relaxes only through the polymers. Furthermore, these polymers are not fully solvated which decreases the polymer/water contact surface and thus increases the polymer/water resistance. As a result, the multi-

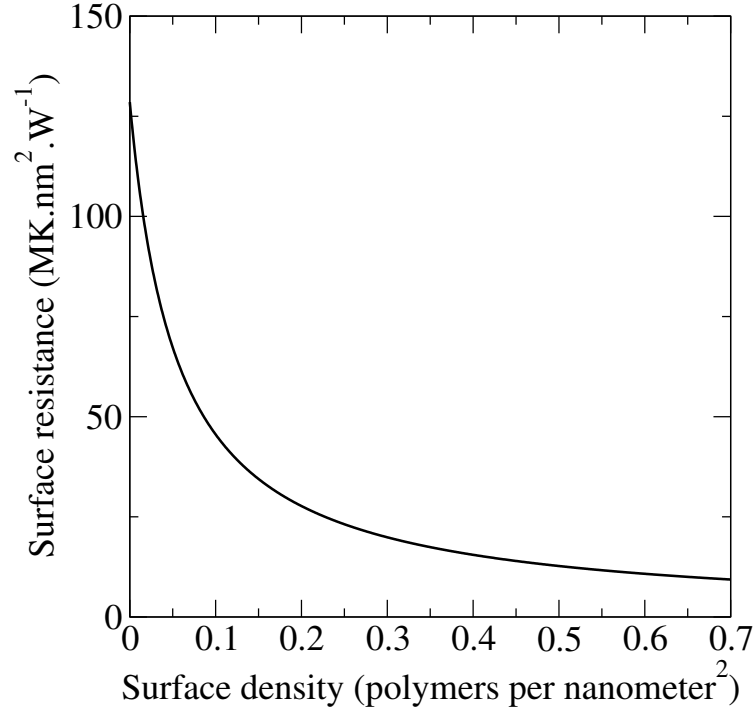


Figure 2.10: *Effective contact resistance extrapolated for higher polymer surface density on gold. Increasing the number of polymers on the gold decreases the effective resistance in $\frac{1}{n}$ with n , the polymer surface density.*

channel aspect vanishes to let place to an interstitial material between the gold and the water. So that the new effective resistance becomes:

$$R'_{\text{eff}} = R'_{\text{GP}} + R'_{\text{PW}} + \frac{L}{\lambda S} \quad (2.7)$$

where L , S and λ are respectively the thickness, the surface area and the thermal conductivity of the polymer layer. It not obvious if this would lead to a greater or smaller effective gold/water resistance and several parameters could change eq. 2.7 like the hydrophobicity of the polymers or again their length which, in addition to the curvature of the nanoparticle, could still lead to some solvation of the polymers.

2.8 Conclusion

A microscopic analysis of heat transfer at the interface between a gold nanoparticle and its aqueous environment has been developed. We first demonstrated that the curvature of the nanoparticle is negligible if its diameter is above 17 nm and that a planar model can be used. Then, our calculations show that attaching a polymer on the surface of a nanoparticle creates an extra heat

relaxation channel that dominates the gold/water interface. As a result, the total thermal conductance between the nanoparticle and the surrounding water is decreased from $G = 7.8 \text{ GW}\cdot\text{m}^{-2}\cdot\text{K}^{-1}$ for the bare gold/water interface by almost a factor of two for a density of 0.04 polymer per nanometre square. The analysis of the density of states and the transmission between the sub-systems of the model allows understanding that the decrease of the resistance is due to the similar relaxation frequencies in water and the polymer and to the covalent bonding between the gold and the polymer. This study is a first step toward new promising methods to design nanoscale systems for hyperthermia or drug delivery. However, this study is limited as the effect parameters of this interface such as the polymer length or the surface density, have not been investigated.

Part III

Lipid bilayers

Chapter 3

Lipid bilayer systems

3.1	Introduction	70
3.2	Self-organisation of lipids in water: bilayers, micelles and vesicles	70
3.3	Thermal properties of lipid bilayers	72
3.3.1	The lipid bilayers phases	72
3.3.2	Thermal behaviour	72
3.3.3	Heat conduction	75
3.4	Response to electric field	75
3.4.1	Electroporation	75
3.4.2	Nerve pulse propagation and axon models	76
3.5	Conclusion	79

3.1 Introduction

In nature, lipids are mostly known because they are part of the living cell membrane. The lipids are molecules with a hydrophilic head and a hydrophobic tail. In the context of cell membranes, Gorter and Grendel proposed in 1925 [53] that the lipids are organised in a bilayer structure due to their amphiphilic characteristic. The hydrophilic head points to water while the tail remains inside the bilayer. It is now well known that the lipid bilayer constitutes the main matrix of the cell membrane in which the proteins and ions channels are embedded. The cell membrane shape is also mechanically supported by the cytoskeleton. The membrane is thus an ensemble of different materials and molecules thus all its mechanical, thermal or dielectric properties are the result of the combination of those different elements. However, the properties of those constituents are not all known and specifically the thermal properties. Lipid bilayers being the main component of the cell membrane, their thermal behaviour is central in the relaxation in all living cells. In this chapter, a state of the art of the lipid bilayers structure and thermal behaviour is presented as well as the heat relaxation problem addressed in the following chapters.

3.2 Self-organisation of lipids in water: bilayers, micelles and vesicles

Lipids are amphiphilic molecules, their polar heads are hydrophilic and their tails are hydrophobic carbon chains. These chains can be of different length from one lipid to another and can contain several double bonds. As a result, the lipids in water organise in two layers with their heads toward the water and the carbon chains are facing each other inside the bilayer. A drawing of this structure is given on Figure 3.1. In water, depending on their concentration or on the external conditions, a bilayer is not the only accessible structure. The most probable structures are micelles and vesicles. Those last ones are very stable [60] and they are represented in Figure 3.2. To artificially fabricate proper bilayers in water, one needs to develop specific methods that will be detailed in further chapters.

As Figure 3.2 shows, micelles are not bilayers while vesicles are lipid bilayers closed on themselves. They can be used when studying lipid bilayers but only one side of the bilayer is accessible which limits the range of experiments achievable with vesicles. Different types of system are gathered under the name of vesicles:

- multilayer vesicles: vesicles of the order of a micrometer with several lipid layers as a membrane.
- small unilamellar vesicles: vesicles of the order of a few tens of nanometers form of only one membrane closed on itself as the one represented in Figure 3.2.

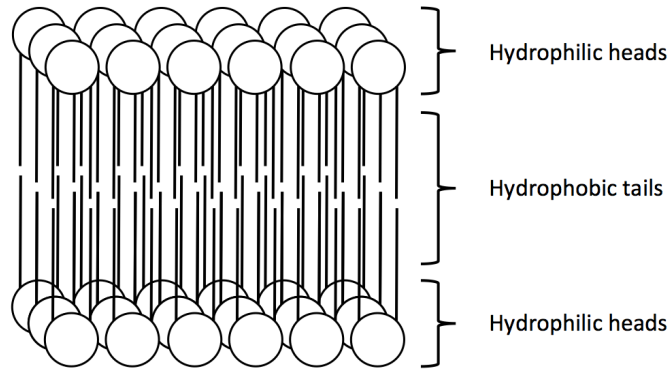


Figure 3.1: *Bilayer structure of lipids. In water, lipids can self-assemble as a bilayer, their hydrophilic head in contact with the water and the hydrophobic tails in contact with the tails of the other lipid layer.*

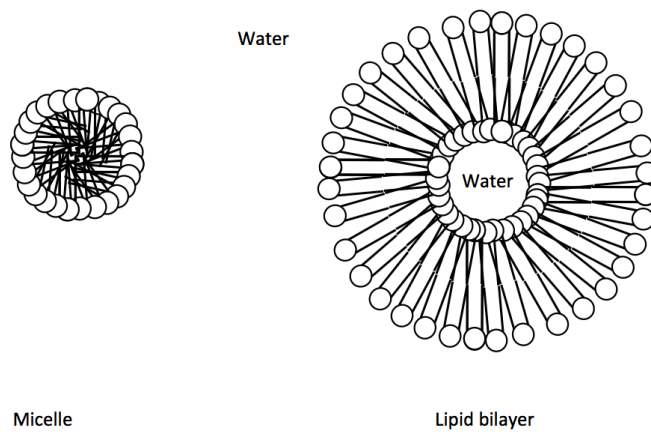


Figure 3.2: *Micelles and vesicles are the two spontaneously created form of lipid in water. The vesicles are basically lipid bilayers closed on themselves while micelles are not a lipid bilayer system.*

- large unilamellar vesicles: unilamellar vesicles of about 200 nanometers.
- giant unilamellar vesicles: unilamellar vesicles of 10 to 50 micrometers.

3.3 Thermal properties of lipid bilayers

3.3.1 The lipid bilayers phases

Bilayers can be found in several phases depending on the temperature and the lipid types forming the bilayer. The structure of the bilayer depends on the lipid: the dipole in its head and the length and unsaturation degree of its chains. The main phases are the gel phase and the liquid phase. The main difference between those phases is the area per lipid and the thickness of the bilayer. The gel is thicker than the liquid but the area per lipid is larger in the liquid phase. In addition to those main organisations other phases are accessible to the bilayer are [60, 169]:

- a crystalline phase where the lipids are ordered in the three directions. It is the L_c phase reported on Figure 3.3.
- a gel phase, where the lipids are often tilted by about 30° , this corresponds to the $L\beta$ and $L\beta'$ phases illustrated in Figure 3.3.
- a ripple phase made of a linear combination of gel and liquid phases. It is represented as the $P\beta'$ phase in Figure 3.3.
- a liquid phase. The lipids are disorganised and there is no periodicity. It is the $L\alpha$ phase depicted in Figure 3.3.

When the bilayer phase is ordered, in common cases, it takes the form of a two dimensional hexagonal structure. At lower temperatures, a cubic phase structure also exists. Those structures have been investigated using X-ray or neutron scattering [170, 181, 182].

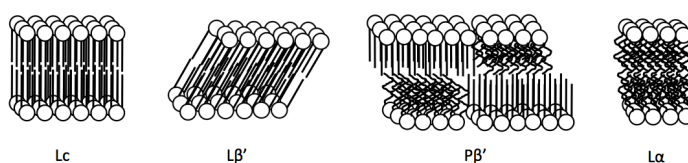


Figure 3.3: Lipid bilayers exist in different phases, crystalline (L_c), gel ($L\beta'$), ripple ($P\beta'$) or fluid ($L\alpha$) depending on the temperature. The higher the temperature, the less organised is the bilayer [60].

3.3.2 Thermal behaviour

A phase transition is the result of the reorganisation of the ensemble of the lipids and a phase transition temperature corresponding to the gel/liquid phase transition can be defined for lipid bilayer made of only one type of lipid. This phase transition is a first order phase transitions, as a consequence, the heat

capacity of the bilayer diverges at the transition temperature as illustrated on Figure 3.4 [169]. This Figure also shows that the per lipid volume in the membrane depends on the temperature. The increase of the volume is due to an increase of the lipid-lipid distance as the bilayer thickness is larger in the gel phase.

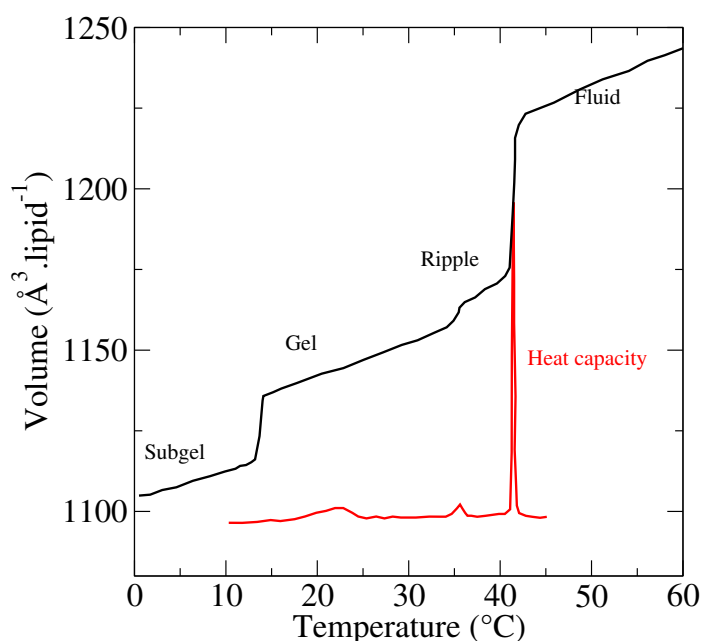


Figure 3.4: *The volume of a DPPC lipid bilayer increases with temperature and at each phase transition, the heat capacity is maximum and the volume changes rapidly [169].*

The transition temperature varies with the type of lipid constituent the membrane. The more saturated are these lipids, the higher the transition temperature. This mechanism is explained by the double bonds in the carbon chain in unsaturated lipids. This bond induces angle differences in the carbon chain preventing perfect stacking of the lipids and leading to more space between lipids as illustrated in Figure 3.5. As a result, the membrane is more flexible and "fragile" [136].

However, the melting temperature cannot be deduced from the unsaturation degree of the lipids because among lipids with the same unsaturation degree, the transition temperature varies. An example of the temperature values is provided in Table 3.1. The transition temperature depends on many parameters [146] such as the position of the double bonds in the chains, the lipid size, the polar head, etc ...

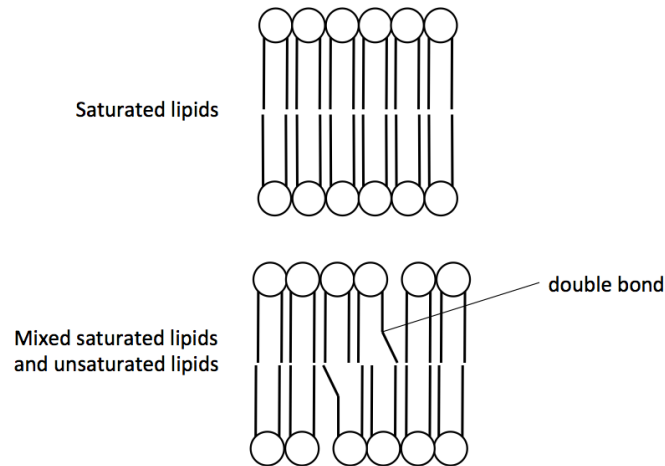


Figure 3.5: Unsaturated lipids have rigid angles due to their double bond(s), which prevents the perfect stacking of the lipids and disturbs the order of the bilayer.

Lipid common name	# of $-\text{CH}_2-$:# of $\text{CH}=\text{CH}$ (position)	Melting temperature ($^{\circ}\text{C}$)
DMPC	14:0, 14:0	23
DPPC	16:0, 16:0	41
DOPC	18:1 (9), 18:1 (9)	-20
DLPC	18:2 (9:12), 18:(9,12)	-53
POPC	16:0, 18:1 (9)	-2
DMPS	14:0, 14:0	35
DMPE	14:0, 14:0	50
DMPA	14:0, 14:0	50

Table 3.1: Melting temperature of different lipids from [146]. Those data show the effect of the double bond(s) in the lipid tails on the melting temperature. While there is no general law, there is a correlation between the number of double bonds and the melting temperature.

3.3.3 Heat conduction

The most un-addressed properties of lipid bilayers are their heat conduction properties. In most cases when modelling the heat conduction, the bilayer is neglected which is reasonable but with nanosystems being developed to act close to the bilayer and at short scale, this approximation can be questioned. Plus, when nanoparticles are injected into a living body, they often enter in the cell by being encapsulated into vesicles. Thus, if those particles heats up, the thermal conductance of the membrane is a part of the model. There is a Non-Equilibrium Molecular Dynamics simulation on a DPPC lipid bilayer in gel phase computing the in-plane and cross plane thermal conductivity [119]. The cross-plane thermal conductivity of the bilayer is found to be $0.25 \text{ W.m}^{-1}.\text{K}^{-1}$ and $0.10 \text{ W.m}^{-1}.\text{K}^{-1}$, in the in-plane direction. This difference is explained by the structure of the bilayer and the type of forces between the atoms. In the plane of the bilayer, the lipid are relatively far apart and interact through van der Waals and dipole-dipole interactions while in the cross direction, the atoms are covalently bonded except at the interface between the two monolayers. This layer-layer resistance is the main thermal resistance in the cross-plane direction. As a result, lipid bilayers conduct heat less than water and are a thermal barrier in the cell environment.

3.4 Response to electric field

Lipid bilayers are electric isolator as due to their structure, they are not permeable to ions. Their capacitance can be defined and measured experimentally and is commonly known to be of the order of 0.01 F.m^2 [14, 168, 15, 115, 137]. However, electrical fields are known to impact the lipid bilayer structure is the case of the electroporation, where a voltage induces the formation of holes in the membrane.

3.4.1 Electroporation

The electroporation consists in applying an electric on the lipid bilayer to increase its permeability. The application of a transmembrane voltage of at least 0.5 to 1 V on the membrane allows large molecules such as DNA to pass through the bilayer. Electroporation is commonly used to increase the permeability of cell membranes and introduce new coding DNA in a bacteria for instance [120]. Large molecule passing through the membrane indicates that this phenomenon is related to the creation of holes of nanometer scale in the bilayer. The mechanism proposed in many studies and numerical simulations [152, 151, 161, 162] is a local reorganisation of the lipids. Some lipids would gradually flip by an angle up to 90° forming a hole in the bilayer but the lipids still face the water with their hydrophilic head as indicated in Figure 3.6.

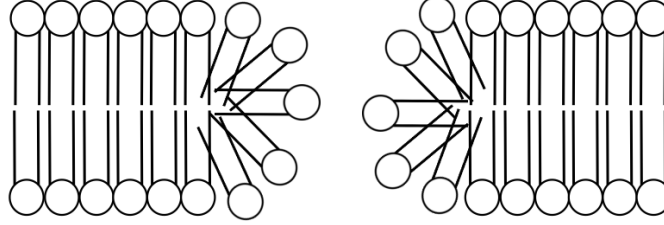


Figure 3.6: Organisation of the lipids in an electroporated bilayer. This structure is created when the transmembrane voltage is higher than a threshold of 0.5 to 1 V.

3.4.2 Nerve pulse propagation and axon models

The measurement of the effects of electric fields on lipid bilayers is motivated by the study of the nerve pulse propagation. A nerve is composed of a bundle of axons. An axon is a projection of a cell called neurone and is responsible of the transmission of information. Signals are carried by the neurones through the propagation of an action potential along the axon. This potential was measured by Cole and Curtis in 1939 on a squid axon [26]. It consists in a transient potential difference propagating along the axon. This measured potential is represented in Figure 3.7.

This potential propagation was later described by Hodgkin and Huxley [64] who considered the role of the ion channels in the propagation of this action potential. Considering that potassium and sodium channels are distributed on the membrane along the axon, they open after the voltage pulse and thus influence the potential in their environment and other channels in their vicinity. To quantify this process, the electrical model of the axon membrane that is depicted on Figure 3.8, has been taken from [60], have been introduced. Ion channels are modelled as resistances (R) or conductances (g), the lipid bilayer is a conductance and a leakage of ions I_L through it is considered. This scheme is repeated along an axon of radius a and resistance R_i . The equation describing the nerve pulse is established as follows:

$$\frac{a}{2R_i} \cdot \frac{\partial^2 U}{\partial x^2} = C_m \frac{\partial U}{\partial t} + g_K(U - E_K) + g_{Na}(U - E_{Na}), \quad (3.1)$$

where C_m is the conductance of the lipid bilayer, E_K and E_{Na} are the potential difference created by the different concentration of potassium and sodium respectively. Those quantities and their arrangement are represented in Figure 3.8.

This model is satisfying to describe the potential measurements carried out on axons but later experiments revealed [142, 163] that heat was released then absorbed from the axon when the action potential propagates. Experimental results from [142] are reproduced in Figure 3.9.

The transmembrane voltage is at most 100 mV and is thus smaller than the

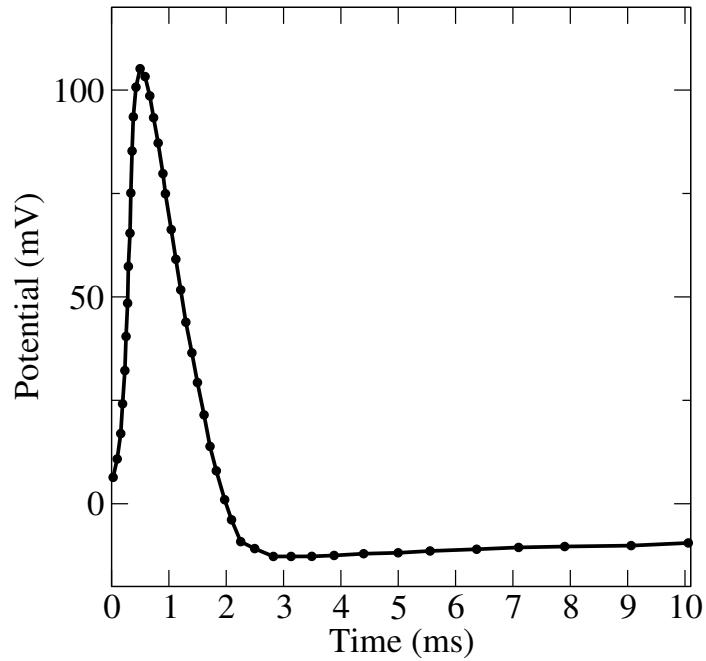


Figure 3.7: Transmembrane voltage measured during the action potential propagation [26]

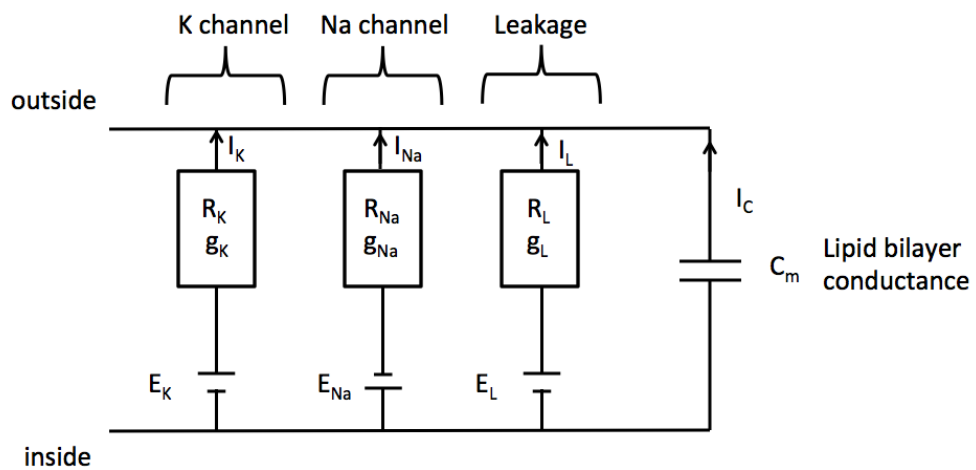


Figure 3.8: Electrical model of an axon as introduced in the Hodgkin and Huxley model for action potential propagation from [60].

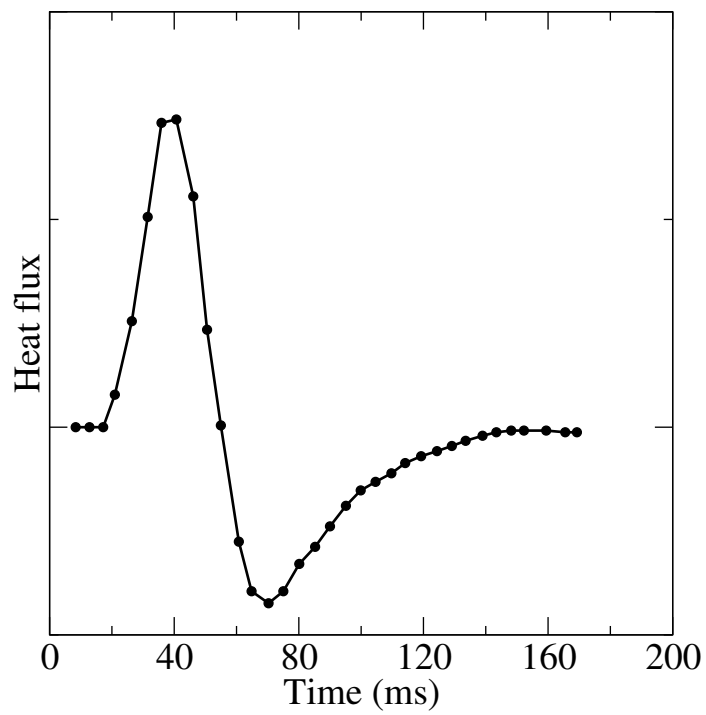


Figure 3.9: Heat released and absorbed during the action potential propagation from experimental data [142]. This reversible behaviour is similar to what is observed in phase transitions.

500 mV required for electroporation but this voltage might still change the structure of the bilayer. The release of heat followed by an absorption hints that this effect takes root in a reversible behaviour. It is thus plausible that this phenomenon, which cannot be explained by the Hodgkin-Huxley model, is due to a voltage-induced phase transition of the lipid bilayer, the voltage being here the action potential. This problem has been addressed by theoretical and experimental studies [159, 9] revealing that the electric field induces a change of the lipid bilayer structure or phase. The difference of energy between the gel and the liquid phase is $\Delta H \approx 30 \text{ kJ.mol}^{-1}$ [60] which can induce a heating of about 1°C of the bilayer.

3.5 Conclusion

In this chapter, the structural aspects of lipid bilayers have been presented and the common forms of those membranes in water have been introduced: small, large and giant unilamellar or multilayer vesicles. The thermal relaxation of lipid bilayers is mostly un-addressed. One numerical calculation studied the heat conduction in a gel DPPC lipid bilayer and has revealed that its cross-plane thermal conductivity is $0.25 \text{ W.m}^{-1}.\text{K}^{-1}$ and thus the membrane constitutes a thermal barrier in water. The most studied heat relaxation property in bilayer is the phase transition. The bilayer's phase depends on the temperature and the main phase transition occurs between the gel and the liquid at a temperature that depends on the lipid types that has been tabulated for pure lipid bilayers. However, the temperature is not the only way to affect the structure of a bilayer and it is known that electric fields increase their permeability by opening holes. This mechanism requires a transmembrane voltage of at least 0.5 V. In nature, the action potential, a transmembrane voltage of about 0.1 V is suspected to induce a reversible change of the bilayer structure due to a heat release followed by a cooling observed during the propagation of the action potential. As a result, the structure of the bilayer could be controlled by the application of electric fields and the hypothesis of a voltage-induced phase transition of the lipid bilayer is investigated in the following chapters.

Chapter 4

Dielectric properties of lipid bilayers

4.1	Introduction	82
4.2	Model description and calculation method	82
4.2.1	Model description	83
4.2.2	Calculation methods	83
4.3	Results	84
4.3.1	Static dielectric properties	85
4.3.2	Dielectric properties in the infra-red domain	87
4.4	The bilayer morphology and its effect on the dielectric properties	90
4.4.1	Links between the structure and the electric capacity	90
4.4.2	The effect of the structure and the infra-red absorption	93
4.5	Conclusion	95

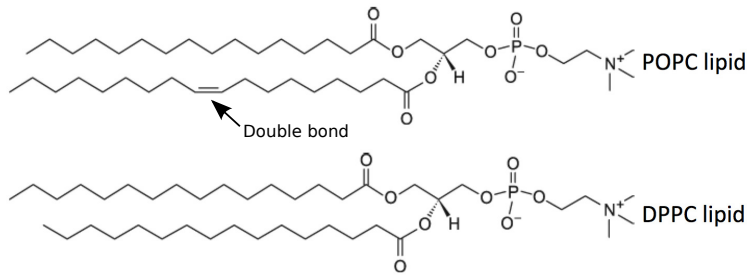


Figure 4.1: *Those two lipids are almost identical. The main difference between them is the double bond in one of the POPC tails (arrow).*

4.1 Introduction

The dielectric properties of lipid bilayers have been studied for years as they play a central role in the membrane ion or protein permeability [2, 34, 62, 50, 52] or in electroporation [127, 155, 151, 152]. Electroporation is an increase of permeability of the cell membrane by applying an electric field. In these applications, we actively act on the membrane to allow the drug delivery inside a cell. The dielectric properties are also involved in the interactions between the membrane and proteins [34] and thus very important to understand the biology or to be able to design systems to interact with membrane cell. The systems that are designed recently aim to deliver drugs or for hyperthermia [51, 157, 177, 111, 158, 73] in which the cell membrane is stimulated by heat or an electric field, static or not. Previous studies have reported that the static dielectric permittivity in the bilayer is not uniform [156] and it has been showed that the structure of the lipid bilayer can be controlled and thus, its permeability changed [93, 145]. However, there are no theoretical studies reporting the THz properties of simple membrane models. In this chapter, we build a Molecular Dynamic model to compute the polarisability of two types of bilayers, one made of DPPC lipids and the other of POPC lipids. These two lipids have very close chemical formulas but despite these similarities they self-organise into bilayers with different structures. This gives us the opportunity to enlighten the link between the morphology and the dielectric properties of a bilayer. Our results have been compared with Raman experimental results [98] we a fait agreement. We then focus on the connexion between absorption picks and the active dipoles position.

4.2 Model description and calculation method

We have studies two lipid bilayers with different structures. One of those bilayers is made of 1-palmitoyl-2-oleoyl-sn-glycero-3-phosphocholine (POPC) and the other one of 1,2-dipalmitoyl-sn-glycero-3-phosphocholine (DPPC). The skeletal formulas of those two lipids are showed on the Figure 4.1.

4.2.1 Model description

The main difference between those lipids relies in the double bond at the POPC lipid tail (see arrow on Fig.4.1). We have modelled the lipid bilayers at an atomistic level with the mean of molecular dynamics simulations (MD) by taking explicitly the interaction of the bilayer with water molecules. The DREIDING [110] (full atomistic) potential has been accounted for the lipids with an experimentally validated TIP3P interaction model [74] for the water molecules. The PPPM solver [63] is employed to compute the electrostatic interactions and the long-range interactions cut-off is 12\AA . The nucleus charges of the lipids are computed according to the Gasteiger algorithm [49]. The relaxation of the bilayers has been performed in canonical ensemble (NPT: pressure and constant temperature) for 400ps to ensure the cohesive energy minimization and using a Nosé-Hoover thermostat [65] (zero pressure, the target temperature and a damping parameter of 1000fs). Then, the optical and morphological properties are extracted from the displacement and velocity fluctuations of the atoms in the microcanonical ensemble (NVE: constant energy and volume) for 200000 steps with a 0.1fs time step to ensure the validity of the fluctuation/dissipation theorem (FDT) [87]. Our simulations include 72 lipids (about $50 \times 50 \text{\AA}^2$) and 6240 water molecules (about 50\AA of water above and under the bilayer) from 230 K to 370 K when exploring temperature dependent effects and 310K otherwise. All the results presented in this work have been ensemble-averaged with ten simulations to reduce the confidence interval.

Figure 4.2 represents the relaxed bilayers at 310K as they are in our Molecular Dynamics simulations. They have similar structure as what can be found in the literature [152, 151, 119]. Qualitatively, this Figure shows that the two bilayers have different morphologies despite the very similar lipids they are made of (Figure 4.1). This will allow us to compare the dielectric properties of two lipid bilayers were the main difference is the structure.

4.2.2 Calculation methods

We apply the fluctuation-dissipation theorem to the dielectric susceptibility (see Chapter 1) defined by:

$$\vec{p} = \epsilon_0 \chi \vec{E},$$

where $\vec{p} = \sum_{i=1}^N q_i \vec{r}_i = \vec{p}_z + \vec{p}_{||}$ is the dipole moment, with N, the number of atoms in the bilayer, and \vec{E} , the exterior electric field. As suggested by the symmetries of the bilayer, the polarisation will be split into its perpendicular and parallel components. We will do the same with the dielectric properties to follow the anisotropy of the bilayers. As $\langle p_z \rangle = 0$, by symmetry of the bilayer. We apply the fluctuation-dissipation theorem giving:

$$\chi_z(\omega) = \frac{\langle p_z^2(0) \rangle}{\epsilon_0 k_B T} + \frac{i\omega}{\epsilon_0 k_B T} \int_0^\infty \langle p_z(0) \cdot p_z(t) \rangle e^{-i\omega t} dt.$$

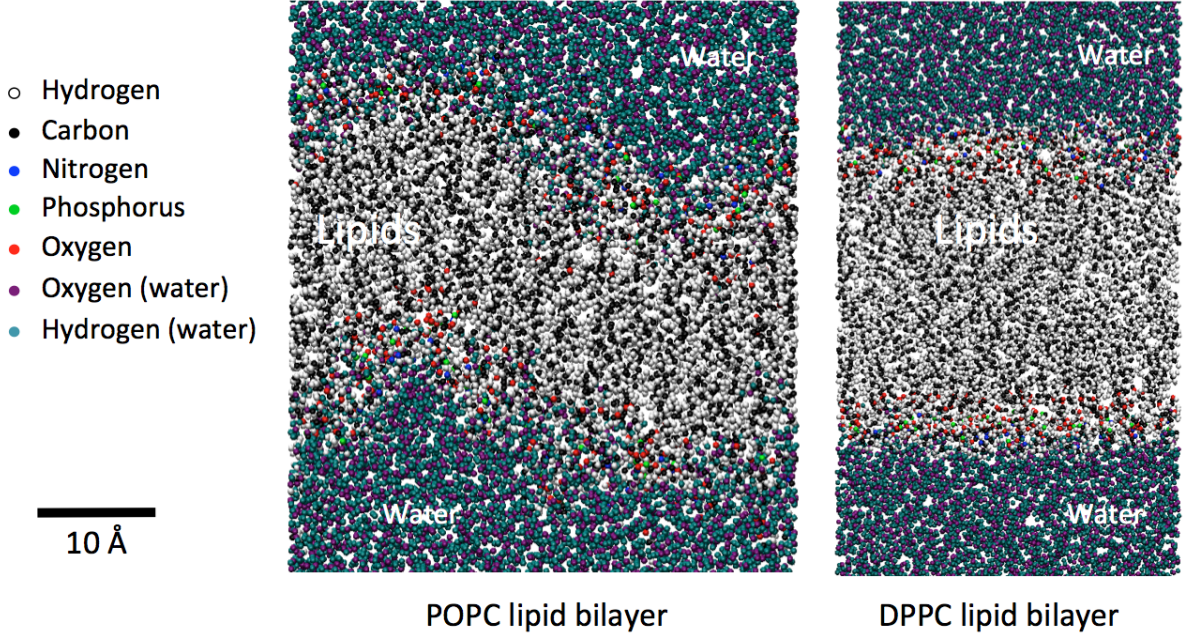


Figure 4.2: Atomistic representation of the lipid bilayers at 310 K. One is made of POPC lipids and the other of DPPC lipids. The DPPC lipids are closer to each other this explains why the POPC bilayer is wider.

It is important to notice that the susceptibility χ_z is not a continuous function of the frequency, so that the Wigner-Khinchin theorem cannot be applied and we must compute the polarisation directly.

We compute the polarisability of the bilayer along the axis perpendicular to the plane of the bilayer:

$$\alpha(\omega) = \frac{\langle p_z^2(0) \rangle}{k_B T} + \frac{i\omega}{k_B T} \int_0^\infty \langle p_z(0) \cdot p_z(t) \rangle e^{-i\omega t} dt.$$

The in-plane components of the polarisation are not zero on average. Thus we can compute the in-plane dielectric components of the lipid bilayer as

$$\epsilon_{x \text{ or } y}(\omega = 0) = \frac{\langle p_{x \text{ or } y} - \langle p_{x \text{ or } y} \rangle \rangle^2}{\epsilon_0 k_B T}.$$

We will split our results into two parts; the first part will focus on the static part of the dielectric constants ($\omega = 0$) and the second part on the infra-red domain (THz frequencies).

4.3 Results

We start by the static part ($\omega = 0$) of the polarisability and then we will focus on its frequency dependant part. It is mainly its imaginary part that is involved in the radiation absorption.

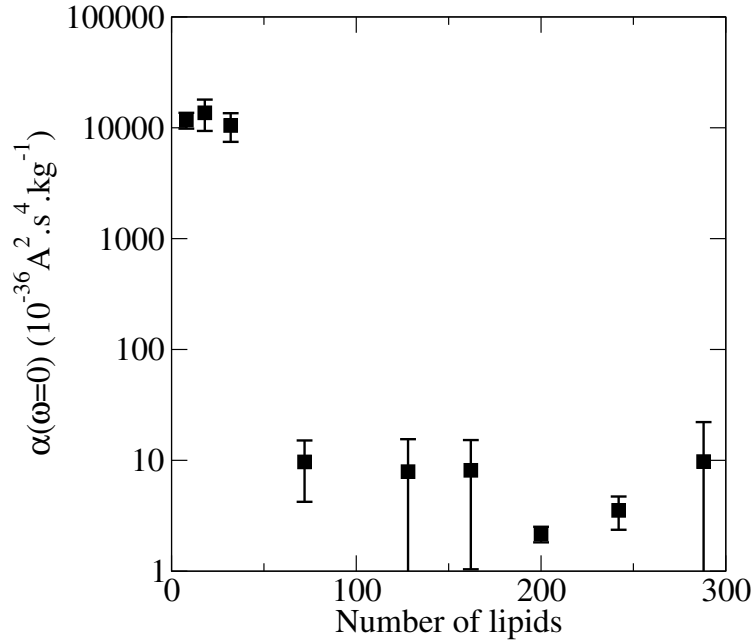


Figure 4.3: Size effect on the static polarisability of the lipid bilayer at 310 K. The static polarisability converges very quickly, at 72 lipids.

4.3.1 Static dielectric properties

4.3.1.1 Size effect

To account for the size effect in our bilayers, we first compute the static polarisability as function of the number of lipids. Thus, we build several simulations with more and more lipids. We used DPPC lipids for this study. We represented the static polarisability on Figure 4.3. This shows that it converges with less than 72 lipids. With fewer lipids, the polarisability is very high. As $\alpha(\omega = 0) = \frac{\langle p_z^2(0) \rangle}{k_B T}$, we can think that the perpendicular component of the dipole moment of the bilayer fluctuates very widely.

The dielectric permittivity in the plane of the bilayer can also be computed as the average between the ϵ_x and ϵ_y . We get Figure 4.4. Here we notice that the static permittivity converges in a way very similar to the polarisability.

As both quantities converge at 72 lipids, we will use this size for the temperature dependant calculations.

4.3.1.2 Electric capacity and static permeability of the bilayer

We have seen that the static polarisability has converged at 72 lipids; we can then compute this polarisability as function of the temperature. To be able to compare our results to experimental data, we can link the polarisability to the

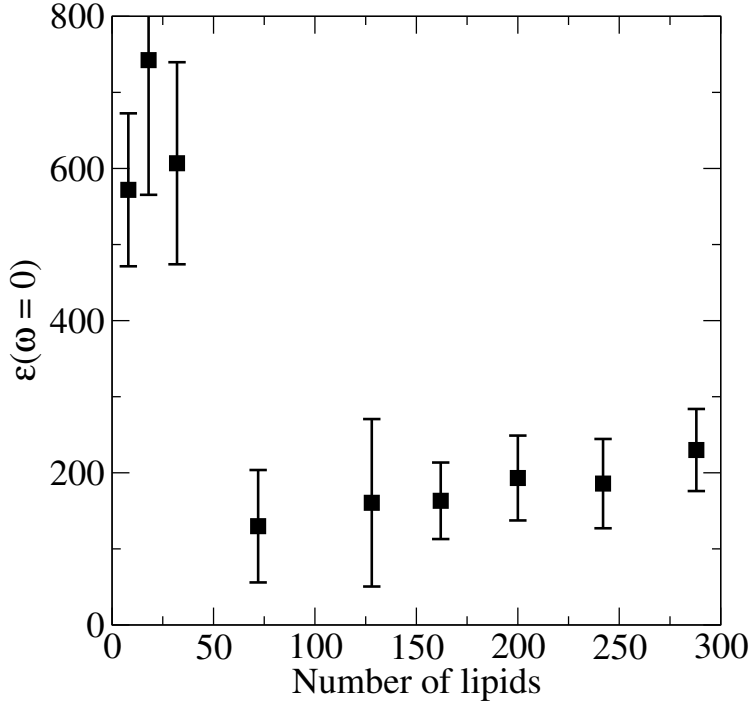


Figure 4.4: Size effect on the static permittivity in the plane of the lipid bilayer at 310 K. This shows similarly that the permittivity converges at 72 lipids.

electric capacity:

$$C = \frac{\left(\frac{\alpha(\omega=0)}{\epsilon_0 V} + 1\right)\epsilon_0 S}{d},$$

where d is the thickness of the bilayer, V its volume and ϵ_0 the permittivity of vacuum. We have computed both the polarisability and the electric capacity for both the DPPC and the POPC lipid bilayers and gathered the results on Figure 4.5. This Figure reveals that the polarisability doesn't depend on the temperature, for both bilayer, as well as the electric capacity. In the literature the effect of temperature is not accounted but the electric capacity of lipid bilayers has been found to be between 0.01 F.m² and 0.03 F.m² [14, 168, 15, 115, 137] which is compatible with our results. These measures have been realised on natural lipid bilayers that mixes different lipids and that explains that we find a range of results. Figure 4.5 tells us that the bilayer made of POPC lipids has a polarisability twice to three time larger than the one made of DPPC lipids. This is a first effect of the morphological differences of between the bilayers that we will explain later.

After the polarisability, we can compute the in plane dielectric permittivity of the bilayers as function of the temperature. We can plot the Figure 4.6 and we notice several things there:

- the dielectric permittivity in the POPC bilayer is larger than in the DPPC

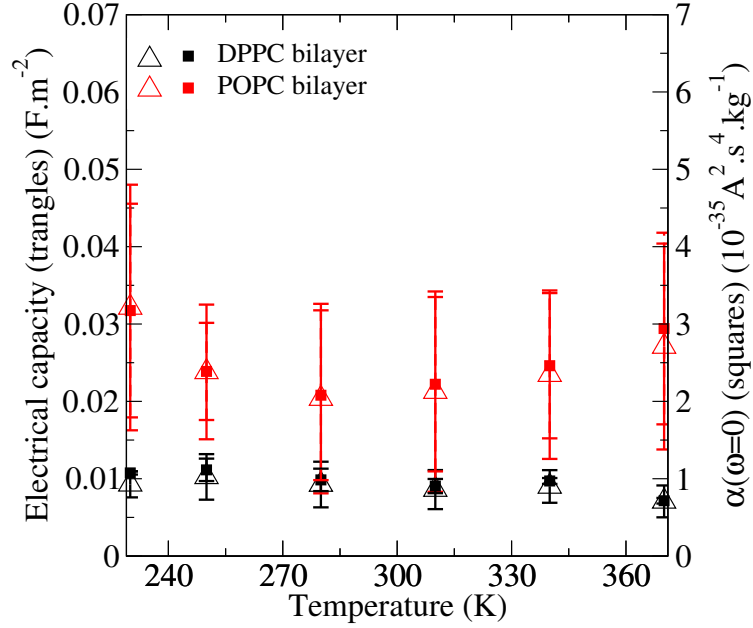


Figure 4.5: *Static polarisability and electric capacity of lipid bilayers as function of temperature. The temperature has no effect on the polarisability but the lipid type as a large impact as the POPC lipid bilayer as a polarisability three times higher.*

bilayer.

- in both cases, the permittivity is constant or decreases slightly with the temperature.

We get here an order of magnitude of the in plane permittivity but the error doesn't allow us to clearly show its dependence with the temperature.

4.3.2 Dielectric properties in the infra-red domain

The infrared absorption is responsible of the heat transfer by radiation to the bilayer. We won't be interested to the radiation above 100 THz (i.e. $\approx 3330 \text{ cm}^{-1}$ or $3 \text{ }\mu\text{m}$). Indeed, above this value, the absorption is mainly due to the electrons, no more the atomic dipoles. So this frequency domain is not accessible to us in Molecular Dynamics where there are no electrons in the models. To address the absorption, we have calculated the imaginary part of the polarisability, $\alpha''(\omega)$, in both our bilayers:

$$\alpha''(\omega) = \Im \left(\frac{i\omega}{k_B T} \int_0^\infty \langle p_z(0) \cdot p_z(t) \rangle e^{-i\omega t} dt \right).$$

The result is plotted on Figure 4.7 as well as a comparison with Raman spectroscopy measurement [98] and the densities of states of the bilayers. We haven't find measurements of the absorption spectrum under 40 THz (i.e. $\approx 1300 \text{ cm}^{-1}$ or $7.5 \text{ }\mu\text{m}$).

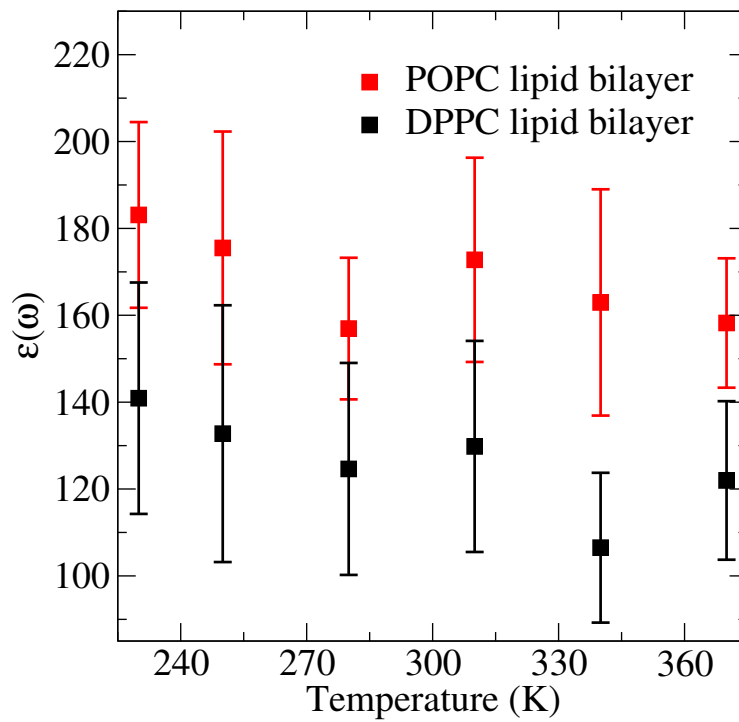


Figure 4.6: *In plane static permittivity of lipid bilayers as function of temperature. Alike the polarisability, the temperature has no effect but the lipid type plays a role and the less ordered POPC lipid bilayer has a higher permittivity.*

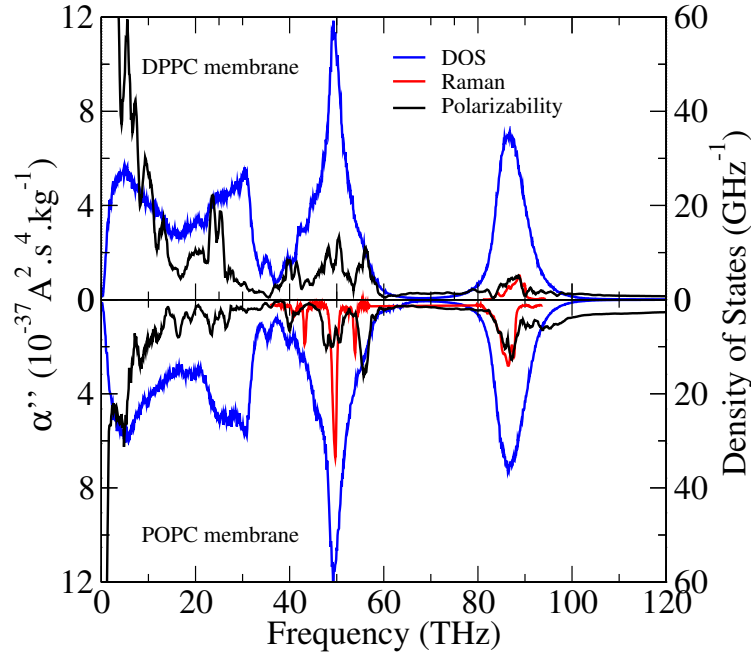


Figure 4.7: Absorption spectrum, Raman spectroscopy and densities of states of DPPC and POPC bilayers at 310 K. We calculated the absorption spectrum and the density of states and found good agreement with experimental data [98].

Figure 4.7 reveals a very good agreement between our calculations and the Raman measurements from about 90 THz to 100 THz where the absorption can be attributed to the dipoles involving the hydrogen atoms, like the C-H and N-H bonds activated at 85 THz and 100 THz. The agreement between our calculations and the experimental results is less good in the 50 THz range, the one where lies the frequencies of the C-C, C-O, C-N and P-O bonds. The densities of vibration states of the two bilayers are also represented on Figure 4.7, showing the density of states and the absorption spectrum have similar mode frequencies. This means that all vibration modes are activated in infrared, this is due to the fact that all atoms in our system are charged. However we notice that the relative intensities of the modes are different between the absorption spectra and the densities of states. The absorption spectrum is made by dipoles while the density of states is driven by the masses and speed of the atoms. We notice on Figure 4.7 that the absorption is large at low frequencies, where the largest dipoles of the lipids vibrate, the one located in the heads of the lipids.

4.4 The bilayer morphology and its effect on the dielectric properties

The dielectric properties of the two lipid bilayers we have calculated present both differences and similarities while the two lipids used to make the two bilayers are actually very similar, as showed on Figure 4.1. We thus turn to the bilayer's structure itself to look for an explanation for the differences in the dielectric properties and this is what this section is about.

4.4.1 Links between the structure and the electric capacity

We have previously showed in Chapter 4 that the electric capacity of the POPC lipid bilayer is three time larger than the electric capacity of the DPPC lipid bilayer. We have seen it, on Figure 4.2, the lipid organisation is different between both bilayers. Firstly, we can think that the capacities are different because of the volume difference, or the thickness difference. Another explanation would be the dipole distribution.

To quantify the morphological differences, we computed the densities of each element present in the bilayer along the axis perpendicular to the bilayer plane, those densities are gathered on Figure 4.8. This let us notice that the DPPC lipid bilayer presents only a small interdigitation, showed by the small density drop at the middle of the bilayer (indicated by the arrow) meaning the two monolayers does not intermix. At the opposite, the density in the POPC lipid bilayer reaches a maximum at its middle. This interdigitation induces a decrease of the thickness in the POPC lipid bilayer that is 5 Å thinner than the DPPC lipid bilayer, this has already been reported in the literature [79, 174, 91]. Another way to quantify the structure of the bilayer is to compute its radial distribution function in the bilayer plane. The definition and method to do this calculation is described in Chapter 1. We represented the distribution functions for both bilayers on Figure 4.9. They reveal that the POPC lipids are not as organize as the DPPC lipids. This results into two things visible on Figure 4.9, for the POPC lipid bilayer, the distance with the first neighbour is larger and the distribution function converges faster to the averaged density.

These differences can both be explained by the double bond indicated on Figure 4.1 by an arrow on the POPC lipids. This double bond creates an angle in the carbon backbone preventing those lipids to stack as well as the DPPC lipids. The distance with the first neighbour becomes larger, the density decreases and the greater space between the lipids allows an easier penetration of the tails of the lipids from the other monolayer, creating more interdigitation which reduces the thickness of the whole bilayer.

However, this morphological difference does not explain the different electric capacity but it let us presume the mobility of the lipids are different depending of the bilayer. This is confirmed by the standard deviation of the position of the lipids $\langle (x^2 + y^2) - (x + y)^2 \rangle$ that is larger by a factor 2 in the POPC lipid

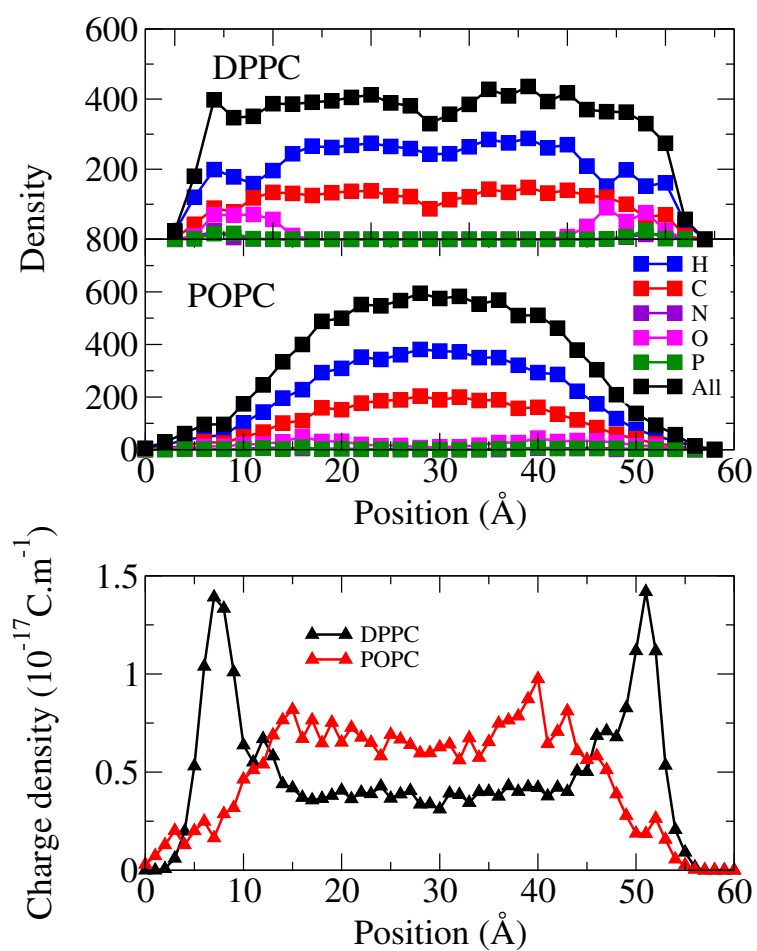


Figure 4.8: Per element density (up and middle) and charge density profiles in the bilayers (bottom) at 310 K. Those profiles reveal again the different structures of the bilayers and the charge density are equally impacted which partly explain our results.

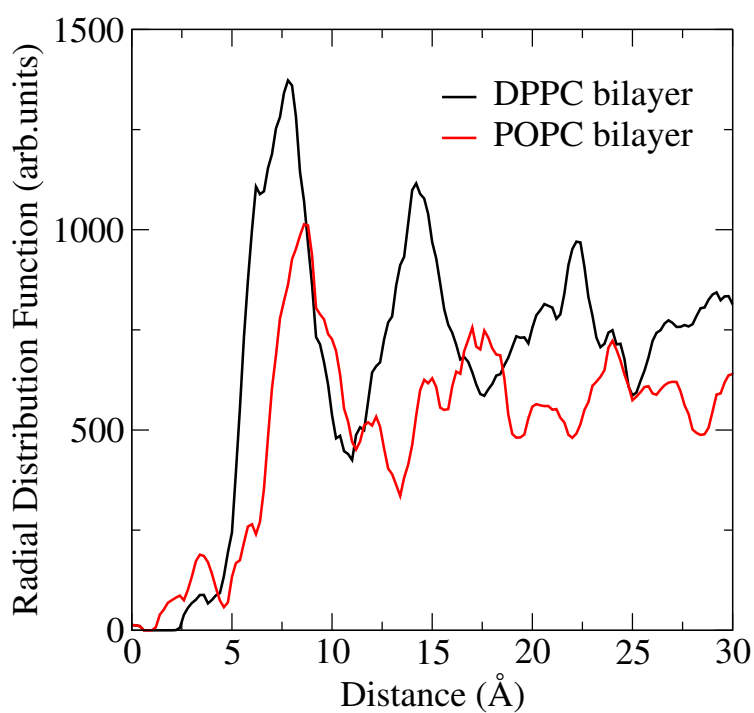


Figure 4.9: *Two dimensional radial distribution function of lipid bilayers at 310 K. In the DPPC lipid bilayer, the two dimensional ordering is observed up to 25 Å while in the POPC lipid bilayer it is lost after 15 Å. These curves also reveal that the lipid-lipid distance in a monolayer is larger with POPC lipids than with DPPC lipids.*

bilayer where it is 0.2810\AA against 0.1762\AA in the DPPC lipid bilayers (computed over 100 ps). If we know go back to Figure 4.8, we can notice the charges are mostly located in the hydrophilic heads of the lipids. The POPC lipids being more mobile, we think the angular fluctuations bring those dipoles in more perpendicular positions than the DPPC lipids. Indeed, when computing the ratio of the out-of-plane polarisation over the in-plane polarisation, $\left| \frac{p_z}{p_{||}} \right|$ in the monolayers, we find 0.0309 for POPC lipids and 0.0017 for the DPPC lipids. This difference, due to the space between lipids reducing the dipole-dipole interaction, explains that the electric capacity is larger with POPC lipids than with DPPC lipids.

The in-plane dielectric permittivity being larger in the POPC lipid bilayer (Figure 4.6) means that the fluctuations of the dipoles in the plane of the POPC lipid bilayer are larger than in the DPPC lipid bilayer. This could also come from the larger distance between POPC lipids and the smaller the dipole-dipole interactions, inducing more dipole fluctuations. The slight decrease of the permittivity with the temperature is a sign that the temperature is screening the dipole-dipole interactions between the lipids.

Going back to Figure 4.8, we see that the charges, and thus the dipoles are mostly in the heads of the lipids. Thus according to our analysis of the static permittivity and the polarisability, we can consider the lipids as big dipoles interacting with each other. The distance between those dipoles, and thus their mobility, is driven by the mostly uncharged lipid tails. Those tails give the general structure of the bilayer that will change the behaviour of the charges in the lipid heads and thus change the dielectric properties.

4.4.2 The effect of the structure and the infra-red absorption

In the case of the infra-red absorption, Figure 4.7 shows that the absorption spectra of both bilayers are very similar. This is quite surprising after having seen the morphological differences of the two bilayers but then where is this absorption occurring? By computing the absorption spectra as function of the axis perpendicular to the bilayer's plane with a 2\AA resolution, we were able to address this question with Figure 4.10.

The top of Figure 4.10 represents the local absorption averaged on the whole spectrum part available to our simulation. This Figure shows that the absorption in the DPPC lipid bilayer occurs mainly in the heads of the lipids (at about 40 and 85\AA), where the curve is maximal but in the bilayer made of POPC, the absorption is spread more homogeneously. The bottom part of Figure 4.10 represents the absorption at 53 THz as function of the position in the bilayers. We have chosen this frequency because it is the frequency of the C-C bond, which lie in the center of the bilayers so that we expect to have more homogeneous curves than with the total absorption. This is what we actually find but with several differences between both bilayers. These curves can be explain by noticing they mainly follow the charge density represented on Figure 4.8.

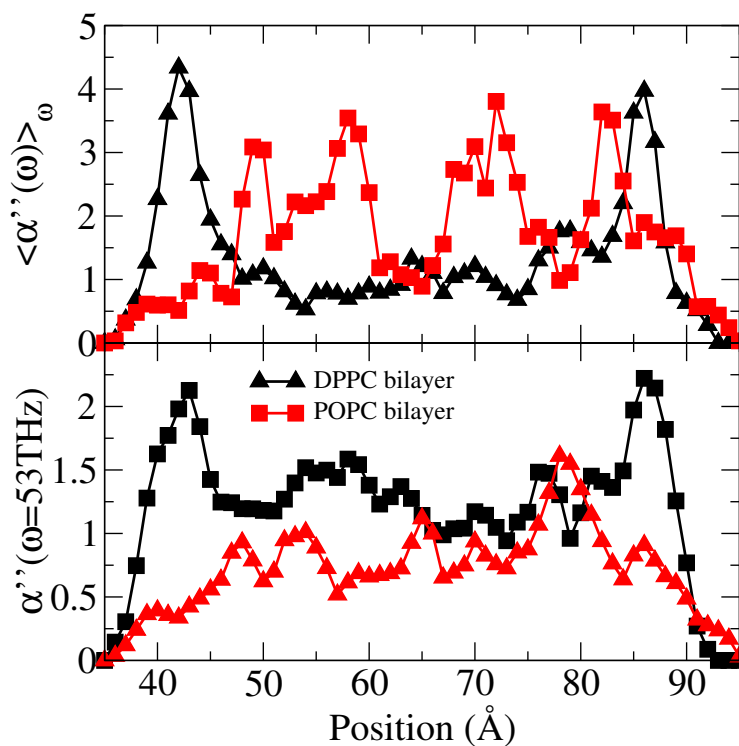


Figure 4.10: Average absorption (top) and absorption at 53 THz (bottom) as function of the position in the bilayers. The absorption in the bilayers different structures and are driven by the charges density profiles. Thus the absorption in the DPPC lipid bilayer is localised in the heads even at 53 THz which is the frequency of the C-C bonds. Oppositely the absorption in the POPC lipid bilayer is more homogeneous in the bilayer.

4.5 Conclusion

In summary, this work presents a first attempt to theoretically predict the IR-THz absorption properties of two types of lipid bilayer. We have based our approach on the fluctuation-dissipation theorem using molecular dynamics simulations. Our calculations have been compared with experiments. A good agreement is reported for the static and frequency dependent polarizability for the range of frequencies available in the literature. In addition, our analysis provides spectral data at lower frequencies (below 40 THz) where no experiments have been conducted so far. The physical origin of the polarizability has been further investigated:

- The temperature is found to have no effect on the static polarizability that differs by a factor of three between POPC and DPPC layers. This feature is explained by different structural configurations that allow more dipole fluctuations at the POPC hydrophilic heads.
- For the case of the IR spectra, both structures exhibit the same broadband absorption, ranging from 10 to 100 THz where the full vibrational spectrum is IR-active. Surprisingly, we found that for the case of the DPPC bilayer, IR absorption is strongly localized at the hydrophilic heads whereas for the case of the POPC bilayer, the absorption occurs more uniformly. This has been explained by the charge distribution. This approach opens the field to the study of the heating properties of biological systems when IR radiation plays a dominant role.

Chapter 5

Viscosity of a suspended DPPC lipid bilayer: effect of the solvent

5.1	Introduction	98
5.2	Experimental investigations	98
5.2.1	Phase contrast microscopy	99
5.2.2	Fluorescence Lifetime Imaging Microscopy (FLIM)	99
5.2.3	Molecular rotor for fluorescent lifetime imaging microscopy	100
5.2.4	Preparation of the suspended lipid bilayer	100
5.2.5	FLIM results	104
5.2.6	Experimental results analysis	105
5.2.7	Comparison with the fluorescence lifetime of the BOD-IPY in various lipid bilayer systems	109
5.3	Variation of the decane concentration in the bilayer from Molecular Dynamics simulations	109
5.3.1	Calculation of the splitting work	111
5.3.2	Concentration of decane as function of temperature	112
5.4	Prediction of the fluorescence lifetime variation	116
5.5	Conclusion	117

5.1 Introduction

In this chapter, it is intended to show that a phase transition of a lipid bilayer can be induced by an electric field. The experiment consists in applying different electric field on a bilayer, at different temperatures and characterise the phase of the bilayer by measuring its viscosity.

Using the cell membrane, such as the one of axons [106, 114, 67, 107, 164], is the easiest way to get a lipid bilayer, but this system includes different lipids and proteins. To study the variation of the viscosity with the electric field or the temperature, it is preferable to use a pure lipid bilayer with systems created *in vitro*. An easy technique is to dissolve lipids in water and let them self-organise into micelles or vesicles. Another system is the supported lipid bilayer which is made of deposited lipids on a surface. This system is ideal for force microscopy experiments [48]. A third technique was developed by Mueller in 1962 [118, 117], and then called the "painting method". Mueller described a method to create a suspended lipid bilayer in a hole, also called black lipid membrane. In this geometry, electrodes can be placed on both sides of the bilayer. This is why this technique has been widely used for electric capacity measurements [7, 179, 141] and also to study ions channel activities [61, 30, 124, 25, 134].

This system was chosen to conduct the experiments because of this advantage. The first step is the measurement of the viscosity by fluorescence lifetime imaging microscopy at different temperatures. Those results will be detailed in the first part of this chapter. Very surprising results were found as the viscosity of the bilayer increases with the temperature. The opposite trend was found in other lipid systems [183]. The hypothesis is that this behaviour is due to the presence of the solvent in the bilayer. This is tested by molecular dynamics simulations presented in the second part of this chapter.

5.2 Experimental investigations

The viscosity of the lipid bilayer is measured with a molecular rotor. The fluorescent lifetime of this molecule depends on the viscosity of its environment. As a result, measuring its fluorescent lifetime gives access to the viscosity of the bilayer. The phase transition is detected as the viscosity suddenly changes with the temperature.

To conduct these experiments, two microscopy techniques were used:

- phase contrast microscopy.
- fluorescence lifetime imaging microscopy (FLIM).

This part will first introduce those two microscopy techniques, then, the preparation of the suspended lipid bilayer and finally the FLIM results.

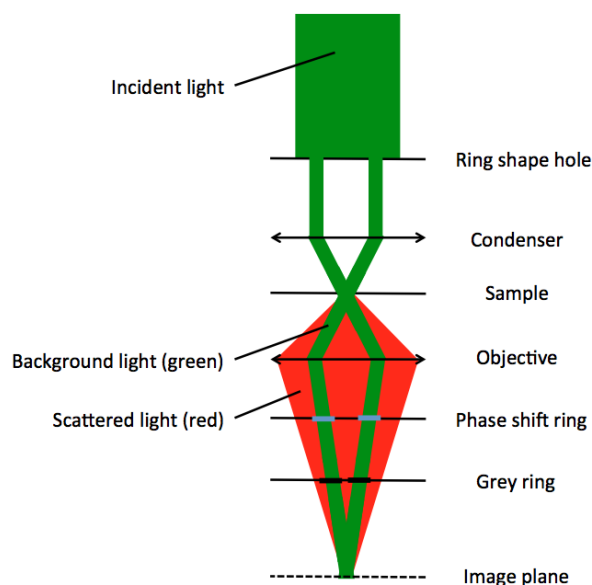


Figure 5.1: Sketch of a phase contrast microscopy set-up. The principle of phase contrast microscopy is to make the light scattered by the sample (red) interfere with the background light (green).

5.2.1 Phase contrast microscopy

When observing an object, by eye or with a camera, one sees the amplitude of the light emitted by this object. The amplitude varies if the object scatters or absorbs the light but the phase of the wave is normally not observable while it is also affected by the medium observed. This information is neglected even if it is more relevant than the amplitude.

The principle of phase contrast microscopy is to observe the phase difference of waves that went through different materials by turning it into brightness differences. The set up phase contrast microscopy is described on Figure 5.1. The incident light on the sample passes through a ring shape hole and then focused on the sample by the condenser. Part of this light is scattered and phase shifted by the sample but most of it is unaffected. The unaffected (background) light's phase is then shifted by $+90^\circ$ by a phase shift ring. Then a gray ring reduces its intensity to one comparable to the intensity of the scattered light. When both light are recombined, they interfere and create a brightness contrast.

5.2.2 Fluorescence Lifetime Imaging Microscopy (FLIM)

Fluorescence-lifetime imaging microscopy (FLIM) consists in imaging a fluorescence lifetime instead of fluorescence intensity. A pulsed laser excites fluorophores on the sample, and then they emit a photon according to their fluorescence lifetime. Each of those photons when received by the detector is reg-

Name	T Pulse-200 from Amplitude Systemes
Type	femtoseconde oscillator
Gain media	Yb:KYW (Ytterbium-doped tungstate crystal)
Repetition rate	10 MHz
Pulse width	407 fs
Output power	2.5 W at 1030 nm
Second harmonic generation	in β -BaB ₂ O ₄ at 515 nm
Power in experiments	a few hundred μ W at 515 nm

Table 5.1: Specifications of the laser used in all the fluorescence lifetime imaging microscopy measurements. 515 nm excitation corresponds to the absorption of the BODIPY and the power on the sample was decreased to a few hundreds of μ W (depending on the fluorescence intensity of the sample).

istered along with its time of arrival and position. This is repeated with each laser pulse and after a chosen exposure time, the fluorescence decay at different position in the sample is extracted. From this decay, the fluorescence lifetimes are computed and displayed on a two dimensional image. This technique needs a long exposure time (up to several tens of minutes). The measurements were performed at different temperatures applied with a hot sample holder in the microscope and then measured with a thermocouple in contact with the sample. The specification of the laser used in the experiment is given in Table 5.1. The set-up is presented on Figure 5.2.

5.2.3 Molecular rotor for fluorescent lifetime imaging microscopy

The molecular rotor used in the experiments is a BODIPY (boron-dipyrrromethene) developed by Dr. Marina Kuimova [66, 88]. Figure 5.3 shows its skeletal formula. This molecule is hydrophobic so it is present inside the lipid bilayers and not in the surrounding water.

This rotor's fluorescence lifetime depends on the viscosity of its environment and Dr. Kuimova published a study calibrating this dependence, the results from her paper are reproduced on Figure 5.4. This represents a bijective function that can be used to get the viscosity of any system the rotor is in.

5.2.4 Preparation of the suspended lipid bilayer

This experiment is conducted on suspended lipid bilayers made of DPPC lipids (bought at AVANTI polar lipids inc.). Its skeletal formula is presented on Figure 5.5. The lipids (powder) are solvated in decane with a concentration of 20 mg.ml⁻¹. If the lipids are in chloroform, they are evaporated before adding the decane. The skeletal formula of the decane is given on Figure 5.6. The molecular rotor is added to this solution in concentration of 1 for 800 lipids [88]. This solution is then injected in the chip depicted on Figure 5.7. This

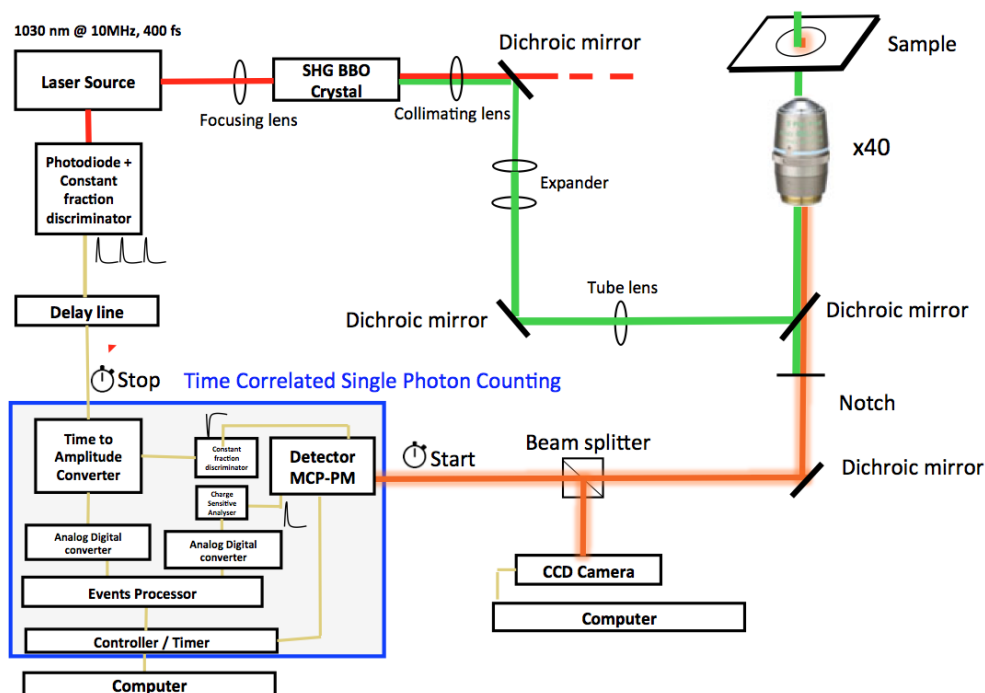


Figure 5.2: Set-up of the FLIM experiments.

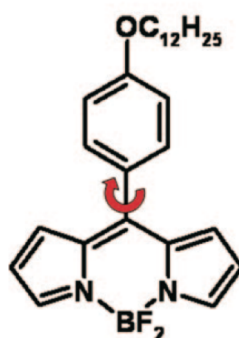


Figure 5.3: Skeletal formula of the BODIPY made by Marina Kuimova. Its fluorescence lifetime depends on the viscosity [88].

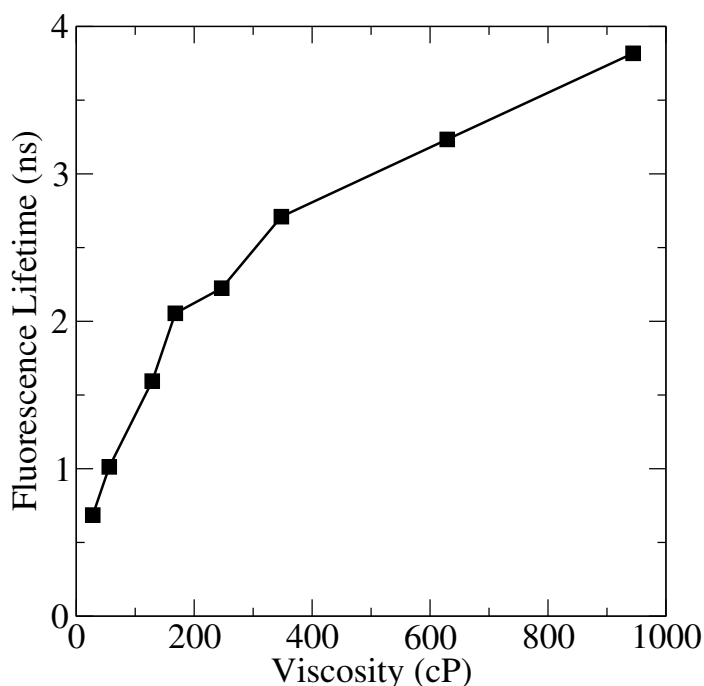


Figure 5.4: Fluorescence lifetime of the BODIPY as function of the viscosity published by Kuimova [88].

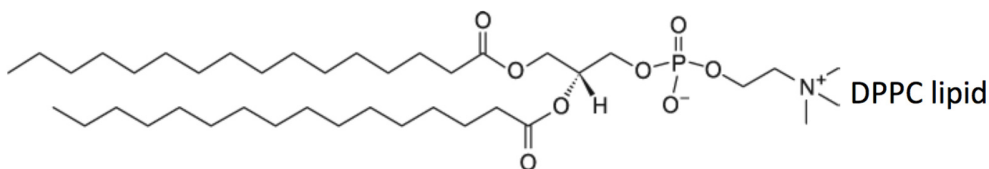


Figure 5.5: Skeletal formula of a DPPC lipid.

chip is made of a pool (1) with a parylene bottom (2) pierced by a hole (3) (usually 50 to 200 μm wide). This hole communicates with a channel (4) that runs under the pool. This channel can be filled from two extremities (5 and 6) far from the central pool (1). The different parts of this chip were made separately and glued by hand.

The procedure of the painting method exploits the amphiphilic properties of the lipids. When the lipid solution is in contact with water, the hydrophilic heads of the lipids will gather between the water and the decane. If the decane is then replaced by water, the lipid rearrange in a bilayer structure. The procedure with the chip is depicted on Figure 5.8:

1. filling the top central pool with water (phosphate buffered solutions (PBS)).
2. inserting some of the lipid solution in the channel beneath.
3. pushing the lipid solution under the pool with the PBS solution



Figure 5.6: *Skeletal formula of decane used as an organic as solvent.*

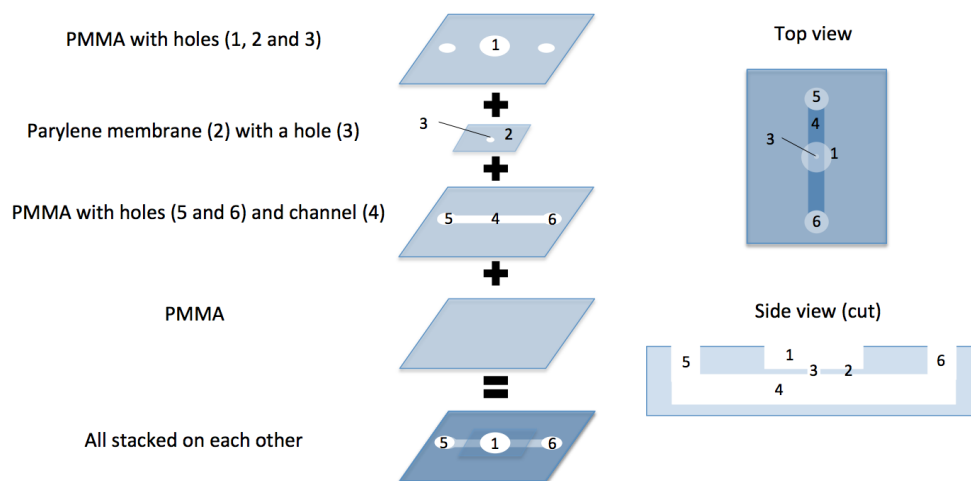


Figure 5.7: *Description of the chip for suspended lipid bilayers. This chip is made of a pool (1), a parylene membrane (2) pierced by a hole (3) and a channel (4) open at its extremities (5 and 6).*

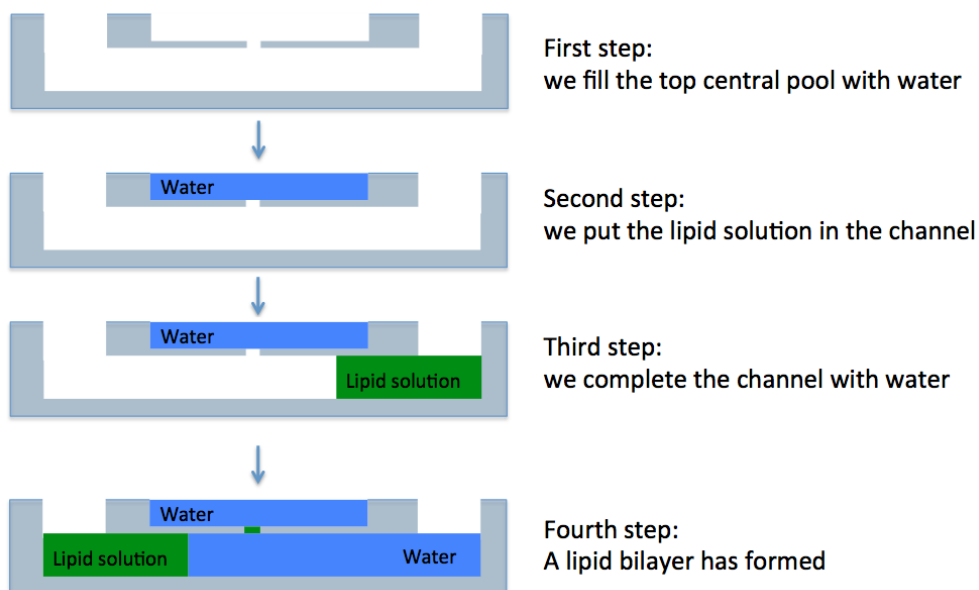


Figure 5.8: Procedure of the painting method.

4. when the parylene hole is surrounded by water, a lipid bilayer has formed. Once the lipid bilayer is formed at the center of the hole in the parylene it can be observed in phase contrast or fluorescence microscopy. Figure 5.9 (left) is the phase contrast image and shows that the hole is filled by a reservoir surrounding the lipid bilayer. The fluorescence image, Figure 5.9 (left), shows that the reservoir hosts the highest concentration of fluorophore. This is because it is made of the lipid solution and is thick compared to the central bilayer. Its fluorescence intensity decreases with the distance from the boundary of the hole because it becomes thinner. At the center, the bilayer is about 5 nm thin. As a result it hosts less BODIPY per surface area and is darker than the reservoir on the images. This system did not bleach which suggests that the fluorescent molecules in the reservoir come in the bilayer to replace the fluorophores. With this system, electrodes can be placed on both sides of the bilayer to apply a voltage. Checking that the current through the hole is zero has confirmed the presence of the bilayer.

5.2.5 FLIM results

FLIM image of the suspended bilayer allows us to map four regions in this system. They are depicted on the FLIM image on Figure 5.10. The colors on this image represent the different fluorescence lifetimes and the brightness represents the fluorescence intensity.

The regions identified on this image are:

1. a part not illuminated by the laser that does not fluoresce.

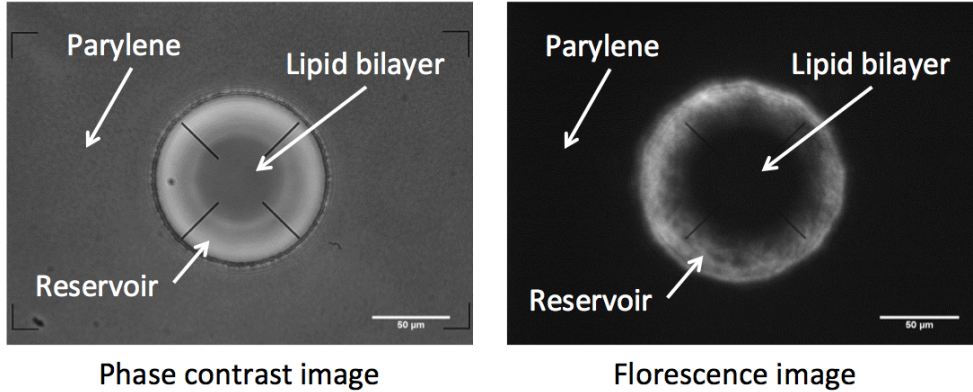


Figure 5.9: Phase contrast image and fluorescence image of the hole in the parylene with a bilayer showing the parylene, the reservoir containing lipids and decane and the lipid bilayer itself in the center on the hole. The bilayer is darker because it is thinner and thus holds less BODIPY.

2. the illuminated parylene that fluoresces with a homogeneous lifetime.
3. the reservoir around the lipid bilayer in the parylene hole. (Its fluorescence comes from the dissolved BODIPY.)
4. the lipid bilayer. The light from this part comes from the BODIPY dissolved in the bilayer.

The fluorescence decay of the fluorophores in the area #4 of Figure 5.10 is plotted on Figure 5.11 for different temperatures. This Figure shows how many photons are received from area #4 as function of time after the laser pulse. To extract the fluorescence lifetime, the curves are usually fitted by an exponential function but here, the fit requires a bi-exponential function with different lifetimes τ_1 and τ_2 :

$$Ae^{-\frac{t}{\tau_1}} + Be^{-\frac{t}{\tau_2}}. \quad (5.1)$$

The presence of two decays can originate from two populations of BODIPY in the bilayer. These occupy two distinct locations in the lipid structure meaning the BODIPY measure the viscosity of two different environments. In the following, τ_1 will be smaller than τ_2 .

5.2.6 Experimental results analysis

The two lifetimes from Figure 5.11 can be extracted and plotted as function of the temperature on Figure 5.12. This shows that both lifetimes increase with the temperature. Considering that when the lifetime increases it means that the viscosity increases ([88]), this result is surprisingly the opposite of the expected tendency. Indeed in most fluids, and in lipid bilayers [183], the viscosity decreases with the temperature.

Using Kuimova's calibration [88] with τ_1 (τ_1 is main lifetime as A is about ten times larger than B), the viscosity of the lipid bilayer is computed on Figure

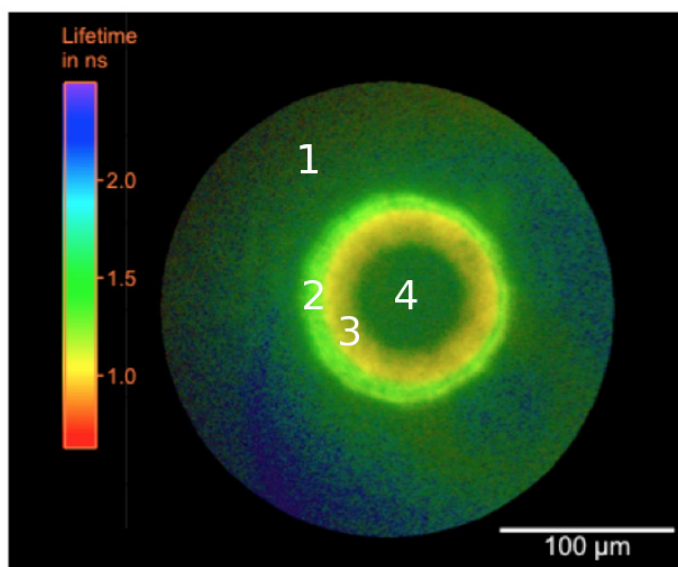


Figure 5.10: FLIM image of a suspended lipid bilayer. The colors on this image represent the different fluorescence lifetimes and the brightness represents the fluorescence intensity. On this image (1) is the area that is not excited by the laser, (2) is the parylene in the excited region, (3) is the reservoir made of the solvent, lipids and the BODIPY and (4) is the lipid bilayer.

5.13. The viscosity given by this lifetime is about 60 cP which correspond to the liquid phase viscosity of 90 cP [184, 81]. This could mean that the bilayer is in fluid phase but the other lifetime measured gives a viscosity of about 650 cP which is compatible with a gel phase. The viscosity depends on the environment of the BODIPY and the difference between the viscosities measured must originate from the different positions of the two populations of fluorophore. Figure 5.13 also shows that the viscosity tends to increase, but it is also shows that its dependence is not linear. It decreases after 310 K after increasing from 300 K to 310 K. Finally, there is a large variation between 305 K and 310 K, first decreasing, then increasing up to the maximum of the curve. This is the signature of the phase transition of the DPPC lipid bilayer (tabulated at 314 K). It is thus possible to consider that the increase of the viscosity is due to the phase transition. The bilayer is a gel at low temperatures and a liquid at higher temperatures. The viscosity at the transition varies oppositely to what is expected.

To check the validity of the experiments, the same measurements are performed on other lipid bilayer systems.

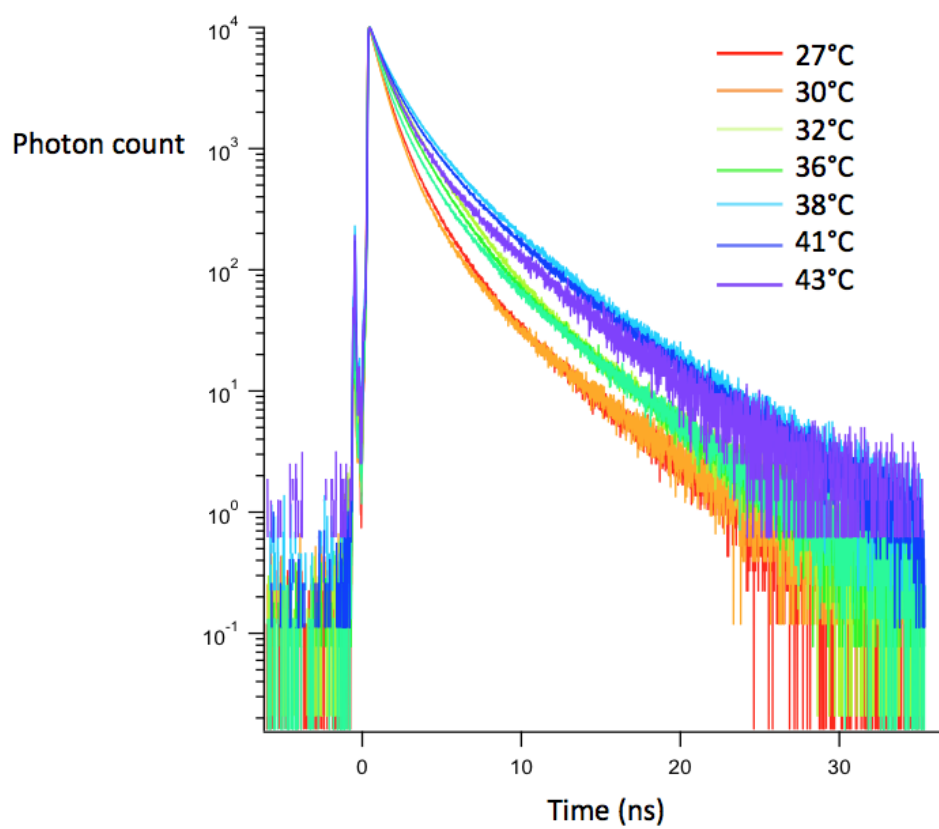


Figure 5.11: *Fluorescence decay in the lipid bilayer presenting a bi-exponential behaviour. This plot reveals that the fluorescence lifetime increases when the temperature increases.*

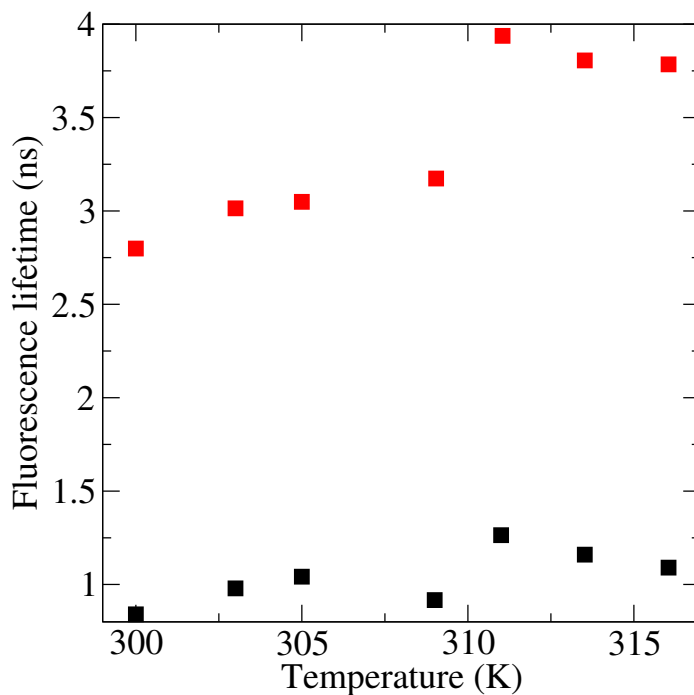


Figure 5.12: Fluorescence lifetimes of the BODIPY in the lipid bilayer computed by fitting Figure 5.11 with a bi-exponential function.

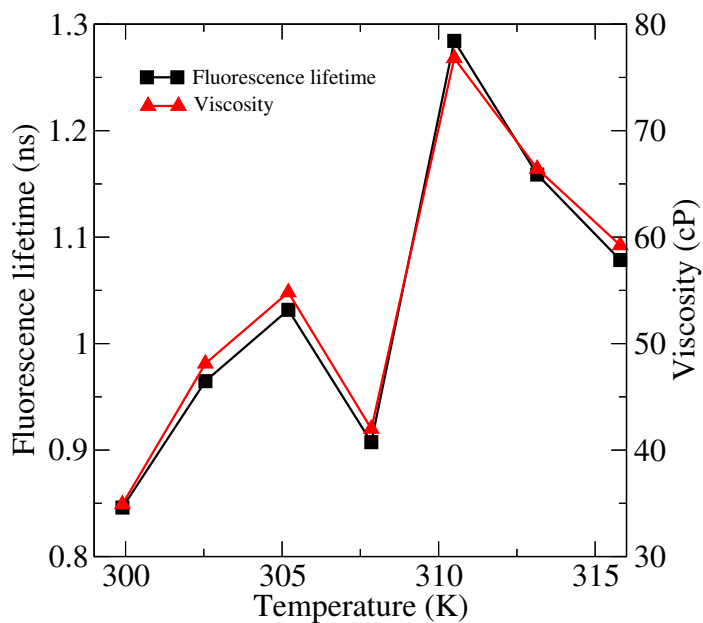


Figure 5.13: Fluorescence lifetime with the corresponding viscosity using the calibration of Kuimova 5.4. The fluorescence lifetime tends to increase with the temperature and thus the measured viscosity of the bilayer varies oppositely to the expected variation.

5.2.7 Comparison with the fluorescence lifetime of the BODIPY in various lipid bilayer systems

The same experiments were conducted on three other lipid systems:

- a lipid multilayer deposited on a glass surface. The procedure is to deposit the lipid solution on a glass surface and evaporate the solvent (decane or cholesterol).
- vesicles solvated in water. To grow them, the lipid solution is deposited on the bottom of a glass recipient, the solvent is evaporated and then the recipient is filled with water. It is then exposed to ultrasound to release the lipids in the water and they self-rearrange in vesicles.
- giant unilamellar vesicles (GUV). GUV are vesicles of several microns or tens of microns. The growing method is explained in Chapter 6.

The organic solvent is absent in those three systems.

The fluorescence lifetime of the BODIPY is measured in those three systems and the results are gathered in Figure 5.14. For all these three systems, the fluorescence decay was fitted with a bi-exponential function but unlike on Figure 5.13, the fluorescence lifetime in those three systems decreases when the temperature increases. The signature of the phase transition is also visible as a drop of the fluorescence lifetime.

The conclusion is that the increase of the fluorescence lifetime in the suspended bilayer is due to the presence of the solvent in the final configuration. The BODIPY diffuses from the reservoir to the bilayer and it is plausible that decane molecules diffuse as well in the bilayer. Previous studies on suspended lipid bilayers have also showed that they are not solvent-free [18, 180, 3, 59]. As a result, the decane could modify the bilayer's viscosity. The concentration of decane in the bilayer varies when the temperature changes resulting in the decreasing of the viscosity. In the following, this hypothesis is tested using Molecular Dynamics simulations.

5.3 Variation of the decane concentration in the bilayer from Molecular Dynamics simulations

For the viscosity to increase, the concentration of decane in the bilayer must decrease with the temperature. This could be explained by considering that when the temperature increases, the interdigitation between the two layers of the lipid bilayer increases which shoos away the decane molecules. Molecular Dynamics simulations are performed to investigate this possibility.

In this part is divided in three parts:

- the computation the work required to split the bilayer.
- the calculation of the size of the decane molecule (its gyration radius) inserted in the bilayer.
- the occurrence of a decane molecule getting in between the lipid layers.

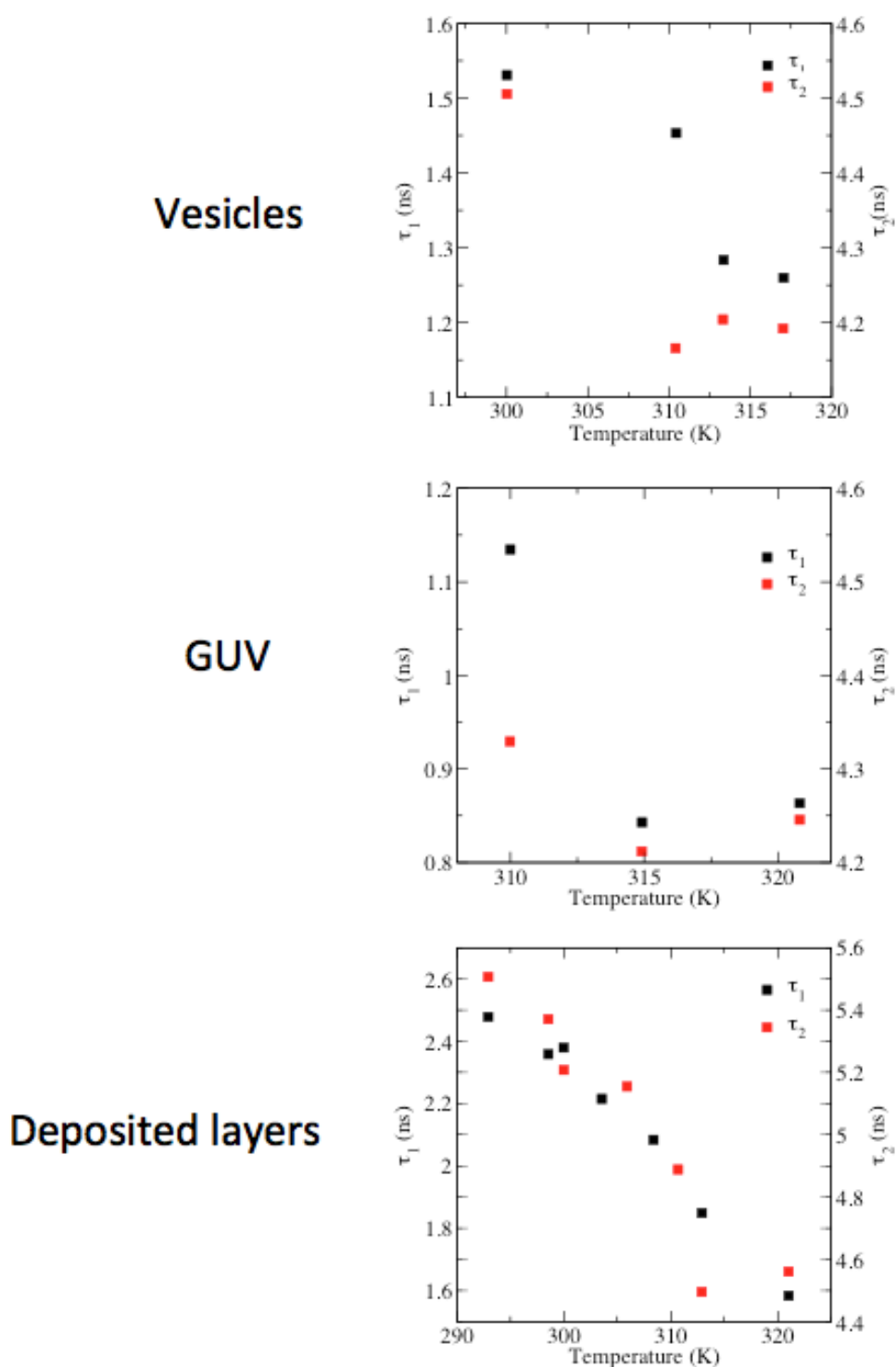


Figure 5.14: Fluorescence lifetime of the BODIPY in three different systems: vesicles, layers of lipids deposited on glass and Giant Unilamellar Vesicles. In those three systems the fluorescence lifetime of the BODIPY decreases with the temperature.

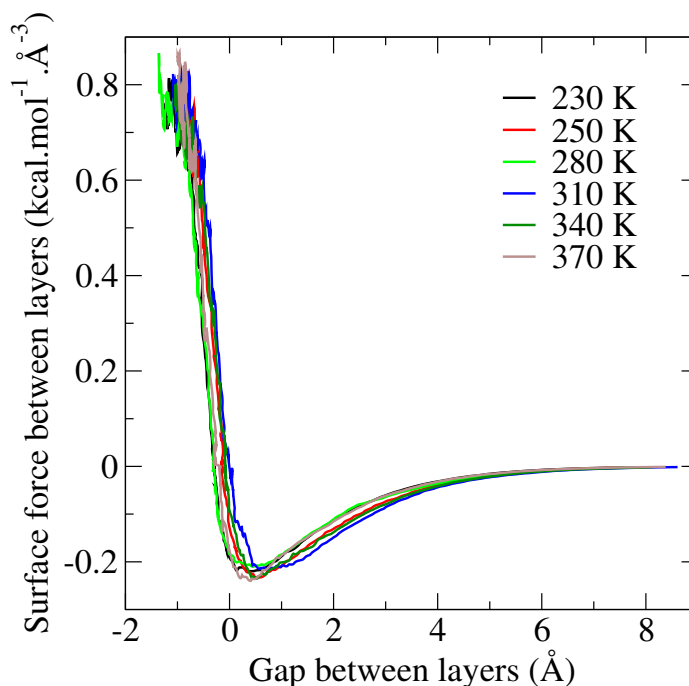


Figure 5.15: Forces between the layers of a DPPC lipid bilayer as function of their gap at different temperatures.

This is achieved at different temperature to extract the variation of the decane concentration with the temperature.

5.3.1 Calculation of the splitting work

To compute the splitting work, the force between the two layers of the lipid membrane is extracted as function of the distance separating them. The same Molecular Dynamics model of the DPPC lipid bilayer as described in previous Chapters 4 was used. A static force of $1 \text{ kcal.}\text{\AA}.\text{mol}^{-1}$ is applied to split the bilayer. During the expansion, the force between the two layers is computed. This force is defined as the sum of all the forces between an atom from one layer and an atom from the other layer. It includes both van der Waals and coulombic interactions. The force between the layers when compressed is computed using the same method but with an opposite force.

These simulations were performed at several temperatures and the results averaged over three simulations are gathered on Figure 5.15.

This figure shows that the interlayer force is zero at long distance and close to the equilibrium position (the one at the start the simulation) which is at negative distances (there is interdigitation of the layers.).

The extracted equilibrium gap Δz_{eq} at which $F(\Delta z_{eq}) = 0$ give the equilibrium interdigitation of the layers. There are represented as function of the

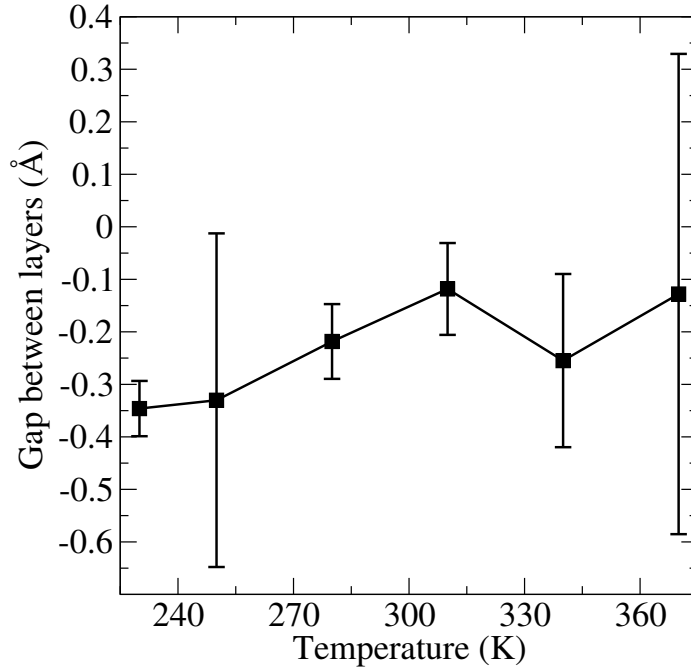


Figure 5.16: *Equilibrium distance between the two layers of the DPPC bilayer as function of the temperature extracted from Figure 5.15. These values are negative because the monolayers are slightly interdigitated. The error bars are the standard deviation from three different simulations.*

temperature Figure 5.16.

5.3.2 Concentration of decane as function of temperature

The work W required to split the layers by Δz is expressed from the equilibrium gaps and the force profiles F as:

$$\frac{W(\Delta z)}{S} = \frac{\int_{z=\Delta z_{eq}}^{z=\Delta z_{eq}+\Delta z} F(z) dz}{S}, \quad (5.2)$$

with S the contact surface between the layers.

The probability $P(\Delta z)$ to get a gap Δz on a surface s can be expressed using this calculated work:

$$P(\Delta z) \propto e^{-\frac{W(\Delta z)s}{Sk_B T}}. \quad (5.3)$$

Figure 5.17 displays this probability for different temperature (with here $s = 6.25\text{\AA}^2$). Finally, the probability to get enough space between the two layers to have a decane molecule can be extracted if its size is known.

The size of a decane molecule in the bilayer is computed from a Molecular Dynamics model of a solvated decane molecule inside a lipid bilayer. The decane molecule is modelled using the DREIDING potential [110] and its partial

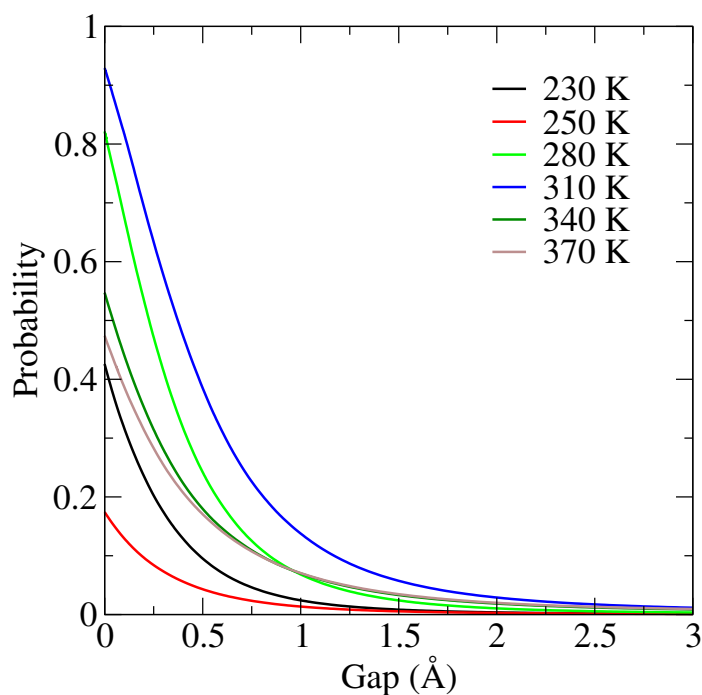


Figure 5.17: Probability to split the bilayer as function of the created gap for different temperatures.

charges computed with the Gasteiger algorithm [49], see Table 5.2. After 400 ps in NPT to equilibrate the system, the gyration radius in the three directions is extracted in NVE at different temperatures. The surface, s , and the thickness, e , of the decane molecule are derived from these data. Figure 5.18 shows the corresponding values. The thickness decreases with the temperature and the surface decreases with a jump at 310 K. The DPPC lipid bilayer has a phase transition at about 310 K which can explain the variations of the curves on Figure 5.18.

This distance and surface are injected in equation 5.2 to compute the work needed to insert a decane molecule in between the bilayer. The results of these calculations are displayed on Figure 5.19. Finally the probability, see equation $refP_{work}$, can be computed giving the curve on Figure 5.20.

This curve reveals that the probability increases with the temperatures, which does not explain the measurements. However, this curve is not monotonous and between 280 K and 310 K (the temperatures of the measurements), the probability decreases. Considering the errorbars, the conclusion is not clear and the probability could be increasing slowly.

ID	Type	Partial charge	Bonded to			
			1	2	3	4
1	H	0.083885	2			
2	C	-0.237246	1	3	4	5
3	H	0.083885	2			
4	H	0.083885	2			
5	C	-0.210169	2	6	7	8
6	H	0.098432	5			
7	H	0.098432	5			
8	C	-0.201005	5	9	10	11
9	H	0.09997	8			
10	H	0.09997	8			
11	C	-0.20009	8	12	13	14
12	H	0.100026	11			
13	H	0.100026	11			
14	C	-0.200055	11	15	16	17
15	H	0.100027	14			
16	H	0.100027	14			
17	C	-0.200055	14	18	19	20
18	H	0.100027	17			
19	H	0.100027	17			
20	C	-0.20009	17	21	22	23
21	H	0.100026	20			
22	H	0.100026	20			
23	C	-0.201005	20	24	25	26
24	H	0.09997	23			
25	H	0.09997	23			
26	C	-0.210169	23	27	28	29
27	H	0.098432	26			
28	H	0.098432	26			
29	C	-0.237246	26	30	31	32
30	H	0.083885	29			
31	H	0.083885	29			
32	H	0.083885	29			

Table 5.2: Atoms of the decane with their partial charges computed with the Gasteiger algorithm [49] and the atoms they are bonded to.

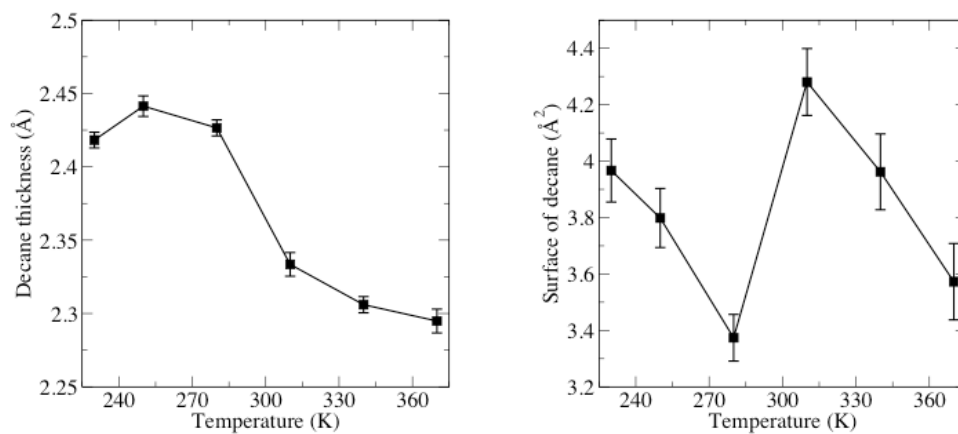


Figure 5.18: Thickness and surface of a decane molecule computed as the radius of gyration of the decane molecule embedded in a lipid bilayer.

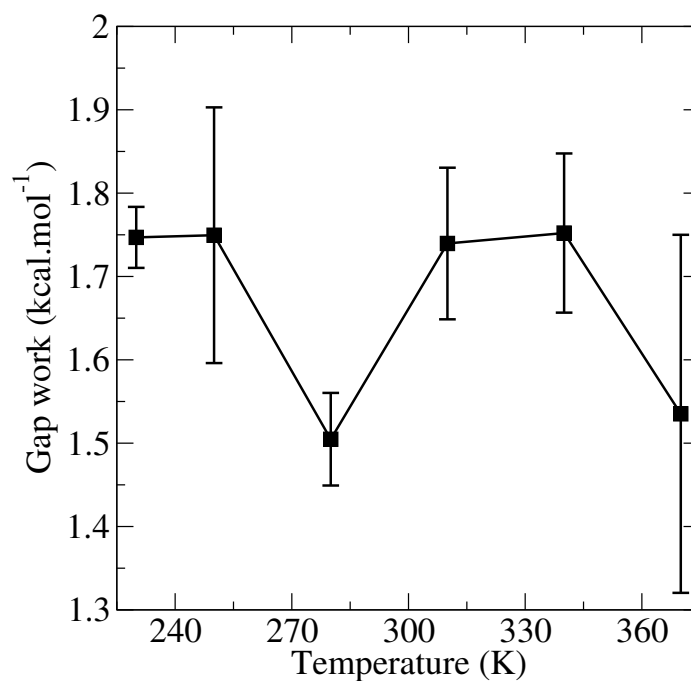


Figure 5.19: Work needed to insert a decane molecule inside the bilayer.

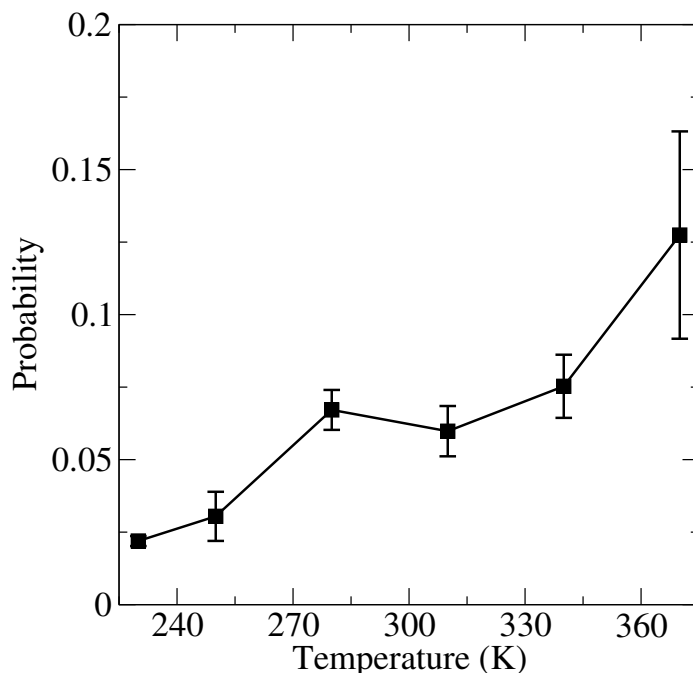


Figure 5.20: Probability to insert a decane molecule inside a lipid bilayer computed with the data from Figure 5.19 normalised by the partition function computed from Figure 5.15.

5.4 Prediction of the fluorescence lifetime variation

In the experimental system, the decane molecules are located in the reservoir and diffuse into the bilayer. The higher the probability of a decane molecule to enter between the layers, the easier it is to diffuse in the bilayer. As a result, the concentration of decane in the bilayer increases with the probability. In first approximation, it is assumed to be proportional to the probability at temperature T , $P(T)$:

$$C = AP(T). \quad (5.4)$$

A viscosity η is thus computed by composition of the viscosity of the bilayer (90 cP [184, 81]) and the decane (from about 4 cP at 250 K to 0.4 cP at 370 K [44]):

$$\eta \propto AP(T)\eta_{decane} + (1 - AP(T))\eta_{bilayer}. \quad (5.5)$$

The results on Figure 5.21 allow predicting the fluorescence lifetime of the BODIPY hypothetically dissolved in the bilayer. The simulations can thus be compared to the experimental results of Fig.5.13. As the probability on Figure 5.20 decreases, the viscosity decreases with the temperature. However, between 280 K and 310 K this decrease is slowed down and could be reversed but considering the errorbars of the calculations, this result is unclear.

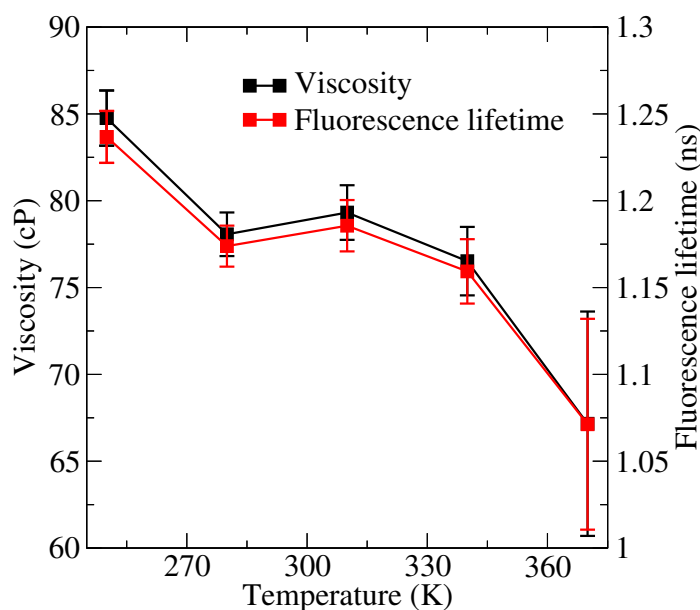


Figure 5.21: Predicted viscosity of a mixing of decane and DPPC lipid bilayer and the corresponding fluorescence lifetime of the BODIPY. This is computed by using the expected variations of the viscosity of both the lipid bilayer and the decane with the temperature. It overall decreases but the simulations reveal that the decrease is slower between 280 K and 310 K.

5.5 Conclusion

In summary, an investigation of the viscosity of a lipid bilayer as a function of the temperature has been conducted using both FLIM experiments on a suspended lipid bilayer and Molecular Dynamics calculations. The experimental results show that the suspended bilayer's viscosity increases with the temperature, and especially at the phase transition temperature occurring at about 310 K. This unexpected result can be explained if the solvent molecules localised in the bilayer are shoed due to the increase of the interdigitation with the temperature. This hypothesis was assessed using a Molecular Dynamics simulations based on the computation of the work to insert decane molecule in the bilayer. This calculation allows computing the variation of the concentration of the solvent in the bilayer and the results are in agreement with the experimental measurements. The phenomenon highlighted in this chapter reveals that suspended lipid bilayers are not the good system to investigate the viscosity of lipid bilayers as function of the temperature and voltage. To measure the influence of an electric field on the bilayer, another lipid system, Giant Unilamellar Vesicles, have been selected and the experiments conducted are detailed in the next chapter, Chapter 6.

Chapter 6

Voltage and temperature induced phase change in Giant Unilamellar Vesicles

6.1	Introduction	120
6.2	Fabrication of the Giant Unilamellar Vesicles: the electroformation	120
6.3	Imaging method	122
6.4	Mapping the orientation of the BODIPY in the bilayer: an experimental approach	122
6.4.1	Fluorescence anisotropy principle	123
6.4.2	Fluorescence anisotropy experimental results on a GUV	124
6.5	Temperature and voltage dependent viscosity of the bilayer from FLIM experiments on GUV	124
6.5.1	Method to apply a transmembrane voltage and temperature on the GUV	127
6.5.2	FLIM results	128
6.6	Conclusion	135

6.1 Introduction

The gel/liquid phase change of lipid bilayers occurs at a temperature that depends on the lipid structure [146]. This chapter addresses the issue of voltage-induced phase transitions of the bilayer. Such effect of the voltage on a bilayer could explain the thermal behaviour observed on axons [106, 114, 67, 107, 164]. It has been observed that the action potential induces a release of heat followed by a cooling. The action potential is a transmembrane voltage and if that induces a phase transition of the bilayer, heat would be released in the environment. When the voltage becomes zero again, the membrane reverses phase and absorb heat.

The first step in demonstrating this is to prove that an electric field can change the phase of the bilayer. This chapter presents a measure of the viscosity of a lipid bilayer as function of the temperature and the voltage to detect its phase. The systems chosen to perform such experiments are Giant Unilamellar Vesicles (GUV). Like all vesicles, they are stable lipid bilayer systems in water. Vesicles formed artificially have a typical diameter smaller than 100 μm [10, 13]. They can be as large as a few hundreds of nanometers in the case of Large Unilamellar Vesicles (LUV) [183]. GUV are large vesicles of tens of μm and thus the lipid bilayer can clearly be seen in optical microscopy. They are extensively used as cell membrane models [28, 5, 172, 108]. Their large size is convenient to visualize the bilayer and study the phase separation of lipids [178, 144]. The diffusion of proteins in the GUV's membrane can be tracked [85, 77]. The effect of high frequency AC electric fields as also been studied and can change the shape of the vesicles [109, 36, 35]. The first part of this chapter presents the method to synthesise the GUV called the electroformation [4]. This GUV embed the same BODIPY as in Chapter 5. Then, two experiments conducted on the formed GUV are presented:

- an investigation on the position of the BODIPY in the bilayer.
- FLIM measurements as function of the temperature and the voltage applied on the GUV.

6.2 Fabrication of the Giant Unilamellar Vesicles: the electroformation

Giant Unilamellar Vesicles are synthesised using electroformation [4] with the procedure developed by Mauroy [109]. The principle is to deposit the lipids at the bottom of a recipient filled with water. A voltage is then applied on this lipid sediment for several hours to form the GUV. This is done in a recipient formed of two superposed glass slides separated by a seal. These elements are depicted on Figure 6.1. Two recipients are formed at once as the seal is drilled by two holes.

The material needed for the electroformation procedure is:

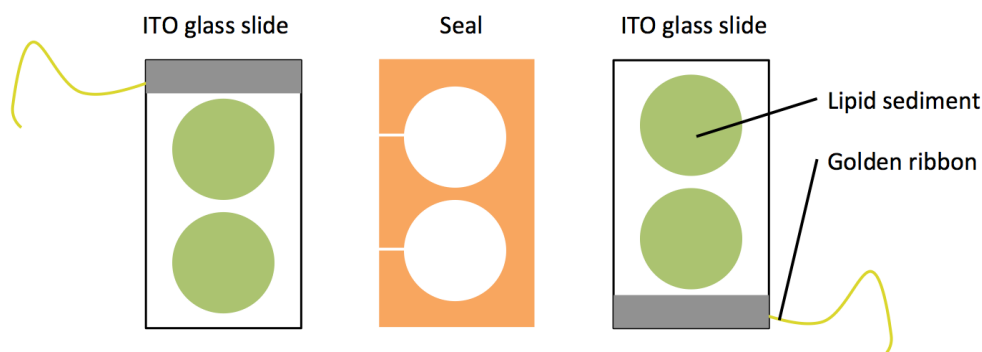


Figure 6.1: *The different parts of the electroformation system. It is formed by superposing the two ITO glass slices separated by the seal. The lipids are deposited on the ITO surface (green circles) and must correspond with the holes in the seal. An electrode made of copper ribbon is then taped on each of the ITO surface.*

- two glass slides with one face covered with Indium Tin Oxide (ITO glass).
- a silicone seal thick of 3 mm.
- lipids (powder or dilute in chloroform).
- chloroform.
- the same fluorescent BODIPY as in Chapter 5.
- copper ribbons to make electrodes on the ITO surface.
- Milli-Q water concentrated at 240 mmol.L^{-1} of sucrose.
- a generator to apply sinusoidal and square voltage.

The first step is to add the electric contacts on the ITO glass slides by taping copper ribbons on the conductive surface. The second step is to prepare the lipid solution: chloroform solution concentrated at $500 \mu\text{g.mL}^{-1}$ of DPPC lipids. The same BODIPY in the same proportion as in Chapter 5 (1:800) is added in this solution. $15 \mu\text{L}$ of this solution is then homogeneously deposited on the glass covered with Indium Tin Oxide (ITO) with a Hamilton syringe (the solution is deposited on the conductive face). Circular patterns are used to form a sediment that follows the shape of the holes in the seal (Figure 6.1 in green). To remove the chloroform and prevent the lipid to oxidise, the two slides are then placed under vacuum for about one hour.

The next step is to superpose the two slides and keep them separated by the seal. The sediment of lipid must be in the holes of the seal and inside the formed recipient. The seal is open on one side to introduce the syringe and fill the recipient with the sucrose Milli-Q water.

Finally, the recipient is heated up to 50°C (above 41°C , the transition temperature of DPPC lipid bilayer). A ramp of sinusoidal voltage at 8 Hz is then applied between the electrodes of this system. This voltage starts at 50 mV peak to peak and is increased up to 2450 mV by adding 200 mV every 5 minutes. The system is maintained under these conditions for one night (minimum

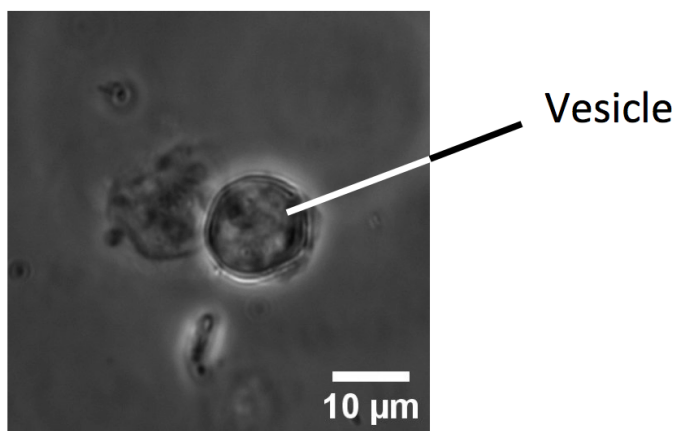


Figure 6.2: Phase contrast image of a GUV (filled with the 240 mmol.L^{-1} sucrose solution) in water concentrated at 260 mmol.L^{-1} of glucose, 1 mmol.L^{-1} of Hepes .

4 hours).

To prevent the water inside the recipients from drying, the seal (Figure 6.1) must be carefully closed after the water is injected. The holes in the seal are made only by cutting the seal which allow to close the recipient almost completely and hermetically. The chamber was kept closed by putting a weight on the glass to prevent it to open during the electroformation. At the end of the formation, a square 2450 mV voltage at 4 THz is applied for 1 hour to take the vesicles down. The inner solution can be recovered with the Hamilton syringe. The vesicles formed this way are more stable than to the suspended bilayer and can be conserved in a fridge for days. There is no organic solvent in the final form of the sample: the lipid bilayers are pure.

6.3 Imaging method

The vesicles are diluted in another solution: water concentrated at 260 mmol.L^{-1} of glucose and 1 mmol.L^{-1} of Hepes as recommended by Mauroy [109]. The vesicles are observed using phase contrast imaging in a chamber made with plain glass slides separated by a silicone seal. Figure 6.2 shows a vesicle in phase contrast image.

6.4 Mapping the orientation of the BODIPY in the bilayer: an experimental approach

In Chapter 5, the FLIM measurements revealed a bi-exponential decay of the fluorescence of the BODIPY. GUV can be used to check that this is explained by the presence of two populations of BODIPY located differently in the bilayer.

GUV being at least 10 μm thick, their membrane can be seen in fluorescence microscopy. This can be exploited to precise the orientation of the BODIPY by polarising the excitation light and measure the fluorescence anisotropy.

The fluorescent molecules aligned with this polarisation will absorb and thus re-emit more. As a result, a correlation between the location of the fluorophore and its orientation can be extracted. The GUV being a sphere, its membrane is seen under different orientations. Thus, the intensity contrast on the GUV edge is correlated to the orientation of the BODIPY regarding the bilayer.

First, the principle of fluorescence anisotropy is detailed, followed by static measurements on the GUV. The last part presents a FLIM anisotropy measurement on a GUV.

6.4.1 Fluorescence anisotropy principle

A fluorescent molecule can absorb a photon only if the electric field of the light is oriented in a specific direction [92]. The emitted photon's polarisation will also have a specific orientation. This orientation is defined by the transition dipole of the molecule. The probability of absorption or emission is proportional to $\cos^2 \Phi$ where Φ is the angle between the polarisation and the transition dipole of the molecule. This phenomenon is called photoselection.

The fluorescence anisotropy, r , is defined as the difference between the emitted intensity polarised as the exciting light, I_{\parallel} , and the emitted intensity polarised perpendicularly, I_{\perp} , divided by the total intensity, I_{tot} : The fluorescence anisotropy r is defined by:

$$r = \frac{I_{\parallel} - I_{\perp}}{I_{\text{tot}}} = \frac{I_{\parallel} - I_{\perp}}{I_{\parallel} + 2I_{\perp}}. \quad (6.1)$$

To realise such measurement, the incident and emitted light are polarised either vertically (V) or horizontally (H). The measured intensities will thus be noted I_{XY} with X= V or H, the polarisation of the incident light and Y = V or H, for the emitted light. As a results,

$$r = \frac{I_{VV} - I_{VH}}{I_{VV} + 2I_{VH}}. \quad (6.2)$$

Detector used to measure the intensity can introduce a bias by having different sensitivities for different polarisations. It is corrected by a factor, G , defined by the ration of the sensitivity to vertical polarisation and the one of horizontal polarisation. Thus,

$$r = \frac{I_{VV} - GI_{VH}}{I_{VV} + 2GI_{VH}}. \quad (6.3)$$

This anisotropy is related to the orientation of the fluorophore population by [92]:

$$r = \frac{3\langle \cos^2 \theta \rangle - 1}{2}, \quad (6.4)$$

with the probability density

$$p(\theta) = \sin \theta \cos^2 \theta, \quad (6.5)$$

where θ is the angle between the transition dipole and the vertical polarisation. If the distribution of the fluorophore is random, $r = 0.4$. If all the transition moments are aligned with the polarisation, $\theta = 0$, and $r=1$. These derivations are made under the assumption that the transition dipole of the absorption and emission are collinear. In most cases, there is an angle α between those two transition dipoles. The fluorescence anisotropy finally becomes:

$$r = \frac{3\langle \cos^2 \theta \rangle - 1}{2} \frac{3 \cos^2 \alpha - 1}{2}. \quad (6.6)$$

6.4.2 Fluorescence anisotropy experimental results on a GUV

The fluorescence microscopy set up is the same as in Chapter 5. The signal on the GUV bleaches as there is no BODIPY reservoir in this system. The absorption transition dipole is indicated on Figure 6.5 [80].

Figure 6.3 shows the four measurements with different polarisations used to measure the fluorescence anisotropy of the system. The photoselection on these images reveals the orientation of the BODIPY in the bilayer. On the HH image, the right and left sides of the GUV are extinguished. The VV image shows the opposite: the left and right sides bright while the upper and lower edges of the GUV are extinguished. The VH and HV images however are alike. As a result, the transition dipoles are horizontal in the top and bottom edges and vertical on the sides' edges: the BODIPY lie parallel to the membrane plane. This claim is compatible with the position dependent fluorescence anisotropy computed using eq. 6.3 and Figure 6.3. This calculation is represented on Figure 6.4. The anisotropy in the central part on the GUV (green) is 0.2. It reaches 0.6 on the sides of the GUV and -0.3 on the top. Assuming that the transition dipoles are in the plane of the bilayer on the top of the GUV ($\theta = 90^\circ$), eq. 6.6 gives $\cos^2 \alpha \approx 0.73$. Injected into the same equation on the sides of the GUV ($\theta = 0^\circ$), this gives $r = 0.6$ which is consistent with the measured fluorescence anisotropy. The BODIPY are lying parallel to the membrane. Kuimova et al.[183] stated that 10-15 % of the BODIPY lie on the membrane surface. As the majority is still in a parallel direction, the other 85-90 % are located in between the layers of lipids.

6.5 Temperature and voltage dependent viscosity of the bilayer from FLIM experiments on GUV

To measure the voltage-induced phase transition of the lipid bilayer with the GUV, the viscosity of the GUV will be measured as function of the voltage on the membrane (transmembrane voltage) through the fluorescence lifetime of an

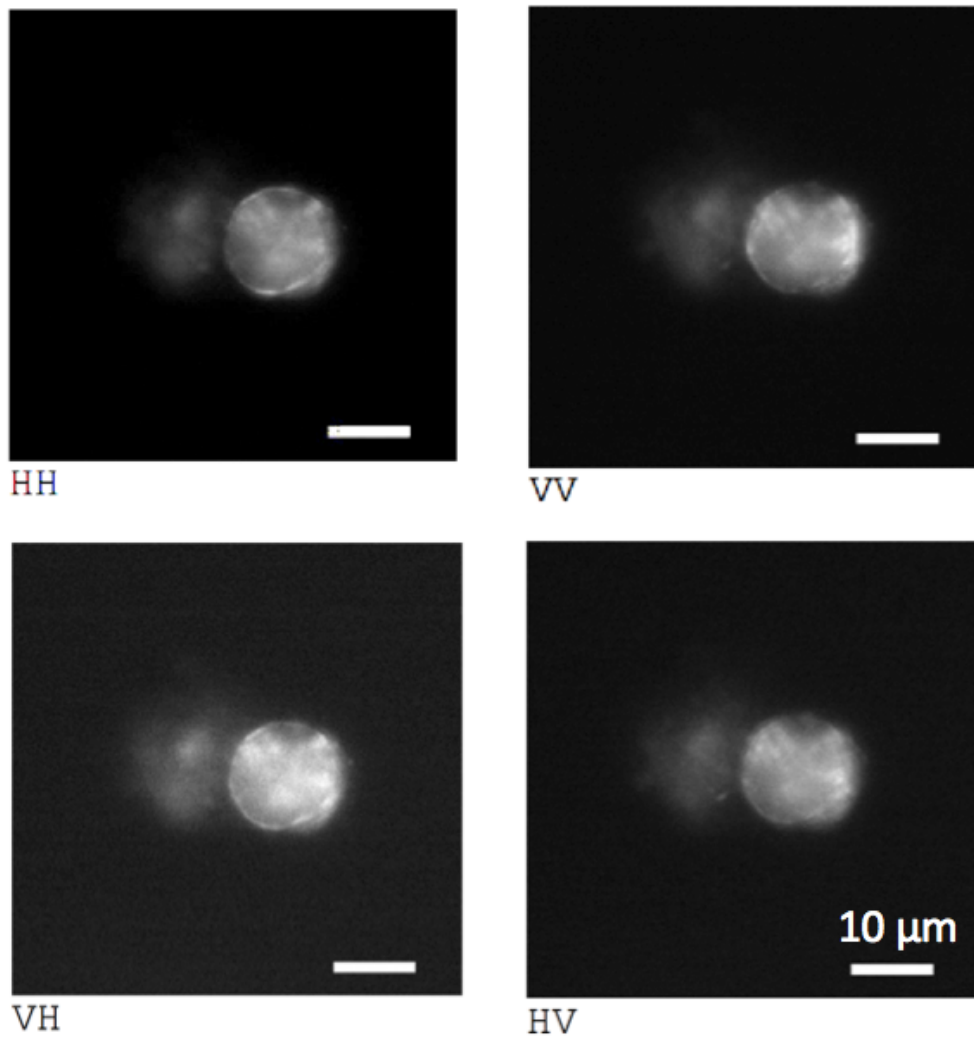


Figure 6.3: *The fluorescence of the GUV depends on the polarisation of the laser (first letter, H for horizontal and V for vertical). The second letter is the polarisation of the emitted light received by the detector. The most intense areas on the image HH are located at the upper and lower part of the GUV while in the VV image, they are on the left and on the right. This indicates that the BODIPY is mostly oriented in the plane of the bilayer. The anisotropy can be computed from these images and is represented on Figure 6.4.*

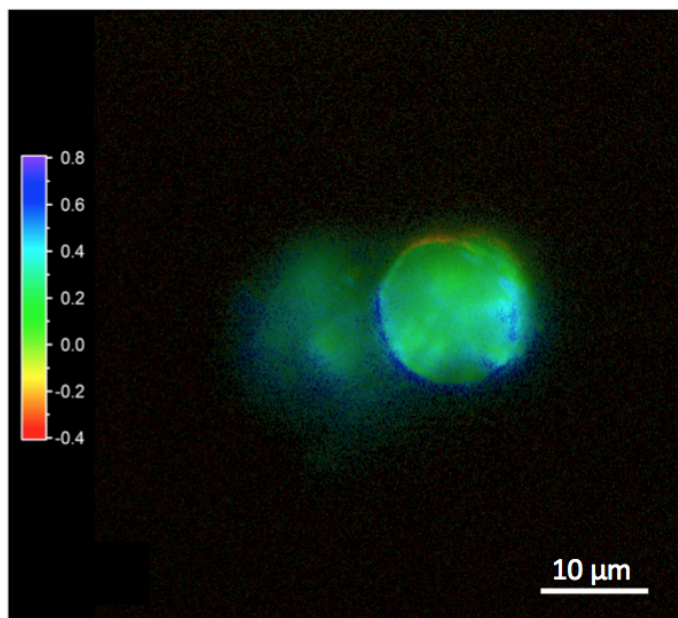


Figure 6.4: Fluorescence anisotropy on a GUV computed with eq. 6.3. The anisotropy in the central part on the GUV (green) is 0.2. It reaches 0.6 on the sides of the GUV and -0.3 on the top. These measurements are consistent with the transition dipoles of the BODIPY being parallel to the plane of the bilayer.

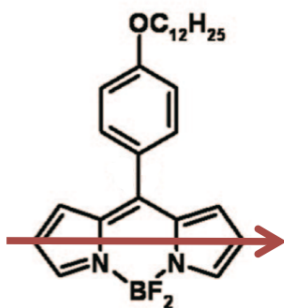


Figure 6.5: BODIPY used as fluorescent molecule. The red arrow indicates the transition dipole [80].

embedded BODIPY. In liquid phase, the viscosity is smaller than in the gel phase. The fluorescence lifetime of the fluorophore is thus smaller in the liquid phase as seen in Chapter 5.

First, the method to apply a transmembrane voltage on the GUV without the possibility to place electrodes on both sides of the lipid bilayer is detailed. The second part here focuses on the results of FLIM measurements on a GUV. This is done at different transmembrane voltages and at 30°C, 35°C and 44°C.

6.5.1 Method to apply a transmembrane voltage and temperature on the GUV

Electrodes cannot be placed inside the vesicle but transmembrane voltages can still be applied [109, 36, 35]. A GUV in water under an electric field accumulates charges on its surface and can be assimilated to an electric capacitor. These charges create in a transmembrane potential. The GUV can be modelled as a hollow dielectric sphere subjected to uniform field E_0 (Figure 6.6). A square field being applied on the GUV, the transmembrane potential ΔV at position (r, θ) is given by [82]:

$$\Delta V = 1.5r \cos \theta E_0 (1 - \exp^{-\frac{t}{\tau}}), \quad (6.7)$$

with t is the duration of the impulsion of the square field and τ is the charging time of this capacitor. τ depends on the geometry and the electric conductances inside (λ_1) and outside (λ_2) the sphere [82]:

$$\tau = \frac{C_m r (\lambda_2 + 2\lambda_1)}{2\lambda_1 \lambda_2}. \quad (6.8)$$

Here, $\lambda_2 = 85 \mu\text{S}\cdot\text{cm}^{-1}$, $\lambda_1 = 17 \mu\text{S}\cdot\text{cm}^{-1}$ and $C_m = 0.01 \text{ F}\cdot\text{m}^{-2}$ (as calculated in Chapter 4 and presented on Figure 4.5). As a result, $\tau \approx 82 \mu\text{s}$ for a vesicle of 40 μm of diameter.

In the experiments, the voltage was applied in a direction parallel to the observation plane. The vesicles were deposited between the gold electrodes of a chip depicted on Figure 6.7. The voltage applied on the vesicle is a square voltage at 50 kHz and all mentions of the voltage values in this part are the peak-to-peak voltage applied on the electrodes. The temperature is applied with a hot plate in contact with the sample. It is then measured with a thermocouple in contact with the chip. The measurements presented here are performed on only one vesicle. Figure 6.8 presents a phase contrast image and a fluorescent image of this GUV. The diameter of this GUV is 31 μm and it is between two electrodes separated by 300 μm . The transmembrane voltage ΔV applied on this GUV as function of the voltage on the electrodes U can be computed using Eq. 6.7:

$$\Delta V \approx 0.055U \cos \theta. \quad (6.9)$$

It has been showed that when the transmembrane potential is higher than a threshold, the membrane becomes permeable and the model used here to

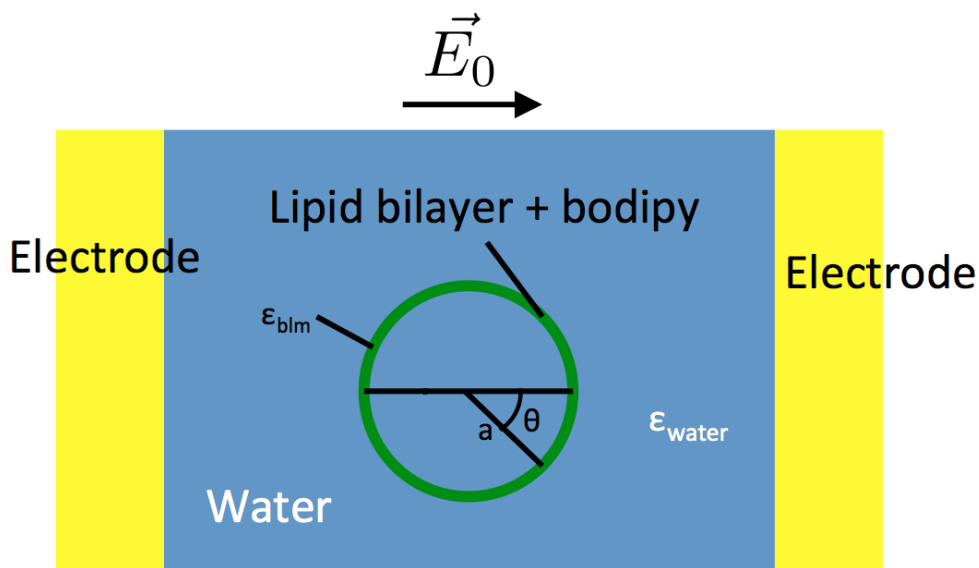


Figure 6.6: Sketch of a GUV of radius a in water between two electrodes. When a voltage is applied between the electrode, and electric field E_0 is created in the water and is applied on the GUV.

compute the transmembrane voltage has to be modified [109]. The threshold for DPPC lipid bilayer is 210-225 mV [165, 132]. In the following experiments, the measurements are done at 30°C, 35°C and 44°C. The inter-electrode voltages vary from 0 V to 8 V peak to peak.

6.5.2 FLIM results

The fluorescence decay observed is bi-exponential like in Chapter 5. It is fitted using the equation:

$$Ae^{-\frac{t}{\tau_1}} + Be^{-\frac{t}{\tau_2}}. \quad (6.10)$$

The fitting parameters are gathered in Table 6.1 and reveal that the two lifetimes have comparable statistical weight. The smallest lifetimes are about 1.7 ns (which corresponds to 120 cP). The largest lifetimes are about 4.5 ns (about 1200 cP). In the following, the pondered averaged lifetimes is considered and they are gathered in Figure 6.9.

These data validate that when the temperature increases, the fluorescence lifetime of the BODIPY in the bilayer drops from 4.15 ns at 30°C and 35°C with 0 V to 3.8 ns. The same effect is observed here when the voltage increases as the lifetime of the GUV at 30°C drops from 4.15 ns with no field to 3.65 ns with 8 V. At 35°C, the same dependence is observed (4.15 ns with no field and 3.7 ns with 8 V).

Using the calibration from Figure 5.4, the fluorescence lifetime from Figure 6.10 and eq. 6.9, the viscosity can be computed as a function of the transmembrane

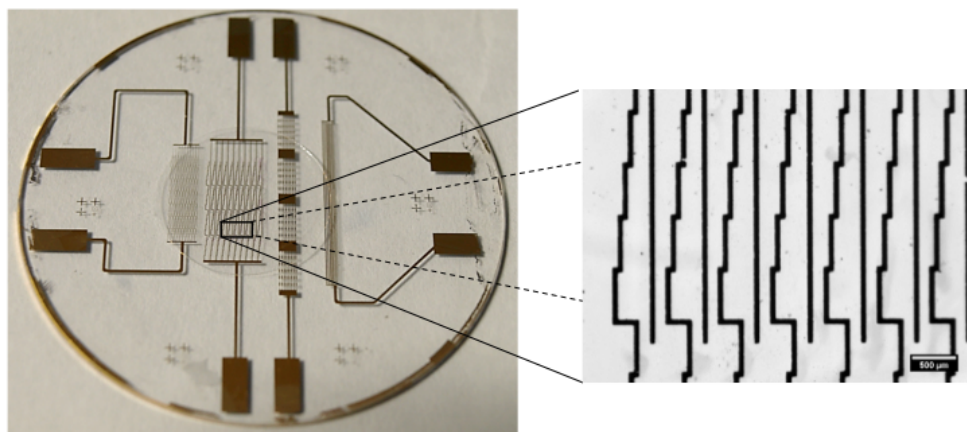


Figure 6.7: Chip to apply voltage on the GUV (right) and close-up on the region used to hold the GUV. The pattern on this chip is in gold and the GUV are put in between the electrodes. The electrodes on the pattern are not always separated by the same distance which allows to have different electric field with the same voltage.

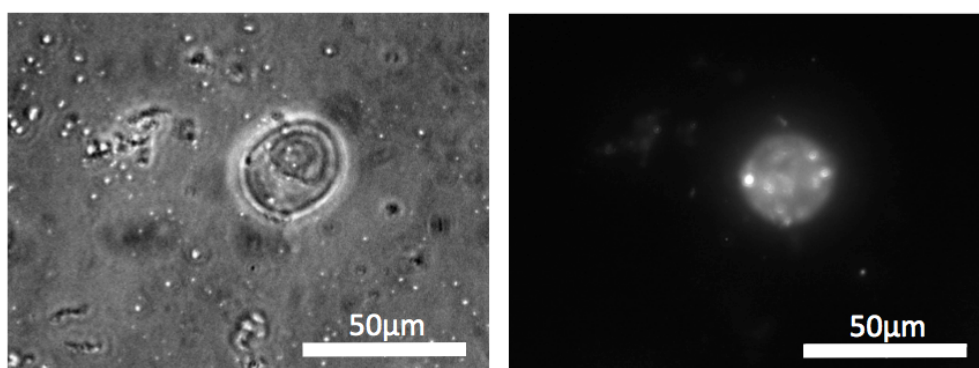


Figure 6.8: Phase contrast image (right) and fluorescence image (left) of the GUV. It is in a 260 mmol.L^{-1} glucose solvent with 1 mmol.L^{-1} of Hepes and is filled with the 240 mmol.L^{-1} sucrose solution. It is on a glass slide between two gold electrodes separated by $300 \mu\text{m}$.

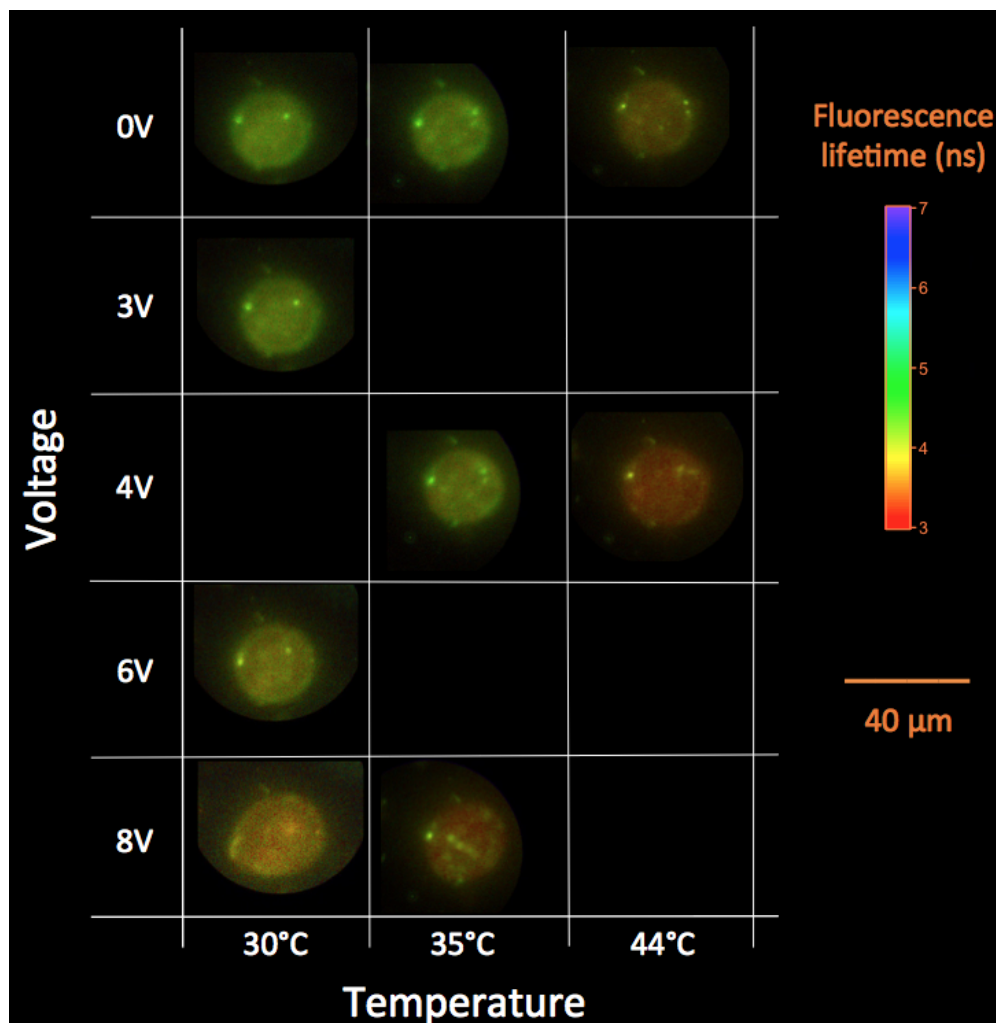


Figure 6.9: FLIM images of a GUV at different temperatures and voltages. The voltage indicated here is the peak to peak voltage applied at the contact of the chip. The electrodes are separated by 300 μm. When the temperature increases, the fluorescence lifetime decreases and the same effect is observed when the voltage increases.

Temperature	Peak to peak voltage	A	τ_1	B	τ_2
30°C	0 V	3551.28	1.72014	6274.97	4.65224
35°C	0 V	3639.58	1.78713	5790.07	4.69298
44°C	0 V	4822.38	1.81982	5452.71	4.52057
30°C	3 V	3674.42	1.60184	6194.65	4.61938
35°C	4 V	4594.06	1.74951	6446.38	4.62137
44°C	4 V	7368.93	1.70763	6811.91	4.28419
30°C	6 V	4061.63	1.39409	5586.07	4.47237
30°C	8 V	5057.46	1.26364	4473.4	4.42373
35°C	8 V	6450.91	1.68979	5810.19	4.52032

Table 6.1: *Fitting parameters of the fluorescence decay on the GUV.*

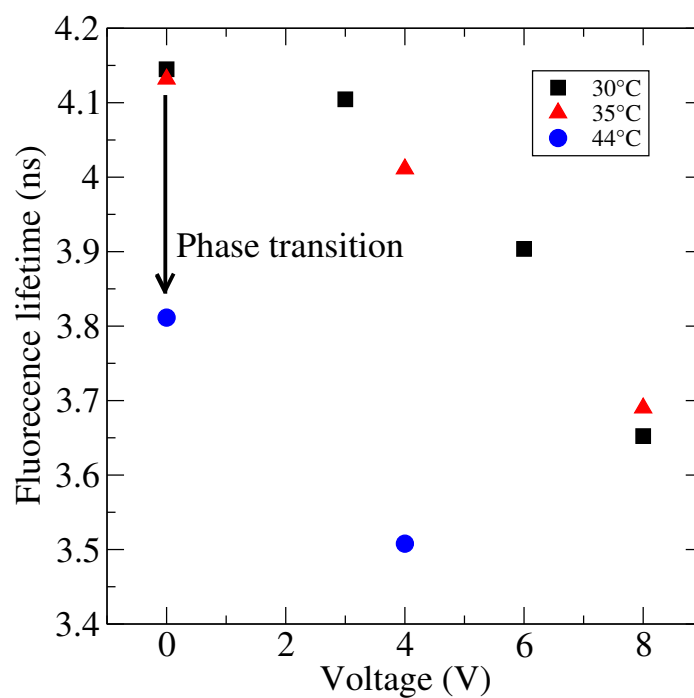


Figure 6.10: *Average fluorescence lifetime as function of the peak-to-peak voltage on the electrodes. At 30°C, 35°C and 44°C, the fluorescence lifetime decreases with the voltage applied.*

voltage (Figure 6.11). The DPPC lipid bilayer phase transition temperature is tabulated at 41°C in the literature. This Figure thus reveals that the viscosity in the gel phase (30°C and 35°C with 0 V) is 930 cP and drops to 790 cP in the liquid phase (at 44°C with 0 V). This means a decrease of 15 % on 9°C. However, this viscosity is still very large for a liquid phase viscosity known to be around 90 cP [60], thus the phase transition might not be totally achieved. The transmembrane voltage also decreases the viscosity of the GUV and the effect is seen to depend on the phase, for instance:

- at 35°C (gel phase), a 50 mV transmembrane voltage induces a 6 % decrease of the viscosity.
- at 44°C (fluid phase), 50 mV induces a 15 % decrease of the viscosity.

However, at 30°C and 35°C, a 140 mV transmembrane voltage has the same effect on the viscosity (22-23 % drop). The viscosity's dependence on the transmembrane voltage is not linear, however, the electric energy added to the system is expressed by $E = CU^2$. The viscosity as function of this energy can be plotted (Figure 6.12). This reveals that the viscosity depends linearly of this energy in the gel phase. To compare the effect of the temperature and the voltage, the energy difference between the gel phase and the fluid phase is $5 \cdot 10^{-20}$ J per lipid [60]. Thus the effect of the electrical energy here is very small compare phase energy difference but only about $4 \cdot 10^{-22}$ J per lipid (140 mV) decreases the viscosity by 23 % at 30°C to a value smaller than the value at 44°C with no field on.

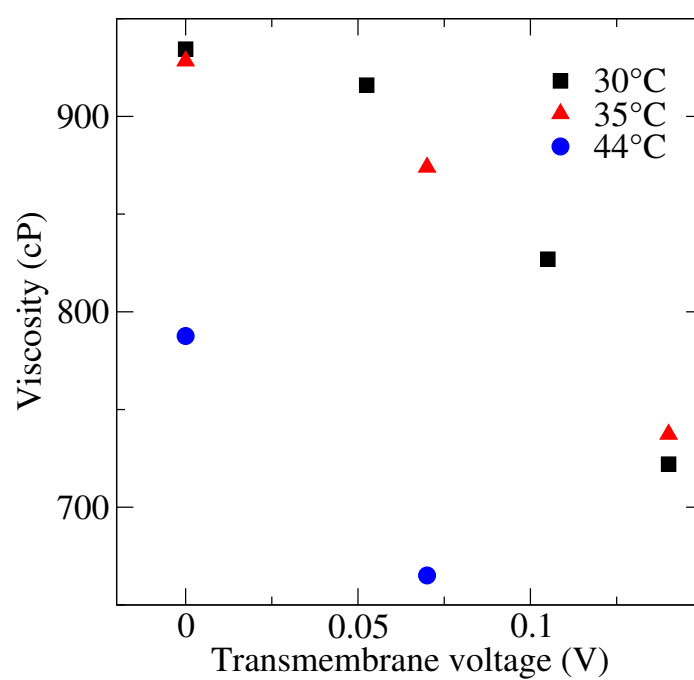


Figure 6.11: Viscosity as function of the transmembrane voltage on the *GUV* at 30°C, 35°C and 44°C calculated from the fluorescence lifetime (Figure 6.10) using the calibration (Figure 5.4) and eq. 6.9.

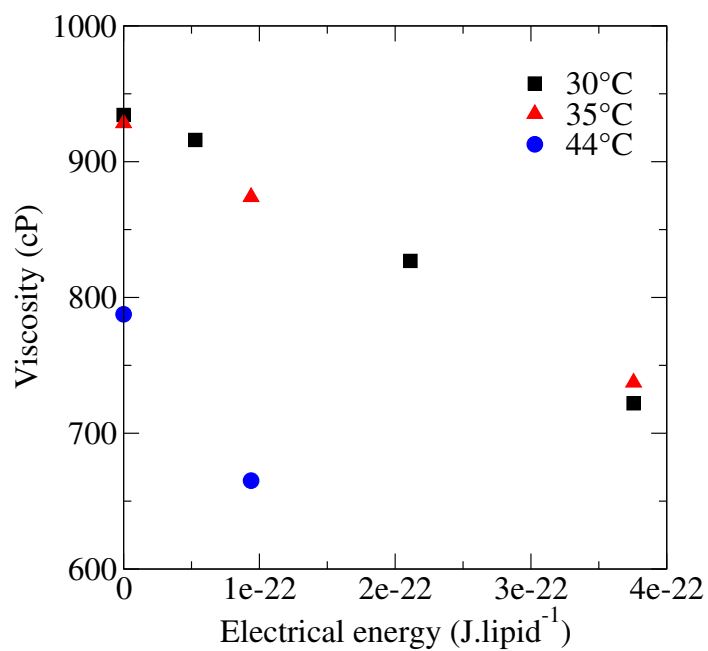


Figure 6.12: Viscosity as function of the electrical energy on the bilayer. In the gel phase ($T < 41^\circ\text{C}$), the viscosity depends linearly on the electrical energy. For comparison, the energy difference between the gel and liquid phase of the bilayer is about $5 \cdot 10^{-20}$ J per lipid.

6.6 Conclusion

To conclusion, the voltage-induced phase transition has been investigated on Giant Unilamellar Vesicles by FLIM measurements. The method is validated by the recovering of a phase transition temperature compatible with the 41°C tabulated in the literature. Fluorescence anisotropy and photoselection experiments exploiting the spherical geometry of the vesicles demonstrated that the BODIPY embedded in the bilayer lie oriented horizontally with regard to the bilayer. The fluorescence lifetime of the embedded fluorophore in the bilayer has been measured with transmembrane voltage from 0 to 140 mV, those measurements reveal the voltage can decrease the viscosity of the bilayer by a 23 % while heating the system from 35°C to 44°C decreases its viscosity by only 15 %. The structure of the membrane is thus altered but to understand the change of structure, further investigations are required. Molecular Dynamics have proven to be able to reproduce structural changes of bilayer in the case of electroporation [127, 155, 151] and could be used to investigate the effect of a smaller electric field as the one applied here and even compute the viscosity variations.

Conclusion

The introduction of nanotechnologies in biology promises more localized and effective medical applications with fewer side effects and that might cure lethal diseases. A large part of these applications take root in the thermal transfer at the nanoscale. However, despite the extensive studies performed worldwide, most of the heat relaxation properties of nanoscale biological materials remain incompletely addressed. There are two types of nanoscale systems of biological interests:

- nanoscale objects designed to interact with biological materials.
- biological materials themselves.

In this thesis, the case of a nanoparticle designed for local plasmonic hyperthermia has been addressed from a numerical point of view. This object is among the best candidates for local hyperthermia applications. A microscopic analysis of the heat transfer at the solid/liquid interface has been proposed in this work with a vibrational analysis and transmission calculations concluding to that polymer grafting reduces the overall solid/liquid resistance by creating additional relaxation channels. The largest part of the work presented here concerns lipid bilayers that are the main constituent of cell membranes. Such material is thus widely studied but heat relaxation problems remain un-addressed such as the voltage-induced phase transition that has been investigated here. A numerical study of the electrical capacity and infrared absorption of this system has been proposed here showing that the absorption spectra do not depend on the bilayer structure but the localisation of the absorption is strongly impacted by the phase: it occurs mostly in the heads of the lipids in the a gel phase, while in a liquid phase, the absorption is more homogeneous. To show a voltage-induced phase transition, fluorescence lifetime imaging microscopy experiments have been conducted on two lipid systems: suspended lipid bilayers and giant unilamellar vesicles. In the first case, the experimental results show that the suspended bilayer's viscosity increases with the temperature, and specially at the phase transition temperature at about 310 K. This unexpected result can be explained by solvent molecules localised in the bilayer being shooved due to the increase of the interdigitation with the temperature. This hypothesis was assessed using Molecular Dynamics simulations. The numerical model allows to compute the variation of the concentration of the solvent in the bilayer and the results are in agreement with the experimental measurements. The

suites found for the investigation of the voltage-induced phase transition are giant unilamellar vesicles. The spherical geometry of this system allows performing fluorescence anisotropy measurements that demonstrated that the fluorophore embedded in the membrane lie horizontally oriented with regard to the bilayer. The measure of the viscosity as function of the temperature and voltage were performed using fluorescence lifetime imaging microscopy. A variation of the viscosity by 15 % is found at the tabulated transition temperature of the bilayer and an even larger variation of 23 % is found with 140 mV of transmembrane voltage. However a sharp variation of the viscosity with the voltage is not found thus the measures reveal a structure change in the bilayer but not a first order phase transition and further calculations and experiments are required to conclude.

The work that have been presented in this thesis reveals the complexity of thermal relaxation in biological nanosystems that involves heat conduction, convection, radiation and phase transition at the same time. The complexity of the system studied leads to very unexpected results and the numerical tool was required to understand the measurements. This thesis illustrates the need to make experimental measurements interact with numerical simulations and model in order to address the nanoscale energy transfer problems in biological environments.

Appendix A

An example of non-ergodic system: the 1D harmonic chain

Let us consider a chain of three particles interacting through spring forces as depicted on Figure A.1. With m the masses of the particles, x_1 , x_2 and x_3 their positions, a the equilibrium length of the springs and k the spring stiffness, the atomic motion equations are:

$$m\ddot{x}_1 = k(x_2 - x_1 - a), \quad (\text{A.1})$$

$$m\ddot{x}_2 = -k(x_2 - x_1 - a) + k(x_3 - x_2 - a), \quad (\text{A.2})$$

$$m\ddot{x}_3 = -k(x_3 - x_2 - a). \quad (\text{A.3})$$

By using $u_1 = x_1$ and $u_2 = x_2 - a$ and $u_3 = x_3 - 2a$,

$$m\ddot{u}_1 = k(u_2 - u_1), \quad (\text{A.4})$$

$$m\ddot{u}_2 = -k(u_2 - u_1) + k(u_3 - u_2), \quad (\text{A.5})$$

$$m\ddot{u}_3 = -k(u_3 - u_2). \quad (\text{A.6})$$

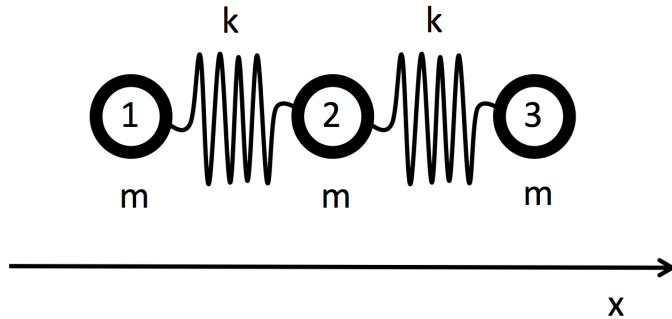


Figure A.1: Coupled spring systems or harmonic polymers are an example of non-ergodic system. It can be shown that they can be trapped in a part of their phase diagram.

Let us define $\omega_0 = \sqrt{\frac{k}{m}}$,

$$\ddot{u}_1 = \omega_0^2(u_2 - u_1), \quad (\text{A.7})$$

$$\ddot{u}_2 = -\omega_0^2(u_2 - u_1) + \omega_0^2(u_3 - u_2), \quad (\text{A.8})$$

$$\ddot{u}_3 = -\omega_0^2(u_3 - u_2). \quad (\text{A.9})$$

Assuming monochromatic wave solutions $u_j = u_j^0 e^{i\omega t}$ and using

$$U = \begin{bmatrix} u_1^0 \\ u_2^0 \\ u_3^0 \end{bmatrix},$$

and

$$M = \begin{bmatrix} \omega_0^2 - \omega^2 & -\omega_0^2 & 0 \\ -\omega_0^2 & 2\omega_0^2 - \omega^2 & -\omega_0^2 \\ 0 & -\omega_0^2 & \omega_0^2 - \omega^2 \end{bmatrix},$$

the resulting equation writes

$$MU = 0. \quad (\text{A.10})$$

This latter equation has non-trivial solutions only if its determinant is zero, that is

$$\det M = \omega^2(\omega^2 - \omega_0^2)(\omega^2 - 3\omega_0^2). \quad (\text{A.11})$$

Therefore there are three frequencies for which it exists non trivial solutions for U, $\omega = 0$, $\omega = \omega_0$ and $\omega = \sqrt{3}\omega_0$. Which leads to the solution vector,

$$\begin{bmatrix} A \\ 0 \\ -A \end{bmatrix},$$

for $\omega = \omega_0$, and

$$\begin{bmatrix} B \\ \frac{B}{2} \\ B \end{bmatrix},$$

for $\omega = \sqrt{3}\omega_0$.

If the system put in one of those eigenstates as a starting condition, it will stay in this mode as it is a solution of its motion equations, but there is a case in which the second atom does not move. Hence it is clear that the system will not explore a domain of its phase space if placed in this mode, no matter how long its evolution. As a conclusion, this system is not ergodic.

Another famous example of non-ergodic system is the Fermi-Pasta-Ulam problem [43], a non linear chain that was proven to be non ergodic because of its dimensionality with important consequences in physical systems [138].

Appendix B

Classical approximation and equipartition theorem

In all the cases addressed in this thesis, we use the classical approximation. In the frame of this approximation, the difference of energy between two consecutive states is small enough that a continuum of states can be considered. Meaning we can write $\prod_i \frac{\int d x_i d y_i d z_i d p_{x_i} d p_{y_i} d p_{z_i}}{(2\pi\hbar)^3}$ instead of a discrete sum. As a result, we are in the conditions of application of the equipartition theorem. This theorem links the temperature to the energy in ergodic systems at equilibrium imposing that each mode carries the same amount of energy, $\frac{1}{2}k_B T$. It can be written as

$$\langle X_i \frac{\partial H}{\partial X_j} \rangle = \delta_{ij} k_B T. \quad (\text{B.1})$$

H refers to the Hamiltonian of the system and X_i is a generalized coordinate. We can straightforwardly prove this relation in the canonical ensemble

$$\begin{aligned} \langle X_i \frac{\partial H}{\partial X_j} \rangle &= \frac{1}{Z} \int X_i \frac{\partial H}{\partial X_j} e^{-\beta H} dX^{6N} \\ &= \frac{-1}{\beta Z} \int X_i \frac{\partial}{\partial X_j} e^{-\beta H} dX^{6N} \\ &= \frac{-1}{\beta Z} \left[\underbrace{\int [X_i e^{-\beta H}]_{X_i=-\infty}^{X_i=+\infty} dX^{6N-1}}_{=0} - \underbrace{\int \frac{\partial X_i}{\partial X_j} e^{-\beta H} dX^{6N}}_{=\delta(i-j)Z} \right] \\ &= \delta_{ij} k_B T. \end{aligned} \quad (\text{B.2})$$

Appendix C

Radial distribution function in diffraction experiments

The radial distribution function is very important because it characterises the microscopic structure of a material but also because it can be measured by diffraction experiments.

In our N particles system, we can define the function $f(r) = \sum_{i=1}^N \delta(r - r_i)$ for any time. All those particles are considered as diffusers that can move. We can rewrite the temporal (or ensemble) average of the diffused radiations intensity $\langle I \rangle$ as function of the Fourier transform of f :

$$\begin{aligned} \langle \tilde{I}(k) \rangle &\propto \langle |\tilde{f}(k)|^2 \rangle \\ &\propto \left\langle \left(\sum_{u=1}^N e^{ikr_u} \right) \left(\sum_{v=1}^N e^{-ikr_v} \right) \right\rangle \\ &\propto \left\langle \sum_{u=1}^N \sum_{v=1}^N e^{-ik(r_v - r_u)} \right\rangle \cong NS(k) \end{aligned} \tag{C.1}$$

(C.2)

We name S the structure factor, we write:

$$\begin{aligned}
S(k) &= \frac{1}{N} \left\langle \sum_{u=1}^N \sum_{v=1}^N e^{-ik(r_v - r_u)} \right\rangle \\
&= 1 + \frac{1}{N} \left\langle \sum_{u=1}^N \sum_{v=1, v \neq u}^N e^{-ik(r_v - r_u)} \right\rangle \\
&= 1 + \frac{1}{N} \left\langle \int e^{-ikr} \sum_{u=1}^N \sum_{v=1, v \neq u}^N \delta(r - (r_v - r_u)) d^3r \right\rangle \\
&= 1 + \frac{1}{N} \int e^{-ikr} \left\langle \sum_{u=1}^N \sum_{v=1, v \neq u}^N \delta(r - (r_v - r_u)) \right\rangle d^3r \\
&= 1 + \int e^{-ikr} (N-1) \langle \delta(r - |r_2 - r_1|) \rangle d^3r \\
&= 1 + \int e^{-ikr} \rho^2 g(r) d^3r \\
&= 1 + \rho \tilde{g}(k) \tag{C.3} \\
&\tag{C.4}
\end{aligned}$$

Thus we can measure the Fourier transform of the pair correlation function by diffraction. This method is often used in soft matter. We can show that g can even be linked to the effective two-body force between the nanoparticles by:

$$g(r) = e^{-\frac{E(r)}{k_B T}}. \tag{C.5}$$

Appendix D

Link between susceptibility and fluctuations

In a more general frame, when the system exchanges a work $dW = x dX$, with X a quantity exchanged with an external reservoir, the following additional constraint can be written:

$$\sum_i P_i X_i = \langle X \rangle. \quad (\text{D.1})$$

Thus we have

$$P_i = \frac{e^{-\beta E_i + \beta x X_i}}{Z}, \quad (\text{D.2})$$

with $x = -T \frac{\partial S}{\partial \langle X \rangle}$ and $Z = \sum_i e^{-\beta E_i + \beta x X_i}$. It can also be shown that $\langle X \rangle = \frac{1}{\beta} \frac{\partial \ln Z}{\partial x}$.

If the work $x \cdot \langle X \rangle \ll k_B T$, we can develop Z :

$$\begin{aligned} Z &= \sum_i e^{-\beta E_i + \beta x X_i}, \\ &\approx \sum_i e^{-\beta E_i} \left[1 + \beta x X_i + \frac{1}{2} (\beta x X_i)^2 \right], \\ &\approx Z_{x=0} \left[1 + \beta x \langle X \rangle_{x=0} + \frac{1}{2} \beta^2 x^2 \langle X^2 \rangle_{x=0} \right] \end{aligned} \quad (\text{D.3})$$

Thus,

$$\begin{aligned} \langle X \rangle &= \frac{1}{\beta} \frac{\partial \ln Z}{\partial x}, \\ &\approx \frac{1}{\beta} \frac{\partial}{\partial x} \left[1 + \beta x \langle X \rangle_{x=0} + \frac{1}{2} \beta^2 x^2 \langle X^2 \rangle_{x=0} \right], \\ &\approx \frac{\langle X \rangle_{x=0} + \beta x \langle X^2 \rangle_{x=0}}{1 + \beta x \langle X \rangle_{x=0} + \frac{1}{2} \beta^2 x^2 \langle X^2 \rangle_{x=0}}, \end{aligned} \quad (\text{D.4})$$

Thus, at the first order in x ,

$$\begin{aligned}\langle X \rangle &\approx (\langle X \rangle_{x=0} + \beta x \langle X^2 \rangle_{x=0})(1 - \beta x \langle X \rangle) \\ &\approx \langle X \rangle_{x=0} + \beta(\langle X^2 \rangle_{x=0} - \langle X \rangle_{x=0}^2)x\end{aligned}\quad (\text{D.5})$$

Thus the susceptibility χ of the system can be identified as

$$\chi = \beta(\langle X^2 \rangle_{x=0} - \langle X \rangle_{x=0}^2). \quad (\text{D.6})$$

This latter expression introduces the general idea that the response of a system (the susceptibility) can be expressed with the fluctuations of the unperturbed system. For example, if x is an exterior electric field, and the response is $X = p$, the polarisation, then

$$\alpha = \epsilon_0 \chi = \beta(\langle p^2 \rangle_{x=0} - \langle p \rangle_{x=0}^2). \quad (\text{D.7})$$

Appendix E

Thermal conductivity

To describe the thermal transfer in a bulk material, the Fourier law has proven to be particularly robust. It describes the relation between the heat flux \vec{F} , and the temperature gradient $\overrightarrow{\text{grad}} T$ [45] :

$$\vec{J} = -\lambda \overrightarrow{\text{grad}} T. \quad (\text{E.1})$$

This equation defines λ , called the thermal conductivity which is intrinsic to a given material and also depends on the temperature. It reaches 2200 $\text{W.m}^{-1}.\text{K}^{-1}$ in diamond at room temperature, and up to 3320 $\text{W.m}^{-1}.\text{K}^{-1}$ in synthetic doped diamond [176, 90], but the thermal conductivity is much smaller in liquids and polymer material having a value of 0.6 $\text{W.m}^{-1}.\text{K}^{-1}$ in water and even a smaller one in gases and it becomes zero in vacuum.

To understand those differences, it is usually considered that in solids, the thermal conductivity at the microscopic scale is due to :

- the transmission of the atom vibrations, it is the phonon contribution λ_{ph} ,
- the movement of the electrons or holes, it is the electronic contribution λ_e .

The total conductivity is the sum of both contributions, $\lambda = \lambda_{ph} + \lambda_e$. However, in most materials studied in this thesis do not have the crystalline periodicity needed to use the concept of phonon. They still have atomic vibrations being carried over but they are not phonons, they do not exhibit wave properties. Free electrons (or holes) are not considered, but the atoms or even the molecules in gels and liquids can move and transport energy, the mobility of the molecule significantly contributes to the thermal transport and is the origin of convection.

E.1 The Green-Kubo relations

The Green-Kubo formulae express the transport coefficients as a function of flux fluctuations. For instance the Green-Kubo formula for thermal conductivity is:

$$\lambda = \frac{V}{3k_B T^2} \int_0^{+\infty} \langle \vec{J}(0) \vec{J}(t) \rangle dt, \quad (\text{E.2})$$

where \vec{J} is the heat flux expressed as:

$$\vec{J} = \sum_i e_i \vec{v}_i - \frac{1}{2} \sum_i \sum_{j \neq i} (\vec{r}_j - \vec{r}_i) [\vec{F}_{ij} \cdot \vec{v}_i], \quad (\text{E.3})$$

with e_i as the energy of atom i , r_i , its position, v_i , its speed and \vec{F}_{ij} the force applied on atom i by atom j .

This formula for the heat flux can be demonstrated as follow. The heat flux can be written by considering e_i as the energy of atom i and r_i , its position, as [42]

$$\begin{aligned} \vec{J} &= \sum_i \frac{\partial e_i}{\partial t} \vec{r}_i \\ &= \sum_i e_i \vec{v}_i + \sum_i \vec{r}_i \frac{\partial e_i}{\partial t}. \end{aligned}$$

With

$$e_i = \frac{1}{2} m_i \vec{v}_i^2 + \sum_{j \neq i} U_{ij},$$

$U = \frac{1}{2} \sum_i \sum_{j \neq i} U_{ij}$ is the potential energy of atom i , so using the equation of motion with $\vec{F}_i = \sum_{j \neq i} \vec{F}_{ij}$, the force applied on atom i :

$$\begin{aligned} \frac{de_i}{dt} &= m_i \dot{\vec{v}}_i \vec{v}_i + \sum_{j \neq i} \frac{dU_{ij}}{dt}, \\ &= \vec{F}_i \cdot \vec{v}_i + \sum_{j \neq i} \frac{dU_{ij}}{dt}, \\ &= \vec{F}_i \cdot \vec{v}_i + \sum_{j \neq i} \vec{F}_{ij} \cdot (\vec{v}_j - \vec{v}_i) \end{aligned}$$

So

$$\begin{aligned}
\vec{J} &= \sum_i e_i \vec{v}_i + \sum_i \vec{r}_i (\vec{F}_i \cdot \vec{v}_i) + \frac{1}{2} \sum_i \vec{r}_i \sum_{j \neq i} \vec{F}_{ij} \cdot (\vec{v}_j - \vec{v}_i) \\
&= \sum_i e_i \vec{v}_i + \sum_i \vec{r}_i \left(\sum_{j \neq i} \vec{F}_{ij} \cdot \vec{v}_i \right) + \frac{1}{2} \sum_i \vec{r}_i \sum_{j \neq i} \vec{F}_{ij} \cdot (\vec{v}_j - \vec{v}_i) \\
&= \sum_i e_i \vec{v}_i + \sum_i \vec{r}_i \left(\sum_{j \neq i} \vec{F}_{ij} \cdot \vec{v}_i \right) + \frac{1}{2} \sum_i \vec{r}_i \sum_{j \neq i} \vec{F}_{ij} \cdot (\vec{v}_j - \vec{v}_i) \\
&= \sum_i e_i \vec{v}_i + \frac{1}{2} \sum_i \sum_{j \neq i} \vec{r}_i [\vec{F}_{ij} \cdot (\vec{v}_j + \vec{v}_i)] \\
&= \sum_i e_i \vec{v}_i - \frac{1}{4} \sum_i \sum_{j \neq i} (\vec{r}_j - \vec{r}_i) [\vec{F}_{ij} \cdot (\vec{v}_j + \vec{v}_i)] \\
&= \sum_i e_i \vec{v}_i - \frac{1}{2} \sum_i \sum_{j \neq i} (\vec{r}_j - \vec{r}_i) [\vec{F}_{ij} \cdot \vec{v}_i] \\
&= \sum_i e_i \vec{v}_i - \frac{1}{2} \sum_i \sum_{j \neq i} (\vec{r}_j - \vec{r}_i) [\vec{F}_{ij} \cdot \vec{v}_i]
\end{aligned}$$

E.2 Applying the Green-Kubo formula in Molecular Dynamics

The Green-Kubo relation seems rather straightforward to be applied based on Molecular Dynamics outputs. Indeed, it only includes volume, temperature and heat flux, which was presented in Chapter 1 but this calculation is actually quite difficult to handle in practice.

The first difficulty is to compute the heat flux, the formula from Chapter 1 does not include the three-body and four-body interactions [42] and adding those contributions can be a difficult task. The second difficulty is that the simulations have a finite duration, thus the integration can only be done up to a finite time in which the convergence must be reached.

Finally, the ensemble average of the autocorrelations has to be performed. The first point is that in each of the simulations, only a limited part of the phase space accessible to the system is explored. To explore a sufficient region of the phase space, a sufficient number of simulations has to be run and averaged. The number of simulations and their durations depend on the system.

The example of a bulk water system is given here. It consists in 4000 water molecules using the TIP3P model as described above at 310K with a 0.1 fs time step. The simulation is run for 500 steps in NVE, then 20000 steps in NVT, and 50000 steps in NPT. Finally, 150000 time steps in NVE are run to compute the heat flux. Only ten simulations are carried out here and the ten heat flux autocorrelations are computed using the Wiener-Khinchin theorem, as reported in Figure E.1. The average of those autocorrelations is the black

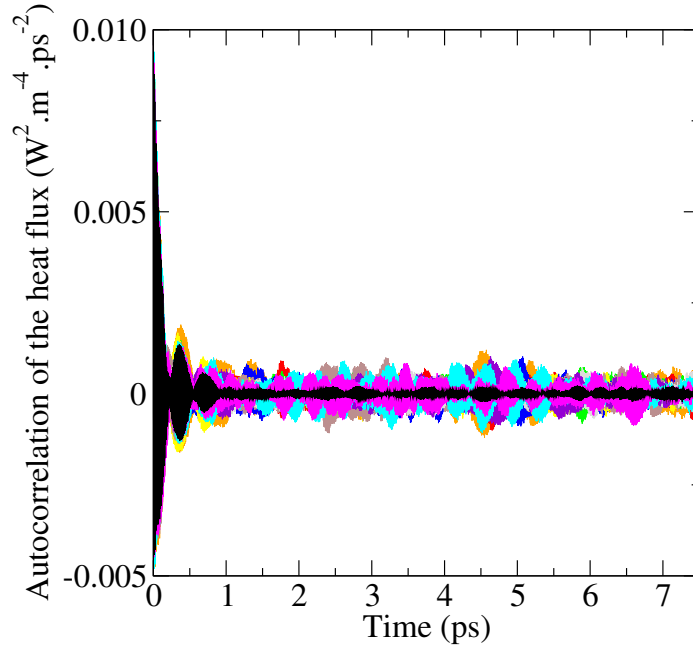


Figure E.1: Autocorrelation functions of the heat flux in water for ten simulations and their average (black line) at 310 K. These curves show that the autocorrelation is converged at a time of about 1 ps.

line. The curves converge after a time of about 1 ps, after which mostly noise occurs. The averaging decreases this noise and the averaged autocorrelation appears as more accurate.

The integral of this autocorrelation, multiplied by the factor $\frac{V}{k_B T^2}$ is then computed for each simulation and showed in Figure E.2. Again the black line is the average of the ten simulations. Almost none of the thermal conductivity integrals converge. Several seem to diverge and others even become negative. However their average is flatter and one can find the value of the thermal conductivity equal to the value of the plateau. The autocorrelation in Figure E.1 reveals that the averaged curve has converged at time 1 ps. Thus the average of the thermal conductivity after this 1 ps is taken and a value of 0.7534 ± 0.0924 $\text{W.m}^{-1}.\text{K}^{-1}$ is obtained. It is possible to increase the number of simulations to reach a better accuracy.

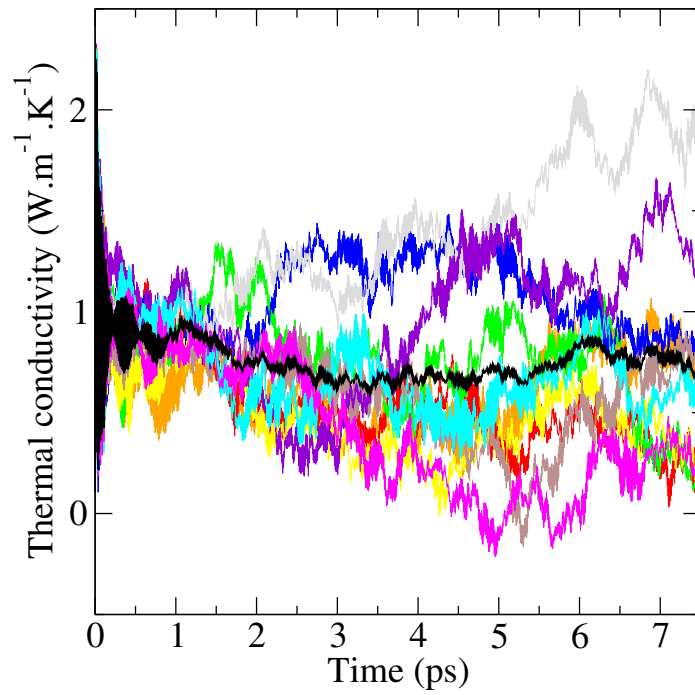


Figure E.2: Thermal conductivity of water for ten simulations and their average (black line). This thermal conductivity is computed as the integral of the autocorrelation of the heat flux. The thermal conductivity integral is supposed to be converged at a time of 1 ps after which variations are assumed to be noise.

Bibliography

- [1] J.L.F. Abascal and C. Vega. A general purpose model for the condensed phases of water: Tip4p/2005. *J. Chem. Phys.*, 123, 2005. p. 21
- [2] Lipika Adhya, Tarunendu Mapder, and Samit Adhya. Role of terminal dipole charges in aggregation of α -helix pair in the voltage gated k^+ channel. *Biochimica et Biophysica Acta*, 1828:845–850, 2013. p. 82
- [3] D. Afanasenkau. *Supported lipid as a biomimetic platform for neuronal cell culture*. Jülich Forschungszentrum, 2013. p. 109
- [4] M.I. Angelova and Dimitrov D.S. Liposome electroformation. *Faraday Discuss Chem. Soc.*, 81:303–312, 1986. p. 120
- [5] M.I. Angelova, R. Mutafchieva, R. Dimova, and B. Tenchov. Shape transformations of giant unilamellar vesicles induced by ethanol and temperature variations. *Colloids Surfaces A: Physicochem. Eng. Aspects*, 149:201–205, 1999. p. 120
- [6] Thad Aweeka. Potential of laser delivery of therapy at the cellular level demonstrated. *MRS Bulletin*, 31(9):653–654, SEP 2006. p. 50
- [7] Teruhiko Baba, Yoshiyuki Toshima, Hiroyuki Minamikawa, Masakatsu Hato, Kyosuke Suzuki, and Naoki Kamo. Formation and characterization of planar lipid bilayer membranes from synthetic phytanyl-chained glycolipids. *Biochimica et Biophysica Acta - Biomembranes*, 1421(1):91–102, 1999. p. 98
- [8] Guillaume Baffou and Herve Rigneault. Femtosecond-pulsed optical heating of gold nanoparticles. *Physical Review B*, 84(3):035415, JUL 21 2011. p. 50
- [9] E. Bamberg and R. Benz. Voltage-Induced Thickness Changes of Lipid Bilayer Membranes and the Effect of an Electric Field on Gram1Cidin a Channel Formation. *Biochimica et Biophysica Acta*, 426:570–580, 1976. p. 79
- [10] Y. Barenholz, D. Gibbes, B. J. Litman, J. Goll, T. E. Thompson, and F. D. Carlson. A simple method for the preparation of homogeneous phospholipid vesicles. *Biochemistry*, 16:2806–2810, 1977. p. 120
- [11] M. I. Baskes. Modified embedded-atom potentials for cubic materials and impurities. *Physical Review B*, 46(5):2727–2742, AUG 1 1992. p. 51
- [12] M.I. Baskes. Modified embedded-atom potentials for cubic materials and impurities. *Physical Review B*, 46:2727–2741, 1991. p. 22

- [13] Shmuel Batzri and Edward D. Korn. Single bilayer liposomes prepared without sonication. *Biochimica et Biophysica Acta*, 298:1015–1019, 1973. p. 120
- [14] R. Benz, O. Fröhlich, P. Läger, and M. Montal. Electrical capacity of black lipid films and of lipid bilayers made from monolayers. *Biochimica et Biophysica Acta*, 394:323–334, 1975. p. 75, 86
- [15] G.N. Berestovsky, M.Z. Gyulkhandanyan, V.G. Ivkov, and V.D. Razhin. Voltage-induced reflectivity relaxation of bilayer lipid membranes: On changes of bilayer thickness. *J. Membrane Biol.*, 43:107–126, 1978. p. 75, 86
- [16] E. Boulais, R. Lachaine, and M. Meunier. Plasma mediated off-resonance plasmonic enhanced ultrafast laser-induced nanocavitation. *Nano Letters*, 12(9):4763–4769, 2012. p. 50
- [17] B.R. Brooks, R. E. Bruccoleri, B.D. Olafson, D.J. States, S. Swaminathan, and M. Karplus. CHARMM: A program for macromolecular energy, minimization, and dynamics calculations. *J. Comp. Chem.*, 4:187–217, 1983. p. 21
- [18] A. S. Bunce and R. C. Hider. THE COMPOSITION OF BLACK LIPID MEMBRANES FORMED FROM EGG-YOLK LECITHIN, CHOLESTEROL AND n-DECANE. *Biochimica et Biophysica Acta*, 363:423–427, 1974. p. 109
- [19] D.A. Case, J.T. Berryman, R.M. Betz, D.S. Cerutti, T.E. Cheatham III, T.A. Darden, R.E. Duke, T.J. Giese, H. Gohlke, A.W. Goetz, N. Homeyer, S. Izadi, P. Janowski, J. Kaus, A. Kovalenko, T.S. Lee, LeGrand S., P. Li, T. Luchko, R. Luo, B. Madej, K.M. Merz, G. Monard, P. Needham, H. Nguyen, H.T. Nguyen, I. Omelyan, A. Onufriev, D.R. Roe, A. Roitberg, R. Salomon-Ferrer, C.L. Simmerling, W. Smith, J. Swails, R.C. Walker, J. Wang, R.M. Wolf, X. Wu, D.M. York, and P.A. Kollman. AMBER 2015, 2015. p. 21
- [20] Neumaier CE, Baio G, S Ferrini, and et al. MR and iron magnetic nanoparticles. Imaging opportunities in preclinical and translational research. *Tumori*, 94, 2008. p. 2
- [21] Y. Chalopin, K. Esfarjani, A. Henry, S. Volz, and G. Chen. Thermal interface conductance in si/ge superlattices by equilibrium molecular dynamics. *Physical Review B*, 85(19):195302, MAY 1 2012. p. 57, 59
- [22] Y. Chalopin and S. Volz. A microscopic formulation of the phonon transmission at the nanoscale. *Applied Physics Letters*, 103(5):051602, JUL 29 2013. p. 59
- [23] Yann Chalopin, Natalio Mingo, Jiankuai Diao, Deepak Srivastava, and Sebastian Volz. Large effects of pressure induced inelastic channels on interface thermal conductance. *Applied Physics Letters*, 101(22):221903, NOV 26 2012. p. 59
- [24] Wei-Hai Chen, Xiao-Ding Xu, Hui-Zhen Jia, Qi Lei, Guo-Feng Luo, Si-Xue Cheng, Ren-Xi Zhuo, and Xian-Zheng Zhang. Therapeutic

- nanomedicine based on dual-intelligent functionalized gold nanoparticles for cancer imaging and therapy in-vivo. *Biomaterials*, 34(34):8798 – 8807, 2013. p. 50
- [25] Yaling Cheng, Richard J. Bushby, Stephen D. Evans, Peter F. Knowles, Robert E. Miles, and Simon D. Ogier. Single ion channel sensitivity in suspended bilayers on micromachined supports. *Langmuir*, 17(4):1240–1242, 2001. p. 98
- [26] K. S. Cole and Curtis H. J. Electric impedance of the squid giant axon during activity. *J. Gen. Physiol.*, 22:649–670, 1939. p. 76, 77
- [27] G. Corongiu and E. Clementi. Molecular-dynamics simulations with a flexible and polarizable potential - density of states for liquid water at different temperatures. *Journal of Chemical Physics*, 98(6):4984–4990, MAR 15 1993. p. 51, 61
- [28] Merkle D., Kahya N., and P. Schwill. Reconstitution and anchoring of cytoskeleton inside giant unilamellar vesicle. *ChemBioChem*, 9:2673–2681, 2008. p. 120
- [29] M. Das, N. Sanson, D. Fava, and E. Kumacheva. Microgels loaded with gold nanorods: Photothermally triggered volume transitions under physiological conditions. *Langmuir*, 23(1):196, JAN 2007. p. 50
- [30] Juan M. del Rio Martinez, Ekaterina Zaitseva, Sönke Petersen, Gerhard Baaken, and Jan C. Behrends. Automated formation of lipid membrane microarrays for ionic single-molecule sensing with protein nanopores. *Small*, pages 119–125, 2014. p. 98
- [31] R. DER. ON THE RETARDED SOLUTION OF THE LIOUVILLE EQUATION AND THE DEFINITION OF ENTROPY IN KINETIC THEORY. *Physica*, 132A:74–93, 1985. p. 10
- [32] Riccardo Di Corato, Ana Espinosa, Lenaic Lartigue, Mickael Tharaud, Sophie Chat, Teresa Pellegrino, Christine Menager, Florence Gazeau, and Claire Wilhelm. Magnetic hyperthermia efficiency in the cellular environment for different nanoparticle designs. *BIOMATERIALS*, 35(24):6400–6411, AUG 2014. p. 2
- [33] J. M. Dickey and Arthur Paskin. Computer simulation of the lattice dynamics of solids. *Physical Review*, 188(3):1407–1418, 1969. p. 42
- [34] James P. Dilger, Stuart G. A. McLaughlin, Thomas J. McIntosh, and Sidney A. Simon. The dielectric constant of phospholipid bilayers and the permeability of membranes to ions. *Science*, 206:1196–1198, 1979. p. 82
- [35] R. Dimova, N. Bezlyepkina, M. D. Jordo, R. L. Knorr, K. A. Riske, M. Staykova, P. M. Vlahovska, T. Yamamoto, P. Yang, and R. Lipowsky. Vesicles in electric fields: Some novel aspects of membrane behavior. *Soft Matter*, 5:3201–3212, 2009. p. 120, 127
- [36] R. Dimova, K. A. Riske, S. Aranda, N. Bezlyepkina, R. L. Knorr, and R. Lipowsky. Giant vesicles in electric fields. *Soft Matter*, 3:817–827, 2007. p. 120, 127

- [37] C. Durand-Gasselin, N. Sanson, and N. Lequeux. Reversible controlled assembly of thermosensitive polymer-coated gold nanoparticles. *Langmuir*, 27(20):12329–12335, OCT 2011. p. 50
- [38] R. Elghanian, J. J. Storhoff, R. C. Mucic, R. L. Letsinger, and C. A. Mirkin. Selective colorimetric detection of polynucleotides based on the distance-dependent optical properties of gold nanoparticles. *Science*, 277(5329):1078–1081, AUG 22 1997. p. 50
- [39] S. Eustis and M. A. El-Sayed. Why gold nanoparticles are more precious than pretty gold: Noble metal surface plasmon resonance and its enhancement of the radiative and nonradiative properties of nanocrystals of different shapes. *Chemical Society Reviews*, 35(3):209–217, 2006. p. 50
- [40] P.P. Ewald. Die berechnung optischer und elektrostatischer gitterpotentiale. *Annalen der Physik*, 3:253–287, 1921. p. 25
- [41] M. Falk and T. A. Ford. Infrared spectrum and structure of liquid water. *Canadian Journal of Chemistry*, 44(14):1699–&, 1966. p. 30, 51
- [42] Zheyong Fan, Luiz Felipe C. Pereira, Hui-Qiongand Wang, Jin-Cheng Zheng, Davide Donadio, and Ari Harju. Force and heat current formulas for many-body potentials in molecular dynamics simulation with applications to thermal conductivity calculations. *Physical Review B*, 92(094301), 2015. p. 148, 149
- [43] E. Fermi, J.R. Pasta, and S.M. Ulam. *Collected Works of Enrico Fermi*, volume 2. University of Chicago Press, 1965. p. 140
- [44] National Center for Biotechnology Information. PubChem Compound Database, 2015. p. 116
- [45] Joseph Fourier. *Théorie analytique de la chaleur*. Firmin Didot Père et Fils, 1822. p. 8, 147
- [46] Stefano Freddi, Laura Sironi, Rocco D’Antuono, Diego Morone, Alice Dona, Elisa Cabrini, Laura D’Alfonso, Maddalena Collini, Piersandro Pallavicini, Giovanni Baldi, Daniela Maggioni, and Giuseppe Chirico. A molecular thermometer for nanoparticles for optical hyperthermia. *Nano Letters*, 13(5):2004–2010, MAY 2013. p. 50
- [47] Xiaohu Gao, Yuanyuan Cui, R.M. Levenson, L. W. K. Chung, and S. Nie. In vivo cancer targeting and imaging with semiconductor quantum dots. *Nature Biotechnology*, 22, 2004. p. 2
- [48] Sergi Garcia-Manyes, Gerard Oncins, and Fausto Sanz. Effect of temperature on the nanomechanics of lipid bilayers studied by force spectroscopy. *Biophysical journal*, 89(6):4261–4274, 2005. p. 98
- [49] J. Gasteiger and M. Marsili. Iterative partial equalization of orbital electronegativity - a rapid access to atomic charges. *Tetrahedron*, 36(22):3219–3228, 1980. p. 21, 23, 24, 52, 53, 83, 113, 114
- [50] R. Gerami and R.F. Bruinsma. Continuum theory of lipid bilayer electrostatics. *The European Physical Journal E*, 30:197–204, 2009. p. 82
- [51] Soham Ghosh, Debabrata Das Gupta, Suman Chakraborty, and Sarit K. Das. Superparamagnetic nanoparticle assisted hyperthermia and cooling

- protocol for optimum damage of internal carcinoma using computational predictive model. *Heat and Mass Transfer*, 49(9):1217–1229, SEP 2013. p. 82
- [52] S.A. Glazier, D.J. Vanderah, A.L. Plant, H. Bayley, G. Valincius, and J.J. Kasianowicz. Reconstitution of the pore-forming toxin alpha-hemolysin in phospholipid/18-octadecyl-1-thiahexa(ethylene oxide) and phospholipid/n-octadecanethiol supported bilayer membranes. *LANGMUIR*, 16:10428–10435, 2000. p. 82
- [53] E. GORTER and F. GRENDDEL. On bimolecular layers of lipoids on the chromocytes of the blood. *Journal of experimental medecine*, 41:439–443, 1925. p. 70
- [54] Alexander O. Govorov and Hugh H. Richardson. Generating heat with metal nanoparticles. *Nano Today*, 2(1):30 – 38, 2007. p. 50
- [55] Pablo Guardia, Riccardo Di Corato, Lenaic Lartigue, Claire Wilhelm, Ana Espinosa, Mar Garcia-Hernandez, Florence Gazeau, Liberato Manna, and Teresa Pellegrino. Water-Soluble Iron Oxide Nanocubes with High Values of Specific Absorption Rate for Cancer Cell Hyperthermia Treatment. *ACS NANO*, 6(4):3080–3091, 2012. p. 2
- [56] Amit Gupta, Ravi S. Kane, and Diana-Andra Borca-Tasciuc. Local temperature measurement in the vicinity of electromagnetically heated magnetite and gold nanoparticles. *Journal of Applied Physics*, 108(6), SEP 15 2010. p. 50
- [57] Zhang H., Yee D., and Wang C. Quantum dots for cancer diagnosis and therapy: biological and clinical perspectives. *Nanomedicine-UK*, 3, 2008. p. 2
- [58] J.F. Hainfeld, D.N. Slatkin, T.M. Focella, and H.M. Smilowitz. Gold nanoparticles: a new X-ray contrast agent. *The British Journal of Radiology*, 79, 2006. p. 2
- [59] W. Hanke and W.-R. Schlue. *Planar Lipid Bilayers*. Harcourt Brace & Company, 1993. p. 109
- [60] Thomas Heimburg. *Thermal Biophysics of Membranes*. Wiley-VCH, 2007. p. 70, 72, 76, 77, 79, 132
- [61] Benjamin A. Heitz, Juhua Xu, Henry K. Hall, Craig Aspinwall, and S Scott Saavedra. Enhanced Long-Term Stability for Single Ion Channel Recordings Using Suspended Poly (lipid) Bilayers. *Journal of the American Chemical Society*, 131:6662–6663, 2009. p. 98
- [62] K. Hichiri, O. Shirai, and K. Kano. Influence of inhalation anesthetics on ion transport across a planar bilayer lipid membrane. *ANALYTICAL SCIENCES*, 28:45–49, 2012. p. 82
- [63] R.W. Hockney and J.W. Eastwood. *Computer simulation using particles*. A. Hilger, 1989. p. 21, 25, 64, 83
- [64] A.L. Hodgkin and A.F. Huxley. A quantitative description of membrane current and its application to conduction and excitation in nerve. *J. Physiol.*, 117:500–544, 1952. p. 76

- [65] W. G. Hoover. Canonical dynamics: Equilibrium phase-space distributions. *Phys. Rev. A*, 31:1695–1697, March 1985. p. 27, 83
- [66] Tristan T. Hormel, Sarah Q. Kurihara, M. Kathleen Brennan, Matthew C. Wozniak, and Parthasarathy Raghuvver. Measuring Lipid Membrane Viscosity Using Rotational and Translational Probe Diffusion. *Physical Review Letters*, 112(188101), 2014. p. 100
- [67] J.V. HOWARTH, R.D. KEYNES, J.M. RITCHIE, and A. VON MURALT. THE HEAT PRODUCTION ASSOCIATED WITH THE PASSAGE OF A SINGLE IMPULSE IN PIKE OLFATORY NERVE FIBRES. *J. Physiol.*, 249:349–368, 1975. p. 98, 120
- [68] Han Hu and Ying Sun. Effect of nanopatterns on kapitzza resistance at a water-gold interface during boiling: A molecular dynamics study. *Journal of Applied Physics*, 112(5):053508, SEP 1 2012. p. 50
- [69] Pierre Hugounenq, Michael Levy, Damien Alloyeau, Lenaic Lartigue, Emmanuelle Dubois, Valerie Cabuil, Christian Ricolleau, Stephane Roux, Claire Wilhelm, Florence Gazeau, and Rana Bazzi. Iron Oxide Monocrystalline Nanoflowers for Highly Efficient Magnetic Hyperthermia. *JOURNAL OF PHYSICAL CHEMISTRY C*, 116(29):15702–15712, 2012. p. 2
- [70] Gregg Jaeger. *The Ehrenfest Classification of Phase Transitions: Introduction and Evolution*. Archive for History of Exact Sciences, 1998. p. 40
- [71] Ghulam Jalani, Sangyeop Lee, Chan Woo Jung, Hongdeok Jang, Jaebum Choo, and Dong Woo Lim. Controlled biohybrid nanoprobe with silver nanoparticle clusters for raman imaging. *Analyst*, 138(17):4756–4759, 2013. p. 50
- [72] K. Jiang, D.A. Smith, and A. Pinchuk. Size-dependent photothermal conversion efficiencies of plasmonically heated gold nanoparticles. *Journal of Physical Chemistry C*, 51(117):27073–27080, 2013. p. 50
- [73] Shan Jiang, Ahmed A. Eltoukhy, Kevin T. Love, Robert Langer, and Daniel G. Anderson. Lipidoid-coated iron oxide nanoparticles for efficient dna and sirna delivery. *Nano Letters*, 13(3):1059–1064, MAR 2013. p. 82
- [74] W. L. Jorgensen, J. Chandrasekhar, J. D. Madura, R. W. Impey, and M. L. Klein. Comparison of simple potential functions for simulating liquid water. *Journal of Chemical Physics*, 79(2):926–935, 1983. p. 21, 83
- [75] W. L. Jorgensen, J. Chandrasekhar, J. D. Madura, R. W. Impey, and M. L. Klein. Comparison of simple potential functions for simulating liquid water. *Journal of Chemical Physics*, 79(2):926–935, 1983. p. 51
- [76] H. Jung, Y. Wong, S. Shin, and K. Kim. Molecular dynamics simulation of benzenethiolate and benzyl mercaptide on au(111). *Langmuir*, 15:1147–1154, 1999. p. 51
- [77] N. Kahya. Protein?protein and protein?lipid interactions in domain-assembly: Lessons from giant unilamellar vesicles. *Biochimica et Biophysica Acta*, 1798:1392?1398, 2010. p. 120
- [78] P.L. Kapitza. The study of heat transfer in helium II. *J. Phys. (USSR)*,

- 4, 1941. p. 35
- [79] Roghayeh Abedi Karjiban, Nurul Syahidah Shaari, Uma Villashini Gunasakaran, and Mahiran Basri. A coarse-grained molecular dynamics study of dlpc, dmpe, dppc and dspc mixtures in aqueous solution. *Journal of Chemistry*, 2013, 2013. p. 90
- [80] J. Karolin, L. B.-A. Lennart B.-A. Johansson, J. F. J Leif Strandberg, and T. Ny. Fluorescence and absorption spectroscopic properties of dipyrrometheneboron difluoride (bodipy) derivatives in liquids, lipid membranes, and proteins. *J. Am. Chem. Soc.*, 116:7801–7806, 1994. p. 124, 126
- [81] J. Katsaras and T. T. Gutberlet. *Lipid bilayer: Structure and Interactions*. Springer, 2001. p. 106, 116
- [82] K. Jr Kinoshita, I Ashikawa, N. Saita, H. Yoshimura, H. Itoh, K. Nagayama, and A. Ikegami. Electroporation of cell membrane visualized under a pulsed-laser fluorescence microscope. *Biophys J.*, 53:1015–1019, 1988. p. 127
- [83] V Kotaidis and A Plech. Cavitation dynamics on the nanoscale. *Applied Physics Letters*, 87(21):213102, 2005. p. 50
- [84] Frank Kreith and D. Yogi Goswami. *The CRC Handbook of Mechanical Engineering*. CRC Press, second edition: 2005. p. 1
- [85] J. Kriegsmann, I. Gregor, I. von der Hocht, J. Klare, M. Engelhard, J. Enderlein, and J. Fitter. Translational diffusion and interaction of a photoreceptor and its cognate transducer observed in giant unilamellar vesicles by using dual-focus fcs. *ChemBioChem*, 10:1823–1829, 2009. p. 120
- [86] Ryogo Kubo, Morikazu Toda, and Natsuki Hashitsume. *Statistical Physics II: Nonequilibrium Statistical Mechanics*. Springer, 1991. p. 33
- [87] Ryogo Kubo, Morikazu Toda, Natsuki Hashitsume, and N. Saito. *Statistical Physics II: Nonequilibrium Statistical Mechanics (Springer Series in Solid-State Sciences, 31)*. Springer, November 1995. p. 83
- [88] Marina K. Kuimova, Gokhan Yahioğlu, James A. Levitt, and Klaus Suhling. Molecular Rotor Measures Viscosity of Live Cells via Fluorescence Lifetime Imaging. *Journal of American Chemical Society Communications*, 116:6672–6673, 2008. p. 100, 101, 102, 105
- [89] C.-L. Kuo and C. Paulette. Meam molecular dynamics study of a gold thin film on a silicon substrate. *Surface Science*, 551:39–58, 2004. p. 22
- [90] K Kuo, R L Thomas, and R W Pryor. Thermal diffusivity of isotopically enriched ^{12}C diamond. *Physical Review B*, 42(2):1104 – 1111, 1990. p. 147
- [91] M. Kupiainen, E. Falck, S. Ollila, P. Niemelä, and A. Gurtovenko. Free volume properties of sphingomyelin, dmpe, dppc, and plpc bilayers. *Journal of Computational and theoretical nanoscience*, 2:401–413, 2005. p. 90
- [92] J.R. Lakowicz. *Principles of Fluorescence Spectroscopy*. Springer, third edition: 2006. p. 123

- [93] Chelsea D. Landon, Ji-Young Park, David Needham, and Mark W. DeWhirst. Nanoscale drug delivery and hyperthermia: The materials design and preclinical and clinical testing of low temperature-sensitive liposomes used in combination with mild hyperthermia in the treatment of local cancer. *The Open Nanomedicine Journal*, 3:38–64, 2011. p. 82
- [94] E. S. Landry and A. J. H. McGaughey. Thermal boundary resistance predictions from molecular dynamics simulations and theoretical calculations. *Physical Review B*, 80(16):165304, OCT 2009. p. 57
- [95] D. Lapotko. Optical excitation and detection of vapor bubbles around plasmonic nanoparticles. *Optics Express*, 17(4):2538–2556, 2009. p. 50
- [96] Scott P. Leary, Charles Y. Liu, and Michael L. J. Apuzzo. Toward the emergence of nanoneurosurgery: Part iii - nanomedicine: Targeted nanotherapy, nanosurgery, and progress toward the realization of nanoneurosurgery. *Neurosurgery*, 58(6):1009–1025, JUN 2006. p. 50
- [97] B.-J. Lee, J.-H. Shim, and M. Baskes. Semiempirical atomic potentials for the fcc metals cu, ag, au, ni, pd, pt, al, and pb based on first and second nearest-neighbor modified embedded atom method. *Physical Review B*, 68:1–11, 2003. p. 22
- [98] Chongsoo Lee and Colin D. Chang, Bain. Raman spectra of planar supported lipid bilayers. *Biochimica et Biophysica Acta*, 1711:59–71, 2005. p. 82, 87, 89
- [99] J. Lee, A. O. Govorov, and N. A. Kotov. Nanoparticle assemblies with molecular springs: A nanoscale thermometer. *Angewandte Chemie-International Edition*, 44(45):7439–7442, 2005. p. 50
- [100] J. B. Lee, K. Kang, and S. H. Lee. Comparison of Theoretical Models of Electron-Phonon Coupling in Thin Gold Films Irradiated by Femtosecond Pulse Lasers. *Materials Transactions*, 52(3):547 – 553, 2011. p. 61
- [101] Michael Levy, Florence Gazeau, Jean-Claude Bacri, Claire Wilhelm, and Martin Devaud. Modeling magnetic nanoparticle dipole-dipole interactions inside living cells. *PHYSICAL REVIEW B*, 84(7), AUG 16 2011. p. 2
- [102] XW Li, LX Sun, XH Lin, and LQ Zheng. Solid lipid nanoparticles as drug delivery system. *Prog Chem*, 19, 2007. p. 2
- [103] E. H. Lieb and J. Yngvason. A fresh look at entropy and the Second Law of Thermodynamics. *Physics Today*, 53:32–37, 2000. p. 10
- [104] M.D. Losego, M.E. Grady, N.R. Sottos, D.G. Cahill, and P.V. Braun. Effects of chemical bonding on heat transport across interfaces. *Nature Materials*, 11(6):502–506, JUN 2012. p. 58
- [105] J.W. Lyn, H.G. Smith, and R.M. Nicklow. Lattice dynamics of gold. *Physical Review B*, 8:3493–3499, 1973. p. 22, 23
- [106] D.-G. Margineanu and E. Schoffeniels. Molecular events and energy changes during the action potential. *Pnas*, 74(9):3810–3813, 1977. p. 98, 120
- [107] J.-B. Masson and G. Gallot. A model for thermal exchange in axons

- during action potential propagation. *Eur Biophys J*, 37:1001–1006, 2008. p. 98, 120
- [108] S. Matosevic. Synthesizing artificial cells from giant unilamellar vesicles: State-of-the art in the development of microfluidic technology. *Bioessays*, 34:992–1001, 2012. p. 120
- [109] Chloé MAUROY. *Fusion d'auto-assemblages lipidiques*. PhD thesis, Université de Toulouse, 2010. p. 120, 122, 127, 128
- [110] S. L. Mayo, B. D. Olafson, and W. A. Goddard. Dreiding - a generic force-field for molecular simulations. *Journal of Physical Chemistry*, 94(26):8897–8909, DEC 27 1990. p. 16, 18, 20, 51, 83, 112
- [111] Anca Meffre, Boubker Mehdaoui, Vinciane Kelsen, Pier Francesco Fazzini, Julian Carrey, Sebastien Lachaize, Marc Respaud, and Bruno Chaudret. A simple chemical route toward monodisperse iron carbide nanoparticles displaying tunable magnetic and unprecedented hyperthermia properties. *Nano Letters*, 12(9):4722–4728, SEP 2012. p. 82
- [112] Amihai Meiri, Asaf Shahmoon, Luca Businaro, and Zeev Zalevsky. Optically reconfigurable structures based on surface enhanced raman scattering in nanorods. *Microelectronic Engineering*, 111:251–255, NOV 2013. p. 50
- [113] Samy Merabia, Sergei Shenogin, Laurent Joly, Pawel Koblinski, and Jean-Louis Barrat. Heat transfer from nanoparticles: A corresponding state analysis. *Proceedings of the National Academy of Sciences of the United States of America*, 106(36):15113–15118, SEP 8 2009. p. 50, 51, 56
- [114] Evan W. Miller, John Y. Lin, E. Paxon Frady, Paul A. Steinbach, William B. Jr Kristan, and Roger Y. Tsien. Optically monitoring voltage in neurons by photo-induced electron transfer through molecular wires Evan. *PNAS*, 109(6):2114–2119, 2012. p. 98, 120
- [115] M. Montal and P. Mueller. Formation of biomolecular membranes from lipid monolayers and a study of their electrical properties. *Proc. Nat. Acad. Sci.*, 69:3561–3566, 1972. p. 75, 86
- [116] M Muchow, P Maincent, and RH Muller. Lipid nanoparticles with a solid matrix (SLN, NLC, LDC) for oral drug delivery. *Drug Dev Ind Pharm*, 34, 2008. p. 2
- [117] Paul Mueller, Donald O. Rudin, H. Ti Tien, and William C. Wescott. Reconstitution of cell membrane structure in *vitro*. *Circulation*, 26:1167–1171, 1962. p. 98
- [118] Paul Mueller, Donald O. Rudin, H. Ti Tien, and William C. Wescott. Reconstitution of cell membrane structure in *vitro* and its transformation into an excitable system. *Nature*, 194:979–980, 1962. p. 98
- [119] Takeo Nakano, Gota Kikugawa, and Taku Ohara. A molecular dynamics study on heat conduction characteristics in dppc lipid bilayer. *J.Chem.Phys.*, 133, 2010. p. 75, 83
- [120] E. Neumann, M. Schaefer-Ridder, Y. Wang, and P. H. Hofschneider. Gene transfer into mouse lyoma cells by electroporation in high electric fields.

- The EMBO Journal*, 1:841–845, 1982. p. 75
- [121] Yuxiang Ni, Hung Le Khanh, Yann Chalopin, Jinbo Bai, Pierre Lebarney, Laurent Divay, and Sebastian Volz. Highly efficient thermal glue for carbon nanotubes based on azide polymers. *Journal of Applied Physics*, 100(19):193118, MAY 7 2012. p. 58
- [122] S. Nosé. A unified formulation of the constant temperature molecular dynamics methods. *J. Chem. Phys.*, 81:511–519, 1984. p. 27
- [123] B. Palpant. Photothermal properties of gold nanoparticles. In C. Louis and O. Pluchery, editors, *Gold Nanoparticles for Physics, Chemistry and Biology*, pages 75–102. Imperial College Press, London, 2012. p. 50
- [124] R Pantoja, D Sigg, R Blunck, F Bezanilla, and J R Heath. Bilayer reconstitution of voltage-dependent ion channels using a microfabricated silicon chip. *Biophysical journal*, 81(4):2389–2394, 2001. p. 98
- [125] D. Pissuwan, S. M. Valenzuela, and M. B. Cortie. Therapeutic possibilities of plasmonically heated gold nanoparticles. *Trends in Biotechnology*, 24(2):62–67, FEB 2006. p. 50
- [126] S. Plimpton. Fast parallel algorithms for short-range molecular-dynamics. *Journal of Computational Physics*, 117(1):1–19, MAR 1 1995. p. 13
- [127] Andraz Polak, Mounir Tarek, Matija Tomsic, Valant, Janez, Ulrih, Natasa Poklar, Andrej Jamnik, Peter Kramar, and Damijan Miklavcic. Electroporation of archaeal lipid membranes using md simulations. *Bioelectrochemistry*, 100:18–26, 2014. p. 82, 135
- [128] Gerald L. Pollack. Kaptiza resistance. *REVIEWS OF MODERN PHYSICS*, 41(1), 1969. p. 35
- [129] Liliana Polo-Corrales and Carlos Rinaldi. Monitoring iron oxide nanoparticle surface temperature in an alternating magnetic field using thermoresponsive fluorescent polymers. *Journal of Applied Physics*, 111(7):07B334, APR 1 2012. p. 50
- [130] Noëlle Pottier. *Nonequilibrium Statistical Physics*. Oxford Graduate Texts, 2009. p. 8
- [131] Zhenpeng Qin and John C. Bischof. Thermophysical and biological responses of gold nanoparticle laser heating. *Chem. Soc. Rev.*, 41(3):1191–1217, 2012. p. 2
- [132] S. Raffy and J. Teissie. Electroinsertion of glycophorin a in interdigitation-fusion giant unilamellar lipid vesicles. *The Journal of Biological Chemistry*, 272:25524–25530, 1997. p. 128
- [133] Ali Rajabpour and Sebastian Volz. Thermal boundary resistance from mode energy relaxation times: Case study of argon-like crystals by molecular dynamics. *Journal of Applied Physics*, 108(9):094324, NOV 1 2010. p. 35, 38, 55
- [134] Suneth P. Rajapaksha, Xuefei Wang, and H. Peter Lu. Suspended lipid bilayer for optical and electrical measurements of single ion channel proteins. *Analytical Chemistry*, 85(19):8951–8955, 2013. p. 98
- [135] A.K. Rappi, C.J. Casewit, K.S. Colwell, W.A. Goddard III, and W.M.

- Skid. Uff, a full periodic table force field for molecular mechanics and molecular dynamics simulations. *Journal of American Chemical Society*, 114(25):10024–10035, 1992. p. 52
- [136] W Rawicz, K C Olbrich, T McIntosh, D Needham, and E Evans. Effect of chain length and unsaturation on elasticity of lipid bilayers. *Biophys J.*, 79:328–339, 2000. p. 73
- [137] W. R. Redwood, S. Takashima, H. P. Schwan, and T. E. Thompson. Dielectric studies on homogeneous phosphatidylcholine vesicles. *Biochimica et Biophysica Acta*, 255:557–566, 1972. p. 75, 86
- [138] Ramon Reigada, Aldo H. Romero, Antonio Sarmiento, and Katja Lindenberg. One-dimensional arrays of oscillators: Energy localization in thermal equilibrium. *Journal of Chemical Physics*, 111(4):1373–1384, 1999. p. 140
- [139] H. H. Richardson, Z. N. Hickman, A. O. Govorov, A. C. Thomas, W. Zhang, and M. E. Kordesch. Thermo-optical properties of gold nanoparticles embedded in ice: Characterization of heat generation and melting. *Nano Letters*, 6(4):783–788, APR 2006. p. 50
- [140] Andreas Riedinger, Pablo Guardia, Alberto Curcio, Miguel A. Garcia, Roberto Cingolani, Liberato Manna, and Teresa Pellegrino. Subnanometer local temperature probing and remotely controlled drug release based on azo-functionalized iron oxide nanoparticles. *Nano Letters*, 13(6):2399–2406, JUN 2013. p. 50
- [141] Ryan S. Ries, Hyeon Choi, Rikard Blunck, Francisco Bezanilla, and James R. Heath. Black lipid membranes: Visualizing the structure, dynamics, and substrate dependence of membranes. *Journal of Physical Chemistry B*, 108(41):16040–16049, 2004. p. 98
- [142] JM RITCHIE and RD KEYNES. THE PRODUCTION AND ABSORPTION OF HEAT ASSOCIATED WITH ELECTRICAL-ACTIVITY IN NERVE AND ELECTRIC ORGAN. *QUARTERLY REVIEWS OF BIOPHYSICS*, 18(4):451–476, 1985. p. 76, 78
- [143] J.-P. Ryckaert, G. Ciccotti, and H. J. C. Berendsen. Numerical Integration of the Cartesian Equations of Motion of a System with Constraints: Molecular Dynamics of n-Alkanes. *Journal of Computational Physics*, 23:327–341, March 1977. p. 21
- [144] S. A. Sanchez, M.A. Gunther, G. and Tricerri, and E. Gratton. Methyl- β -cyclodextrins preferentially remove cholesterol from the liquid disordered phase in giant unilamellar vesicles. *J Membrane Biol*, 241:1–10, 2011. p. 120
- [145] B. TIWARI SANDIP, N. UDUPA, B.S.S. RAO, and P.UMA DEVI. Thermosensitive liposomes and localised hyperthermia - an effective bimodality approach for tumour management. *Indian Journal of Pharmacology*, 32:214–220, 2000. p. 82
- [146] Suzanne Scarlata. Membrane protein structure. *Biophysics Textbook Online*, 2004. p. 73, 74, 120

- [147] P. Schravendijk, N. van der Vegt, L. Delle Site, and K. Kremer. Dual-scale modeling of benzene adsorption onto ni(111) and au(111) surfaces in explicit water. *ChemPhysChem*, 6(9):1866–1871, SEP 5 2005. p. 51
- [148] W. Schrof, S. Rozouvan, E. Van Keuren, D. Horn, J. Schmitt, and G. Decher. Nonlinear optical properties of polyelectrolyte thin films containing gold nanoparticles investigated by wavelength dispersive femtosecond degenerate four wave mixing (dfwm). *Advanced Materials*, 10(4):338–341, MAR 4 1998. p. 50
- [149] S. I. Serdyukov. On the definitions of entropy and temperature in the extended thermodynamics of irreversible processes. *C. R. Physique*, 8:93–100, 2007. p. 10
- [150] M. Shen, W.J. Evans, D. Cahill, and P. Keblinski. Bonding and pressure-tunable interfacial thermal conductance. *Physical Review B*, 84(19):195432, NOV 2011. p. 58
- [151] Sun Sheng, Yin Guangyao, Lee Yi-Kuen, T.Y. Wong Joseph, and Zhang Tong-Yi. Effects of deformability and thermal motion of lipid membrane on electroporation: By molecular dynamics simulations. *Biochemical and Biophysical Research Communications*, 404:684–688, 2011. p. 75, 82, 83, 135
- [152] Sun Sheng, T.Y. Wong Joseph, and Zhang Tong-Yi. Atomistic simulations of electroporation in water preembedded membranes. *Journal of Physical Chemistry B*, 115:13355–13359, 2011. p. 75, 82, 83
- [153] A. Siems, S.A.L. Weber, J. Boneberg, and A. Plech. Thermodynamics of nanosecond nanobubble formation at laser-excited metal nanoparticles. *New Journal of Physics*, 13:043018, 2011. p. 50
- [154] Daw S.M. and M.I. Baskes. Embedded-atom method : Derivation and application to impurities, surfaces, and other defects in metals. *Physical Review B*, 29:6443–6453, 1984. p. 21
- [155] Kyle C. Smith, R.S. Son, T.R. Gowrishankar, and James C. Weaver. Emergence of a large pore subpopulation during electroporating pulses. *Bioelectrochemistry*, 100:3–10, 2014. p. 82, 135
- [156] Harry A. Stern and Scott E. Feller. Calculation of the dielectric permittivity profile for a non-uniform system: Application to a lipid bilayer simulation. *Journal of Chemical Physics*, 118(7):3401–3412, 2003. p. 82
- [157] Roland Stone, Stephen Hipp, Joel Barden, Phillip J. Brown, and O. Thompson Mefford. Highly scalable nanoparticle-polymer composite fiber via wet spinning. *Journal of Applied Polymer Science*, 130(3):1975–1980, NOV 5 2013. p. 82
- [158] Yuanyuan Su, Xinpan Wei, Fei Peng, Yiling Zhong, Yimei Lu, Shao Su, Tingting Xu, Shuit-Tong Lee, and Yao He. Gold nanoparticles-decorated silicon nanowires as highly efficient near-infrared hyperthermia agents for cancer cells destruction. *Nano Letters*, 12(4):1845–1850, APR 2012. p. 50, 82
- [159] I. P. Sugár. A theory of the electric field-induced phase transition of

- phospholipid bilayers. *Biochimica et Biophysica Acta*, 556:72–85, 1979. p. 79
- [160] C Sun, JSH Lee, and MQ Zhang. Magnetic nanoparticles in MR imaging and drug delivery. *Adv Drug Deliv Rev*, 60, 2008. p. 2
- [161] Sheng Sun, Joseph T. Y. Wong, and Tong-Yi Zhang. Effects of external electric fields on the self-assembly of phospholipids/water mixtures (coarse-grained molecular dynamics simulations). *Soft Matter*, 7:9307–9310, 2011. p. 75
- [162] Sheng Sun, Joseph T. Y. Wong, and Tong-Yi Zhang. Molecular dynamics simulations of phase transition of lamellar lipid membrane in water under an electric field. *Soft Matter*, 7:147–152, 2011. p. 75
- [163] I Tasaki, K Kusano, and P M Byrne. Rapid mechanical and thermal changes in the garfish olfactory nerve associated with a propagated impulse. *Biophysical journal*, 55(6):1033–1040, 1989. p. 76
- [164] Ichiji Tasaki, Kiyoshi Kusano, and Paul M. Byrne. Rapid mechanical and thermal changes in the garfish olfactory nerve associated with a propagated impulse. *Biophys. J.*, 55:1033–1040, 1989. p. 98, 120
- [165] J. Teissie and T. Y. Tsong. Electric field induced transient pores in phospholipid bilayer vesicles. *Biochemistry*, 20:1548–1554, 1981. p. 128
- [166] Z. Tian, A. Marconnet, and G. Chen. Enhancing solid-liquid interface thermal transport using self-assembled monolayers. *Applied Physics Letters*, 106(211602), 2015. p. 59
- [167] K. Toukan and A. Rahman. Molecular-dynamics study of atomic motions in water. *Physical Review B*, 31:2643–2648, March 1985. p. 21
- [168] S. Toyama, A. Nakamura, and F. Toda. Measurement of voltage dependence of capacitance of planar bilayer lipid membrane with a patch clamp amplifier. *Biophys. J.*, 59:939–944, 1991. p. 75, 86
- [169] Stephanie Tristram-Nagle and John F. Nagle. Lipid bilayers: thermodynamics, structure, fluctuations, and interactions. *Chemistry and physics of lipids*, 127:3–14, 2004. p. 72, 73
- [170] S. Tristram-Nagle, H. I. Petrache, and J. F. Nagle. Structure and interactions of fully hydrated dioleoylphosphatidylcholine bilayers. *Biophys J.*, 75:917–925, 1998. p. 72
- [171] D Van Der Spoel, E Lindahl, B Hess, G Groenhof, AE Mark, and HJ Berendsen. GROMACS: fast, flexible, and free. *J Comput Chem*, 26, 2005. p. 21
- [172] A. Varnier, Kermarrec F., I. Blesneac, Moreau C. and Liguori L., Lenormand J. L., and Picollet-Dahan N. A simple method for the reconstitution of membrane proteins into giant unilamellar vesicles. *J Membrane Biol*, 233:85–92, 2010. p. 120
- [173] Loup Verlet. Computer "experiments" on classical fluids. i. thermodynamical properties of lennard-jones molecules. *Phys. Rev.*, 159:98–103, 1967. p. 13
- [174] S. Louic Vermeer, Bert L. de Groot, Valérie Réat, Alain Milon, and Jerzy

- Czaplicki. Acyl chain order parameter profiles in phospholipid bilayers: computation from molecular dynamics simulations and comparison with ^2h nmr experiments. *Eur. Biophys. J.*, 36:919–931, 2007. p. 90
- [175] A.N. Volkov, C. Sevilla, and L.V. Zhigilei. Numerical modeling of short pulse laser interaction with an nanoparticle surrounded by water. *Applied Surface Science*, 253(15, SI):6394–6399, 2007. p. 50
- [176] Lanhua Wei, P. K. Kuo, R. L. Thomas, T. R. Anthony, and W. F. Banholzer. Thermal conductivity of isotopically modified single crystal diamond. *Physical Review Letters*, 70(24):3764–3767, 1993. p. 147
- [177] Dongsheng Wen. Nanoparticle-related heat transfer phenomenon and its application in biomedical fields. *Heat Transfer Engineering*, 34(14, SI):1171–1179, NOV 14 2013. p. 50, 82
- [178] O. Wesołowska, K. Michalak, J. Maniewska, and A. B. Hendrich. Giant unilamellar vesicles – a perfect tool to visualize phase separation and lipid rafts in model systems. *Acta Biochimica Polonica*, 56:33–39, 2009. p. 120
- [179] S H White. Formation of "solvent-free" black lipid bilayer membranes from glyceryl monooleate dispersed in squalene. *Biophysical journal*, 23(3):337–347, 1978. p. 98
- [180] S. H. White. Formation of "solvent-free" black lipid bilayer membranes from glyceryl monooleate dispersed in squalene. *Biophys J.*, 23:337–347, 1978. p. 109
- [181] M. C. Wiener and S. H. White. Structure of a fluid dioleoylphosphatidylcholine bilayer determined by joint refinement of x-ray and neutron diffraction data. iii. complete structure. *Biophys J.*, 61:434–447, 1992. p. 72
- [182] Y. Wu, K. He, S. J. Ludtke, and Huang H. W. X-ray diffraction study of lipid bilayer membranes interacting with amphiphilic helical peptides: diphytanoyl phosphatidylcholine with alamethicin at low concentrations. *Biophys J.*, 68:2361–2369, 1995. p. 72
- [183] Yilei Wu, Martin Stefl, Agnieszka Olzyńska, Martin Hof, Gokhan Yahioğlu, Philip Yip, Duncan R Casey, Oscar Ces, Jana Humpolíčková, and Marina K Kuimova. Molecular rheometry: direct determination of viscosity in Lo and Ld lipid phases via fluorescence lifetime imaging. *Physical chemistry chemical physics : PCCP*, 15(36):14986–93, 2013. p. 98, 105, 120, 124
- [184] Yilei Wu, Martin Stefl, Agnieszka Olzyńska, Martin Hof, Gokhan Yahioğlu, Philip Yip, Duncan R Casey, Oscar Ces, Jana Humpolíčková, and Marina K Kuimova. Molecular rheometry: direct determination of viscosity in Lo and Ld lipid phases via fluorescence lifetime imaging. *Physical chemistry chemical physics*, 15(36):14986–93, 2013. p. 106, 116

Titre : Contribution à l'étude de la relaxation thermique dans des nanostructures d'intérêt biologique

Mots clés : Nanosciences, Matière Molle, Transition de Phase, Transfert thermique, Microscopie de Fluorescence, Dynamique Moléculaire.

Résumé : En médecine, les nanotechnologies permettent le développement de nouvelles techniques de soin comme l'hyperthermie local ou la délivrance ciblée de médicaments. Ces applications impliquent de nouveaux défis scientifiques concernant la conception de nanosystems et les propriétés de leur environnement biologique. Dans cette thèse, nous avons analysé plusieurs aspects de la relaxation thermique de tels systèmes. Nous avons mise en œuvre la fois des simulations de Dynamique Moléculaire et des mesures expérimentales de microscopie d'imagerie en temps de vie de fluorescence. Nous présentons une étude numérique du transfert thermique de-

puis une nanoparticule en solution aqueuse et montrons qu'attacher un polymère à sa surface permet de réduire la résistance thermique entre la particule et son environnement. Nous avons modélisé des bicouches lipidiques pour calculer leurs propriétés diélectriques et leur viscosité a été étudiée par microscopie de fluorescence. Ces expériences sont réalisées sur des membranes suspendues et des vésicules unilamellaires géantes et démontrent que la viscosité des bicouches lipidiques diminue avec la température et l'application d'une tension transmembranaire induisant un changement de structure.

Title: Contribution to the study of heat relaxation in nanostructures of biological interest

Keywords: Nanosciences, Soft Matter, Phase Transition, Heat Transfer, Fluorescence Microscopy, Molecular Dynamics.

Abstract: In medicine, nanotechnologies give the opportunity to create new care practices such as local hyperthermia and targeted drug delivery. These applications imply new scientific challenges concerning the design of nanodevices and the properties of their biological environment. In this thesis, we have analysed several aspects of heat relaxation of such systems. We have used both Molecular Dynamics numerical simulations and Fluorescence-lifetime imaging microscopy experiments. We present a study of heat transfer from a solvated nanoparticle and show

that attaching a polymer on its surface reduces the thermal resistance between the particle and its aqueous environment. We have modelled lipid bilayers to compute their dielectric properties and their viscosity have been investigated by fluorescence imaging. The experiments conducted on both suspended lipid membrane and giant unilamellar vesicles show that the viscosity decreases when the temperature increases and when a transmembrane voltage is applied to inducing a structural change.

